PCCP

Physical Chemistry Chemical Physics

Accepted Manuscript

Volume 19
Number 1
7 January 2017
Pages 1-896

PCCP

Physical Chemistry Chemical Physics

rsc.li/pccp

ISSN 1463-9076

PAPER
H.-P. Loock et al.
Determination of the thermal, oxidative and photochemical degradation rates of scintillator liquid by fluorescence EEM spectroscopy

This is an Accepted Manuscript, which has been through the Royal Society of Chemistry peer review process and has been accepted for publication.

Accepted Manuscripts are published online shortly after acceptance, before technical editing, formatting and proof reading. Using this free service, authors can make their results available to the community, in citable form, before we publish the edited article. We will replace this Accepted Manuscript with the edited and formatted Advance Article as soon as it is available.

You can find more information about Accepted Manuscripts in the Information for Authors.

ROYAL SOCIETY OF CHEMISTRY

rsc.li/pccp

Physical Chemistry Chemical Physics

PCCP

ARTICLE TYPE

Perspectives on weak interactions in complex materials at different length scales

J. Fiedler,[a] K. Berland,[b] J. W. Borchert,[c] R. W. Corkery,[d] A. Eisfeld,[e] D. Gelbwaser-Klimovsky,[f] M. M. Greve,[a] B. Holst,[a] K. Jacobs,[g,h] M. Krüger,[i] D. F. Parsons,[j] C. Persson,[k,l] M. Presselt,[m] T. Reisinger,[n] S. Scheel,[o] F. Stienkemeier,[p] M. Tømterud,[a] M. Walter,[p] R. T. Weitz,[c] and J. Zalieckas[a]

Nanocomposite materials consist of nanometer-sized quantum objects such as atoms, molecules, voids or nanoparticles, embedded in a host material. These quantum objects can be exploited as a super-structure, which can be designed to create material properties targeted to specific applications. For electromagnetism, such targeted properties include field enhancements around the bandgap of a semiconductor used for solar cells, directional decay in topological insulators, or high kinetic inductance in superconducting circuits and many more. Despite very different application areas all of these properties are united by the common aim of exploiting collective interaction effects between quantum objects. The literature on the topic spreads over very many different disciplines and scientific communities. In this review, we present a cross-disciplinary overview of different approaches for the creation, analysis and theoretical description of nanocomposites with applications related to electromagnetic properties.

1 Introduction

Recent investigations on novel materials such as solar cells,[1] especially on the photoexcitation-driven processes in such systems,[2,3] aim to increase the efficiency of organic solar cells,[4,5] for instance by exploiting concepts such as singlet fission, the decay from a singlet excitation into two triplet excitations of lower energy. Further applications in organic photovoltaics,[6] optoelectronic devices,[7,8] quantum circuits,[9,10] quantum computers,[11] are related to the study of interactions that are weaker than covalent bonding, ranging from non-covalent bonding in supermolecular complexes[12–14] to long-range electrostatic and Casimir forces governing the formation of colloids.[15] While such "weak" interactions (not to be confused with the weak fundamental force governing lepton decay) are often studied in separate fields of science, these investigations often demand an interdisciplinary approach where methods and approaches of different fields must be combined. However, in using a method beyond the domain they were developed for, one needs to be acutely aware of the various often implicit approximations involved. Moreover, bridging methods developed for different length scales without double counting required an understanding of which physical mechanisms are captured at the different length scales. Thus to make progress, a birds-eye view of the different methods employed to describe long-range interactions in the complex matter is acutely needed. The task of these investigations can be summarised by finding relations between the microscopic properties of systems and the resulting macroscopic effect. In other words, the microscopic properties are propagated to larger macroscopic scales. Different theoretical techniques, given in Fig. 1 have been developed to address this issue. While methods that are fully quantum (such as quantum chemistry or density functional theory) are re-

[a] Department of Physics and Technology, University of Bergen, Allégaten 55, 5007 Bergen, Norway.; E-mail: johannes.fiedler@uib.no

[b] Department of Mechanical Engineering and Technology Management, Norwegian University of Life Sciences, Campus Ås Universitetstunet 3, 1430 Ås, Norway.

[c] 1st Institute of Physics, Georg-August-University, Göttingen, Germany.

[d] Surface and Corrosion Science, Department of Chemistry, KTH Royal Institute of Technology, SE 100 44 Stockholm, Sweden.

[e] Max-Planck-Institut für Physik komplexer Systeme, Nöthnitzer Strasse 38, 01187 Dresden, Germany.

[f] Schulich Faculty of Chemistry and Helen Diller Quantum Center, Technion- Israel Institute of Technology, Haifa 3200003, Israel

[g] Experimental Physics, Saarland University, Center for Biophysics, 66123 Saarbrücken, Germany.

[h] Max Planck School Matter to Life, 69120 Heidelberg, Germany.

[i] Institute for Theoretical Physics, Georg-August-Universität Göttingen, 37073 Göttingen, Germany.

[j] Department of Chemical and Geological Sciences, University of Cagliari, Cittadella Universitaria, 09042 Monserrato, CA, Italy.

[k] Centre for Materials Science and Nanotechnology, University of Oslo, P. O. Box 1048 Blindern, 0316 Oslo, Norway.

[l] Department of Materials Science and Engineering, KTH Royal Institute of Technology, 100 44 Stockholm, Sweden.

[m] Institute of Physical Chemistry (IPC), Friedrich Schiller University Jena, Helmholtzweg 4, 07743 Jena, Germany.

[n] Institute for Quantum Materials and Technologies, Karlsruhe Institute of Technology, 76344 Eggenstein-Leopoldshafen, Germany.

[o] Institute of Physics, University of Rostock, Albert-Einstein-Str. 23-24, 18059 Rostock, Germany.

[p] Institute of Physics, University of Freiburg, Hermann-Herder-Str. 3, 79104 Freiburg, Germany.

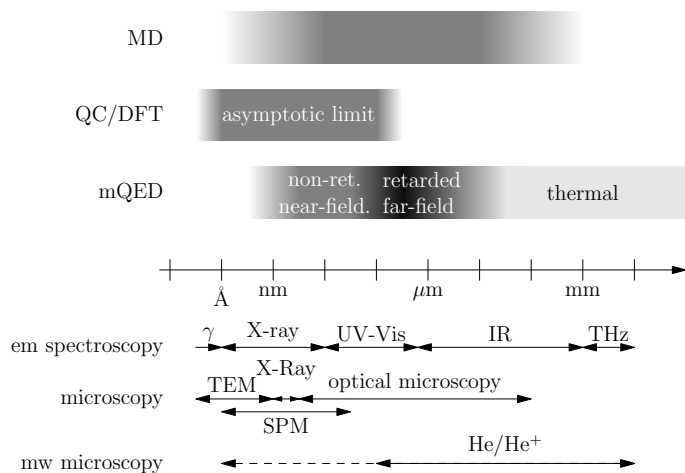Physical Chemistry Chemical Physics Accepted Manuscript

Fig. 1 Length scale overview due to the different theoretical methods (top) (fading out to white indicates the border of the method): classical force field molecular dynamics (MD), quantum chemistry (QC) and density functional theory (DFT), and macroscopic quantum electrodynamics (mQED); and experimental methods (bottom) (bounds are not fixed and overlap): electromagnetic (em) spectroscopy with γ-, X-ray, ultraviolet-visible, infrared, and Terahertz (THz) spectroscopy, microscopy methods: optical and X-ray microscopy, transmission electron microscopy (TEM), and scanning probe microscopy (SPM); matter-wave (mw) spectroscopy beyond electrons: with the helium and helium ion microscopes (the solid line denotes the current resolution limit, the dashed line denotes the theoretical limit).

stricted to small systems with a limited number of electrons, classical force field-based molecular dynamics (MD) simulations can treat systems consisting of a large number of molecules. An alternative to MD simulations is the quantum optical methods, in particular macroscopic Quantum Electrodynamics (mQED). This method considers the coupling of quantised objects via quantised fields. For this reason, it provides a higher accuracy but it does not predict single-particle responses. These properties are input parameters of this theory and it provides their propagation to larger systems. Described as propagating electromagnetic waves, the relevant length scales provide different regimes: the non-retarded regime at small separations, where the finite speed of light does not matter; the retarded regime at larger lengths scales, where retardation effects of the propagating electromagnetic waves play the major role; and the thermal limit, where the interaction is driven by the thermal radiation at the specific system's temperature.

The wide range of applications also reflects the broad range of researchers investigating these systems, from physicists to physicians, chemists to biochemists. This variety causes several issues in the communication between the different researchers due to the differently used nomenclatures and notations. One problematic phrase is "weak interactions", which cannot be defined by giving a particular energy threshold under which the interactions are weak and above they are strong. In Figure 2, a systematic scheme is presented covering the range of weak interactions based on the type of the interacting constituents in line with the traditional chemical view [16] apart from the further distinction of induced forces concerning macroscopic (bulk) responses, such as
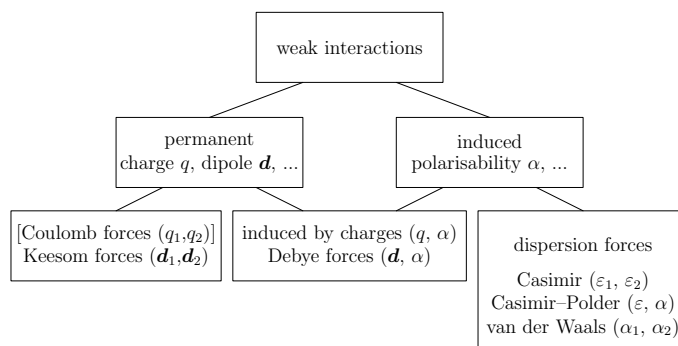

Fig. 2 Systematic overview of weak interactions (restricted to electric interactions) according to the type of interacting objects due to permanent (static) charges q, dipole moments d, and higher-order of static multipoles, and due to induced (dynamical) dipole-polarisabilties α, quadrupole-polarisabilties and higher-orders. Combining two single-particle properties and analysing the resulting interaction, one finds different forces depending on the combination of permanent-permanent, permanent-induced and induced-induced.

the dielectric function ε. Traditionally, one restricts the dispersion forces to be induced by microscopic polarisable objects leading to the van der Waals (vdW) force. For this reason, one often denominates this class by vdW forces and includes the interactions with dielectric bodies. Nowadays, several researchers denote the entire field of weak interactions by vdW interaction, especially in chemistry and colloidal science. From the quantum-optical point of view, this makes sense by applying the electrostatic limit to the dispersive interactions. [17] In contrast in soft-matter physics, one stays strictly in the traditional distinction and neglects the asymptotic transitions from induced to static interactions. An overview of the denominations within the different communities is presented in table 2. In quantum chemistry, the binding between two particles is typically considered, which leads to the phrase "non-covalent" for weak interactions. Concerning non-covalent bonding, ionic and hydrogen bonds belong to the weak interactions, see Fig. 2, as well, but will not be considered explicitly within this review.

Dispersion interaction	origin
Casimir force	$\langle \hat{\rho}\hat{E} + \hat{j} \times \hat{B} \rangle$
Casimir–Polder force	$\langle \hat{d} \cdot \hat{E} \rangle_2$
van der Waals force	$\langle \hat{d}_1 \cdot \hat{E}(r_1) + \hat{d}_2 \cdot \hat{E}(r_2) \rangle_4$

Table 1 Summary of the dispersion interactions applied in the quantum-optics community: The Casimir force as ground-state expectation value of the quantum Lorentz force with the quantised electric and magnetic fields $\hat{E}$ and $\hat{B}$, respectively, and the quantised charge density $\hat{\rho}$ and current $\hat{j}$; the Casimir–Polder interaction as second-order perturbation (index 2 on the expectation value: $\langle \ldots \rangle_2$) of the dipole interaction with the particle's dipole operator $\hat{d}$ and the dressed electromagnetic field $\hat{E}$ at the position of the particle; and the van der Waals interaction as fourth-order perturbation (index 4 on the expectation value: $\langle \ldots \rangle_4$) of the dipole interaction. Details are described in sec. 4.4.1.

The phrase "dispersion forces" traces back to the application of the dispersion relation $k(\omega) = \sqrt{\varepsilon(\omega)}\omega/c$ to take into account the finite speed of light c within a macroscopic medium. In contrast

Table 2 Overview of weak (ground-state) interactions used in different communities.

Particle 1	Particle 2	Quantum Optics	traditional Chemistry	Soft-matter	Statistics	modern Chemistry
charge q_1	charge q_2			Coulomb Interaction		
dipole $\boldsymbol{d}_1$	dipole $\boldsymbol{d}_2$			Keesom Interaction		
dipole $\boldsymbol{d}$	polarisability α			Debye Interaction		
neutral	neutral	Dispersion Int.		van der Waals Interaction		
polarisability α_1 non-retarded retarded	polarisability α_2	van der Waals			van der Waals Casimir–Polder–van-der-Waals	
polarisability α non-retarded retarded	permittivity ε	Casimir–Polder			molecular Lifshitz Casimir–Polder–Lifshitz	
permittivity ε_1 non-retarded retarded perfect conductors	permittivity ε_2	Casimir			Casimir–Lifshitz Casimir–Polder–Lifshitz Casimir	

to the traditionally applied chemical distinction with the restriction to polarisable objects, the consideration of dispersion forces in the quantum-optical framework yields the distinction between the size of the considered objects which can be microscopic polarisable objects or macroscopic dielectric bodies. The resulting distinction between the different interactions is summarised in table 1, which denotes the Casimir force interacting between two dielectric objects; the Casimir–Polder force between a dielectric body and a polarisable object; and the vdW force between two polarisable objects. These three forces built a hierarchical system: by considering two solid objects can obtain the Casimir force between both; by applying the dilute limit to one of them, one reaches the Casimir–Polder force; by applying the dilute limit to both objects, the vdW force will remain. This transition is not reversible, in general. By increasing the density of particles, further interactions will play a role which can not be mapped by a simple up-scaling. For weak responding materials, the Clausius–Mossotti relation

$$\alpha(\omega) = 3V\varepsilon_0 \frac{\varepsilon(\omega)-1}{\varepsilon(\omega)+2}, \qquad (1)$$

with the molecular volume V and the vacuum permittivity ε_0, provides an approximation. However, even the water molecule, it fails in the low energy spectrum due to the missing many-particle effects caused by the hydrogen bond network.[18] A further distinction of the induced interactions is rooted in statistical physics and is restricted to the interactions between two dielectric objects and is in line with the historical development of the description of the Casimir effect. Here, one restricts the Casimir force, according to the original publication,[19] to the force between two perfect conducting plates, the Casimir–Polder force to retardation effects,[20] and the general case for dielectric bodies to the Lifshitz force.[21] Further details on the history of the Casimir theory can be found in Ref. [22]. Another consequence of the dipole approximation is that vdW forces are restricted to point-like particles, which means either atoms or molecules and clusters in the long-range limit such that their separation is much larger than their molecular size. Finite-sized objects experience forces scaling differently than with the inverse sixth power law, see secs. 3.1, 4.2.2, and 4.4.1.

As seen in the beginning, weak interactions are covered by a wide range of research and give rise to several devices and func-tional materials. In the following, we want to introduce recent investigations related to weak interaction studies, covering the application side with the topics of materials and devices; an introduction to relevant characterisation techniques; and an introduction to the most-important theoretical methods describing these materials and effects. We concentrate on ground-state interactions and illustrate partly the treatment of excitations. This review does not provide a comprehensive overview which would quickly fill several books. Instead, we concentrate on the most-relevant effects, experiments and current theoretical methods.

2 Devices and Materials

As introduced above, materials and devices in the context of weak interactions can generally be described as a many-particle effect due to weak interactions, such as atomic clouds, an ensemble of molecules or small clusters, either in a vacuum or in the presence of dielectric solid or liquid surfaces, or the presence of external electromagnetic fields. The most-relevant effects in such systems are the self-organisation near surfaces, leading to vdW heterostructures (sec. 2.2), the excitation dynamics, such as superradiance and singlet fission (sec. 2.1) and the Rabi oscillations in the strong coupling regime (sec. 2.6). The latter occurs by confining the optical mode density for the weak interactions leading to substantial field enhancements. Furthermore, several practical devices result from these interactions, namely solar cells (sec. 2.4), especially organic photovoltaics and top and bottom layers, enhancing the efficiency, electrochemical transistors (sec. 2.3), nano- and micro-electro-mechanical systems (sec. 2.5). Further related topics are due to quantum dots, especially in the context of quantum sensing[23] and quantum computing.[24]

2.1 Interactions and organisation on surfaces

In order to isolate weak interactions, ideally one would like to establish experimental conditions without perturbations from a strongly-interacting environment. Furthermore, having weak interactions and corresponding shallow binding potentials, the competition with thermal energies often requires low-temperature conditions in order to reach state specificity and selective probing. Rare-gas clusters, travelling as isolated cluster beams in a vacuum, have been demonstrated to serve as versatile laboratories for the study of weakly-interacting molecular
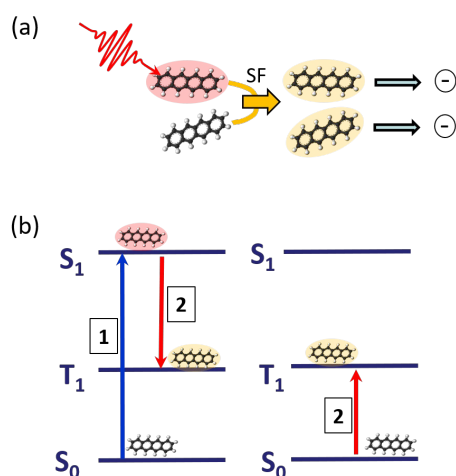
(a)

(b)

Fig. 3 (a) illustration of singlet fission at an example of two pentacene molecules: one molecule is photo-excited into the first electronically excited singlet state. The weak interaction with a second ground-state molecule leads to the population of triplet states on both molecules, which can in a photovoltaic application lead to two separate charge carriers. (b) corresponding level diagram including only the main contributing states.
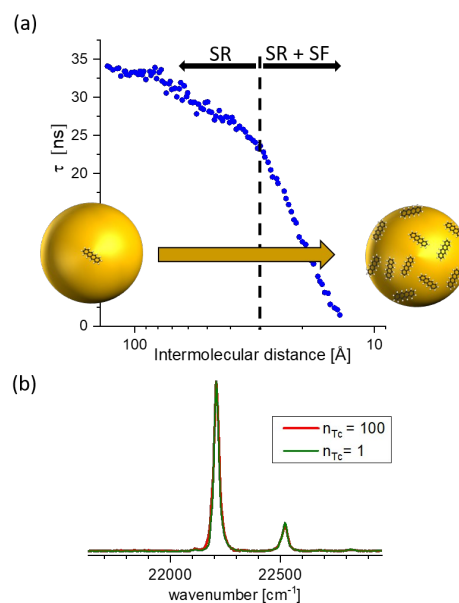

(a)

(b)

Fig. 4 (a) lifetime of excited tetracene molecules attached to the surface of neon clusters as a function of the mean internuclear distance given by the surface coverage. At low coverage, only superradiance leads to a reduction of a lifetime; the prominent reduction at increased coverage is due to singlet fission. (b) Laser-induced fluorescence excitation spectra of the 0_0^0 excitation, and the first prominent vibrational mode at low and high coverage, respectively. n_{Tc} denotes the mean number of tetracene molecules attached to the cluster. Within the cluster-induced broadening, no perturbation from the interaction of the molecules can be identified. Based on data from Ref. [33]

systems.[3,25,26] Technically such clusters having nanometre-sized dimension are condensed in a supersonic expansion from high pressure and mostly cold (down to 3 K) reservoirs. Evaporative cooling of the weakly bound rare gases leads to cluster temperatures ranging from several tens of Kelvin for e.g. argon or neon[27], down to 400 mK/150 mK in case of the isotopes helium-4/helium-3[28,29].

The clusters can be doped with atoms or molecules of interest by the so-called pickup technique, whereupon sticky collisions dopants are attached to the clusters. The number of dopants can be controlled by the pressure in designated vapour cells. Putting such doping units in series along the cluster beam path allows in a well-controlled order an assembly of dopants on the clusters. Whereas helium clusters are liquid, allowing an agglomeration of dopants inside the clusters, all other larger rare-gas clusters are in a solid state. Aromatic molecules, as discussed in the following, are pinned to the surface of these clusters and do even on electronic excitation not migrate to interact with other dopants.[26] By varying the dopant density at statistical low coverage, one can probe weak interactions as a function of the mean intermolecular distance. Here, we want to discuss a prime example of interacting acene molecules. Acenes are of applied interest as absorbers in organic photovoltaics and, in particular, exploiting collective effects by means of singlet fission (SF) has been identified as an alternative route for an increased efficiency converting absorbed photons into separated charges,[30,31] applied in solar cells, see Sec. 2.4.

The process of SF is illustrated in Fig. 3: an absorbed photon leading to an electronically-excited singlet state, which would undergo in an isolated molecule fluorescence emission, can, communicated by the interaction with a neighbouring molecule, transfer the excitation energy into two triplet states, localised on two molecules. Having now two excited molecules can in turn with an appropriate charge separation mechanism lead to the generation of two charges, having only one photon absorbed in the first place. In this way, one is in principle even able to overcome the Shockley–Queisser efficiency limit,[32] acting as the ultimate upper bound for efficient energy conversion.

Tetracene and pentacene molecules are typical examples of having a suitable energy structure of singlet and triplet states enabling SF. Attaching these molecules to the surface of rare-gas clusters, it was demonstrated that SF is even active at dilute conditions with very weak intermolecular interaction.[2,33]

In Figure 4 (a), the measured lifetime of tetracene molecules attached to neon clusters is plotted as a function of the mean intermolecular distance. Whereas at larger distances there is only a slight reduction due to Dicke superradiance, below approximately 30 Å one observes a steep decrease due to SF, reducing the lifetime down to only a few nanoseconds. The assignment to SF and superradiance, respectively, as evidenced by pump-probe schemes and power dependencies and accompanying theoretical simulations.[2] Intriguingly the interaction is so weak that it can not be identified in the spectroscopy of the excited system [perturbation of the spectra, c.f. Fig. 4 (b)].

Furthermore, the interaction with the surface can be studied in these experiments. In comparison with DFT, described in Sec. 4.3, calculations for pentacene molecules attached to neon clusters, vibrationally resolved spectra clearly identify active low-frequency butterfly vibrations from the interactions with the rare-gas sur-
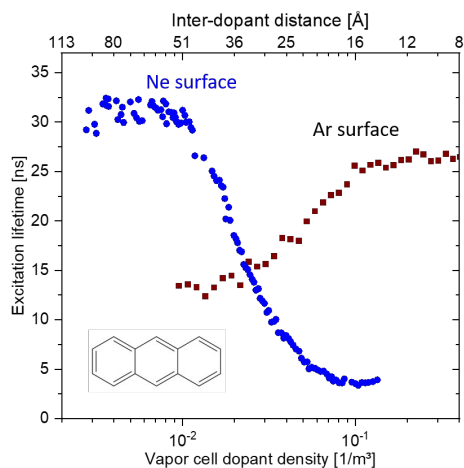
Fig. 5 Comparison of the coverage-dependent lifetime reduction of the first excited singlet state of anthracene molecules attached to Ne and Ar clusters, respectively. The weak perturbation from the interaction with the rare gas leads for Ne to a reduction at high coverage, whereas for Ar the lifetime is increased. Based on data from Ref. [35]

face.[34] Moreover, the weak interaction can even induce perturbations in the organic structure of the molecules leading to suppressed or completely altered decay mechanisms. Such effects are, for instances, capable via mQED (Sec. 4.4) or modelling aggregate structures (Sec. 4.6). As an example in Fig. 5 anthracene molecules are probed as a function of the mean inter-molecular distance on neon and argon clusters, respectively. Since in the case of neon a significantly decreased lifetime at smaller intermolecular distances has been observed, for argon, the lifetime of the excited state is increasing.[35]

Besides rare gas clusters also other dielectric surfaces only weakly perturb the optical properties of molecules deposited on the surface,[36,37] see sec. 4.4.1. Such molecule surface structures can for example be produced by epitaxial growth in ultrahigh vacuum. Typically one can vary the surface density of the molecules over orders of magnitude from very low coverage to full monolayers. It is often possible to use the surface as a template to induce a specific regular arrangement of the molecules ,[36,38,39] which can be probed by atomic force microscopy (AFM) or scanning tunnelling microscopy (STM), see sec. 3.1. Similar to the situation of rage gas clusters one can perform optical far-field spectroscopy. In addition, one can also use various near-field techniques to gain information on these samples.[40–44] It is also possible to change the temperature of the sample from a few Kelvin up to room temperature and above. This allows one, for example, to study the temperature dependence of superradiance.[45]

Another example, where dispersion forces play a major role, is the interaction between nanodiamonds (NDs). Typically, 4-5 nm ND tend to self-assemble into larger aggregations either in the liquid phase or during drying. In the latter case, agglomeration during drying makes ND functionalisation difficult since it often requires dry starting ND material.[46] In the liquid phase, DFT computations in conjunction with Monte Carlo molecular simulations show that assembly interactions between ND particles are domi-

nated by vdW forces rather than electrostatic forces.[47] Therefore, dispersion forces between ND particles or ND and surfaces should be considered carefully in experimental or theoretical investigations. For example, it has been demonstrated that fluorescent ND tethered by double-stranded DNA to a surface can be used as an ultrasensitive label for in vitro diagnostics.[48] Consideration of weak interactions for such systems is expected to improve experiment settings and yield better sensitivities.

2.2 Van der Waals Hetrostructures

It has been long known that the weak short-range vdW interaction holds together layered materials like graphite and MoS_2. The vdW force is weak enough to allow easy sliding of the individual layers against each other such that graphite and MoS_2 have been long established as dry lubricants. The weak interaction between graphene layers has also been the reason that graphite (in the form of highly oriented pyrolytic graphite, HOPG) has been used as a substrate for scanning probe microscopy: simply by mechanical cleavage by scotch tape, a HOPG crystal fresh surface could be prepared.[49] More recently, it has been realised, that this mechanical cleavage can be used to prepare monolayers of such vdW materials, with graphene being the first one subsequently jumpstarting the field of novel 2D materials.[50,51]

While initially mainly monolayers of graphene and other 2D materials had been isolated, it soon was realised that also disjunct materials can be stacked on top of one another. A breakthrough study in this regard had been the work by Dean et al.[52] where for the first time, graphene was placed onto h-BN (which is a large-bandgap insulator synthesised in highest quality e.g. by the group of T. Taniguchi and K. Watanabe[53]) to form a vdW heterostructure. The cleanliness of graphene was significantly improved in this heterostructure (as can be for example quantified by a three-fold increase of the charge carrier mobility) due to the atomic flatness and absence of defects of h-BN (see Fig. 6).[54] Recently, h-BN has been also used as an inert substrate for other materials, e.g. organic semiconductors.[55]

This first h-BN-graphene heterostructure already makes the distinction to multilayers of materials grown by conventional vapour deposition methods (e.g. molecular beam epitaxy, MBE) clear, in which layers of disjunct materials are connected by covalent bonds and where interfacial lattice matching and defects have to be carefully managed. Consequently, the growth of such materials is done in an ultrahigh vacuum.[56] The weak vdW interaction, however, has the consequence that the resulting layer arrangements are not as stable as e.g. MBE grown heterostructures. For example, it was shown that strain can lead to a transformation of the rhombohedral to Bernal stacking in graphene multilayers.[57,58] Nevertheless, the assembly of the wide range of 2D materials (more than 1000 unique 2D materials have been predicted to exist[59]) can be in principle performed in ambient conditions using stamping methods, by which the to-be-assembled materials are picked up sequentially using piezo-controlled stamps and placed on top of one another.[60] Like these heterostructures of arbitrary (that is independent of lattice matching conditions required e.g required for epitaxy), vdW materials can be realised.
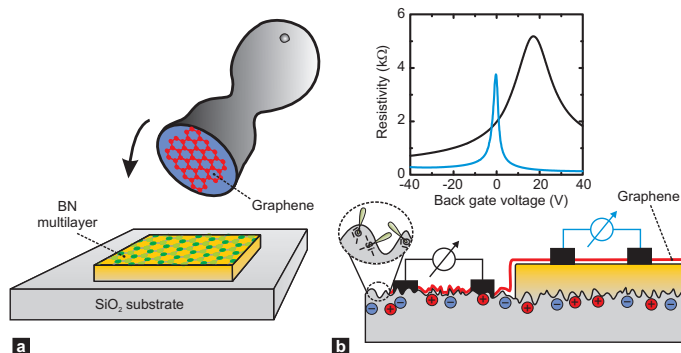
Fig. 6 Supporting graphene on hexagonal boron nitride (BN) substrates. a, Schematic showing how the graphene is transferred onto multilayer BN, which is supported on a SiO$_2$ substrate, with a stamping technique. b, A single piece of graphene (red) is supported by a SiO$_2$ substrate (left) and a flat BN multilayer (right). The corrugations, dangling bonds (inside a dashed circle) and charge inhomogeneities that are inherent to SiO$_2$ surfaces shift and broaden the resistivity peak of the graphene (black line in plot) relative to that of graphene on BN (blue line). Figure taken from Ref. [54].

The resulting interfaces turn out to be very clean due to the so-called "self-cleaning" properties of the materials since often the vdW forces between the to-be-assembled materials turns out to be larger than between that of individual vdW materials and contaminants (typically hydrocarbons).[60,61] This cleaning process can also artificially be initiated with an AFM tip and the self-cleaning imaged in real-time (termed hydrophobic collapse here).[62]

The vdW assembly method offers the exciting possibility to design complex materials on demand by coupling disjunct materials that interact via a Moiré potential creating a superlattice,[63] tunnelling,[64] spin-orbit interaction[65] just to name a few. The coupling can have an impact on the spin degree of freedom, resulting in bandstructure, weakened exchange[66,67] and magnetic properties. One exciting advancement recently has been that if materials of the same type (e.g. two layers of graphene) are twisted by an angle of 1.1° with respect to one another, due to interlayer coupling the bandstructure of the individual graphene layers is modified due to the Moirè potential formed. This leads to a flattening of the band structure and the formation of minibands at the Dirac point with the subsequent observation of correlated phases and unconventional superconductivity.[68,69]

When assembling individual quantum objects into monolayers or their stacks, the material properties are determined by the interactions of the quantum objects with each other[70] (see section 4.6 for predicting such interactions) within the individual layers as well as with the surface, possibly the matrix,[71,72] and possibly the cavity[73,74] surrounding the quantum objects. In order to tailor the material properties, various experimental techniques have been developed that allow the arrangement of quantum objects, for example, DNA origami[75–77] or the Langmuir–Blodgett (LB) and related techniques.[78–81]

Using DNA origami, quantum objects can be arranged with sub-nanometre precision, for which they are covalently bonded to the DNA scaffold.[75–77] Since the resulting arrangements do not interact via vdW forces alone, but initial work has been initiated to de-

velop the current small arrangements towards (vdW) heterostructure materials, they are briefly mentioned in this chapter.[82] Both DNA origami objects, but especially quantum dots and dyes, have been processed by Langmuir–Blodgett and related techniques into thin films or layered structures that interact within and between layers via vdW forces. To do this, for example, typically water-insoluble dyes in solution are applied in small concentrations to a water surface, and the surface concentration is increased by decreasing the available water surface area until a close-packed monolayer is formed, which is tracked via interfacial pressure. Recently, it was demonstrated how the LB technique can also be used to process water-soluble dyes.

In the case of dyes, their arrangement in the monolayer determines the interactions between the transition dipole moments (TDMs, see sec. 3.4) of the dyes and thus the optical and electronic properties of the resulting films.[70] The arrangement is determined by the position of the dyes at the water-air interface and the intermolecular interactions, which are studied by molecular dynamics, force-field-based, and density functional theory methods (see sec. 4.3). In addition, the intermolecular interactions can be affected by embedding the dyes in Langmuir matrices.[71,72] Variation in optical properties with differences in supramolecular structure range from spectral shifts due to interactions between TDMs,[83–91] to optical anisotropy,[92] variation in oscillator strengths due to symmetry breaking,[71,93–96] and the expression of vibronic fine structures[84,88,97–99] in the optical spectra. At intermediate distances 2D materials also offer interesting phenomena related to Casimir interactions[100], as discussed in Sec. 4.1.

2.3 Electrochemical transistors

While the role of the Casimir–Polder force in the interaction between ions has been described (see sec. 4.2.2), a field in which weak interactions have not been considered widely in the field of electrolyte gating in (organic) field-effect transistors. While focusing here on organic polymer semiconductors, the difference between electrostatic and electrolyte gating is, that while in electrostatic gating a purely electrostatic field leads to the accumulation of charges in the semiconductor, in the case of electrolyte gating a liquid electrolyte is placed on the semiconductor and upon application of a voltage difference between the electrolyte and the semiconductor, ions move toward the semiconductor.[101] Then, depending on the materials used the ions can either form a double layer at the liquid/semiconductor interface (called electrostatic gating then as well), or penetrate into the semiconductor (called electrochemical doping).[102] With this method, thin organic semiconducting films but also semiconducting polymers between contacts separated only a few nm can be gated and thus operated as transistors with ultrahigh performance ratios[103] or be used as neuromorphic devices.[104,105] The current flow in such organic electrochemical transistors has also been recently modelled by introducing the movement of the ions in the polymer by the steady-state Nernst–Planck equation and solved numerically.[106] However, the role of the Casimir-Polder interaction has not been included and might be an interesting extension of further work.

2.4 Solar cells

An important field for possible applications is photovoltaic energy generation. A multitude of recent solar cell concepts compete with each other: the prevalent crystalline silicon cells, single-junction GaAs or multi-junction cells, thin-film technologies such as CdTe and CIGS, and other emerging photovoltaic concepts such as organic solar cells or ones based on perovskite structured materials.[5] Their common denominator is the use of irradiance from the solar spectrum to generate electric current. To this end, most solar cells rely on an active layer which has the function of photon absorption and subsequent generation of excitons (usually bound electron-hole pairs). The main challenge is to maximise efficiency, utilising the largest possible part of the solar spectrum, while keeping the fabrication costs as low as possible, which remains the ultimate challenge despite significant advances in the last decade. Multi-junction solar cells have the absolute highest efficiencies with the current record of 39.2% under one sun condition.[107] However, to achieve this, a six-junction cell was designed and fabricated – exemplifying the complexity and consequently the cost of such cells. Therefore, there is a prevailing interest in single-junction cells and methods for enhancing their efficiency. Commonly, the maximum efficiency of any single junction cell is estimated using the infamous Schockley–Queisser limit, which as a first approach is an adequate description. For an ideal band-gap (1.3 eV) cell the upper limit efficiency is around 32%.[108] The limit is met by three loss mechanisms: 1) non-absorbed photons (limitation in photon absorption (intrinsic), reflection losses (extrinsic), 2) thermalisation of excited charge carriers (photon/band-gap miss match), 3) electronic losses through recombination and ohmic losses.[109] The main energy losses are found in the first two categories above. For the first point, traditional and effective methods, use randomised texturing of the sample surface and simple single-layer anti-reflective coatings for maximising the light entering the cell. Using a Lambertian scatterer model for light trapping schemes, the upper light absorption enhancement limit is $4n^2$ compared to single pass absorption, where n is the refractive index of the material.[110]

Using an electromagnetic approach, however, which is necessary to describe sub-wavelength, nano-photonic systems, it has been shown by several research groups that it is possible to increase the light trapping significantly beyond the $4n^2$ limit,[111–113] and also demonstrated experimentally.[114]

With the goal of pushing the efficiency further, light trapping using sub-wavelength structures has been pursued by many research groups, and a wide range of promising nano-structured elements have been investigated such as nano-wires, nano-pillars, upright and inverted nano-pyramids, photonic-crystal-based structures,[110,115–117] and organic molecules, as described in Sec. 2.1 Common for all these nano-structure examples is that typically several nano-lithography steps are needed for the fabrication, a process which significantly complicates the fabrication and consequently limits widespread application. Therefore, another promising nano-structure for solar cell applications is metal nanoparticles (MNPs).[118] The main interest for using MNP in solar applications lies in the strong and tunable light scattering and absorption properties through the localised surface plasmon resonance (LSPR), describable for instance via mQED, see Sec. 4.4. However, the fabrication of MNP is also widely established for a large selection of materials including methods for direct deposition without complex lithography steps, which speaks for scalability.[119]

For solar applications MNP's are typically proposed: 1) placed on the front surface for increased light scattering and consequently light in-coupling into the active layer. 2) Embedded in the active layer for increased optical density through light scattering and near-field effects. 3) On the back surface of the active layer for coupling light not absorbed in the single pass of the active layer to surface plasmon polaritons.[120,121]

MNP added to the front of solar cells is perhaps the simplest configuration and has been investigated by several research groups.[122–124] In particular, metals such as Au and Ag have been investigated due to their strong plasmonic activity in the visible spectrum. Larger nanoparticles (> 30 nm) are typically employed as these have a strong light-scattering component. Promising results for improvements in light incoupling and consequently photocurrent have been demonstrated, but improvements have typically been limited to the longer wavelength ranges. At shorter wavelengths, negative contributions have been reported due to parasitic light absorption of the MNP. Parasitic light absorption has been a challenge for obtaining excellent broad-band results. It is caused by MNPs used in general exhibiting an increased light absorption at shorter wavelengths, but also electron inter-band transitions in the metals.[125–127] These parasitic losses can potentially be omitted by exploring other materials, and recently Al nanoparticles have gained attention. With the plasmon resonance in the UV range, the light absorption losses are minimised, and mainly scattering effects are found in the visible range making them a promising candidate for wide range and efficient light incoupling.[128–130]

For MNPs with a diameter below 30 nm, the far-field scattering will be reduced, and the plasmon interaction will be dominated by near-field effects.[130] Small particles embedded in the active layer have been investigated for enhancing light absorption for both organic solar cells and inorganic solar cells (a-Si).[131,132] Increased light absorption can allow for decreased active layer thicknesses, which in turn would raise the theoretical efficiency limit and yield higher solar cell efficiencies as the charge carrier recombination would be lowered.[133] Theoretical predictions have shown that using small Ag nanoparticles, a conversion efficiency of 18% with only a 15 nm active layer (a-Si) is possible.[131]

The final approach is to increase the optical path length of light not absorbed in a single pass of the active layer, reaching the back surface plane of the active layer to surface plasmon polaritons (SPP). SPP are charge density waves propagating parallel to the back metal/semiconductor interface and are strongly confined once excited and can propagate several micrometres with minimal loss.[134] Due to the momentum mismatch between incident light and the in-plane SPP methods for efficient coupling needs to be employed. Using a periodic grating structure allows an efficient way for coupling incident radiation to SPP modes.[135] Theoretical studies have demonstrated significantly enhanced absorp-

tion enhancement by coupling light to SPP.[134] Furthermore, several nanograting structures such as nano-dent, nano-voids, nanowired and nano-cone have been realised experimentally and noticeable improvement has been reported, and the overall trend is that efficiency on average is improved 1-2%.[136–139] The complicated nano-structuring has so far limited these studies to a-Si solar cells.

2.5 MEMS and NEMS

MEMS and NEMS (micro and nano electromechanical systems), sometimes referred to as micromachines or microsystem technology (MST) are defined as devices which include one or more micro/nano scale parts enhancing functionality.

They are often silicon based, but can also be made of other materials such as quartz, silicon carbide, sapphire and aluminium nitride, as well as polymers[140] (particularly relevant for microfluidic-related applications). Recently, there has been a focus on the application of vdW heterostructure materials for NEMS applications,[141,142] see also sec. 2.2. NEMS can also include components such as nanotubes, nanodots and nanowires. MEMS/NEMS are of significant industrial importance, with an annual market of around 100 million dollars for NEMS alone according to various market reports.

MEMS/NEMS devices can be divided into sensors, actuators and what may be termed passive structures. Sensors include gyroscopes, accelerometers and pressure sensors (extensively used in the automotive industry) and various medical and biochemical diagnostics devices. Actuators include data storage, drug-delivery devices, drug synthesis, fluid regulators, ink-jet printing devices, micro fuel cells, micro-mirror devices, microphones, optoelectric devices, radio-frequency devices and surgical devices and finally passive structures such as atomisers, fluid spray systems, fuel injection, and medical inhalers.[143]

As the dimensions of a system reduce so that the surface-to-volume ratio increases, dispersion forces start to play a role and so it is no surprise that they are crucial in determining the behaviour of in particular a range of NEMS devices. In fact around a decade ago, Casimir forces were seen as a potential obstacle to useful NEMS devices. For example, it was pointed out that at a separation of 10 nm the Casimir force can produce the equivalent of one-atmosphere pressure,[144] see also Ref. [145]. It has been shown both experimentally and theoretically that Casimir and vdW forces have a big effect on the instability of nano-cantilevers, leading to the so-called snap-down (pull-in) behaviour initiated by electrostatic actuation or mechanical shock.[146] The pull-in behaviour occurs when the electrostatic force exceeds the elastic resistance of the beam, which "pulls in" and suddenly adheres to the ground.[147] In general, stiction (adhesion) is a big challenge for NEMS devices. The situation is complicated by the fact that for small distances (in the 100 nm range) the surface roughness starts to play a role.[148] Theoretical models via mQED, see Sec. 4.4 quantise the forces and helps improving such systems.[149]

It has been reported on numerous occasions that 2D materials tend to roll up and form stable scrolls. This is an undesired effect in device fabrication, but it can be used also for nanowires
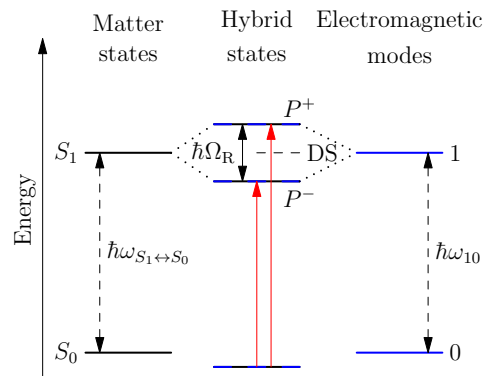

Fig. 7 Schematic energy diagram of strong coupling between an energetic transition, $\hbar\omega_{S_1 \leftrightarrow S_0}$, in a material coupled to a resonant electromagnetic mode, $\hbar\omega_{10}$. Coupling leads to the formation of two-hybrid states, P^+ and P^-, separated by the Rabi-splitting energy, $\hbar\Omega_R$, in addition to uncoupled 'dark' states, DS.

and/or mechanical structures. The roll-up process is governed by a competition between vdW forces and elastic forces.[150]

With the expansion in the technological possibilities for device fabrication, the focus in NEMS development is shifting towards exploiting the dispersion forces actively as an integrated part of the NEMS devices.[151] It should be pointed out though that this is not a completely new idea, for example, the Casimir-induced sensitivity to small changes in distances was exploited in actuators already two decades ago.[152]

2.6 Strong coupling

A striking phenomenon occurs when bringing a material in close proximity to an optical microresonator with electromagnetic modes of similar energies to the material's energetic (e.g. vibrational, electronic) transitions governed by weak (e.g. dipole-dipole) interactions. When the system is properly tuned (depicted schematically in Figure 7), the resulting interaction between weak resonant dipole modeswith the electromagnetic modes can become strong enough to generate a population of pairs of more strongly-interacting hybrid light-matter states within the material, which are then occupied with quasiparticles called 'polaritons.' This relatively simple concept forms the basis of the rapidly-growing body of experimental work in the field of polaritonics encompassing both fundamental and practical studies in chemistry, physics, and materials science.[153–155]

A detailed theoretical treatment of the quantum electrodynamics of strongly coupled systems is discussed in more detail in sec. 4.5. In brief, to facilitate discussions of the experimental work within this section, the polaritonic-state formation can be described as a first approximation by a coupled oscillator model, wherein the strength of the light-matter interaction is indicated by the energy separating the upper and lower hybrid states (P^+ and P^-, respectively) with a characteristic Rabi-splitting frequency

$$\Omega_R = \sqrt{4g^2 - (\kappa - \gamma)^2},\qquad(2)$$

where g is the coupling strength, κ is the photon decay rate, and γ is the non-radiative loss rate for the confined material. When the

losses are sufficiently suppressed (e.g. by using highly reflective mirrors and ideal thicknesses of the interlayers in a Fabry–Pérot cavity) then the system can enter the 'strong coupling regime', where $2g < \kappa, \gamma$. The Rabi-splitting energy proportional to the coupling strength is simply determined by the tuning properties of the coupled material and microresonator

$$\hbar\Omega_{\mathrm{R}} = 2d\sqrt{\frac{\hbar\omega}{2\varepsilon_0 \nu}} \times \sqrt{n_{\mathrm{ph}}+1}, \tag{3}$$

where d is the dipole moment of the material transition, $\hbar\omega$ is the resonant energy of the optical structure, ε_0 is the vacuum permittivity, ν is the electromagnetic mode volume, and n_{ph} is the number of confined photons. Perhaps, the most striking feature arising in (3) and a primary motivator for much of the experimental work in this field is that even if there are no photons contained within the system ($n_{ph} = 0$), there will still be splitting due to the 'vacuum' modes of the resonator (see secs. 4.4.1 and 4.5, thus allowing for coupling to appear without the need for additional photoexcitation. In addition to the 'bright' polariton states, a larger population of delocalised 'dark' states (DS) that have no photonic character are also present.

What has started out as a model quantum optics system where intraatomic transitions have been coupled to cavities[156] has been expanded to the diverse fields of solid-state physics, chemistry and materials science.[155] A multitude of various device physics and potential applications have now been investigated (Fig. 8a-c), including organic polariton transistors,[157] enhanced light-emitting transistors using exciton-polaritons in carbon nanotubes[158] and semiconducting polymers,[159] inversion of singlet and triplet excited states in organic chromophores to enhance quantum efficiency in organic light-emitting diodes,[160] enhancement of ferromagnetism in high-temperature superconductors,[161] modifications of the integer quantum Hall effect,[162] graphene polaritonics,[163,164] and increased charge-carrier transport in e.g. organic semiconductors[165,166] and transition metal dichalchogenides.[167] This latter effect, in particular, introduces both an interesting platform for fundamental studies in charge transport and potentially opens a route towards transistors based on diverse materials that are more efficient. Transport enhancement has been attributed so far to the promotion of greater delocalisation of charge carriers by virtue of the opening of additional bands in a coupled two-level system.[168] However, development of a comprehensive understanding of the parameters that determine whether or not enhanced transport is realised in a given system is ongoing and will need to account for e.g. the role of disorder on carrier and polariton delocalisation under strong coupling conditions[169,170] and dark states.[171] Another promising approach may be to bestow charge on the highly delocalised polaritons by coupling not to charge-neutral excitons, but rather to polarons[172] or trions.[173] In general, the realisation of strongly-coupled systems relies on the availability of sufficient knowledge of the optical and electrical properties of the materials used in the system. Thus characterisation methods to determine e.g. the transition dipole moment of the encapsulated material (see Sec. 3.4) are especially useful.
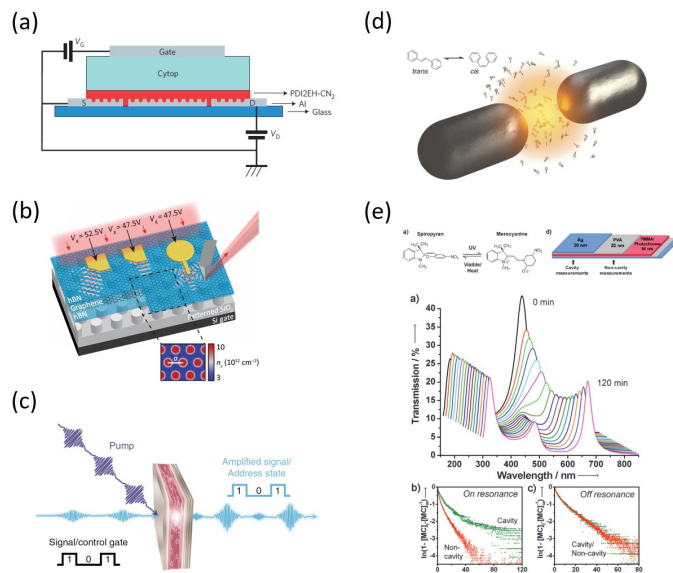

Fig. 8 Examples of recent experiments involving strong coupling. (a) An organic field-effect transistor coupled to the plasmon resonance from a periodic array in an aluminium layer. Taken from Ref. [174] (b) A gated device for manipulating Bloch polaritons generated in graphene encapsulated in hexagonal boron nitride using a plasmonic array in SiO$_2$. Taken from Ref. [164] according to the Creative Commons license[175] (c) An organic polariton transistor. Taken from Ref. [157] (d) Suppression of photoisomerization by coupling to plasmonic modes between metallic nanoparticles. Taken from Ref. [176] according to the Creative Commons license[175] (e) Modification of photoisomerization rate of spiropyran-myocyanine by encapsulation in a Fabry–Pérot cavity. Taken from Ref. [177].

The interest in strongly-coupled systems also stems from the potentially powerful capability of polaritonic states to influence chemical reactions by enhancing the normally weak interactions between the reactants (Fig. 8d, e).[178] It has been reported that the strong coupling to light in a cavity may influence chemical reaction dynamics, which led to the development of the field of polaritonic chemistry or quantum electrodynamics (QED) chemistry.[177,179–181] The strong coupling to the cavity field is envisioned as a control for chemical reaction rates[177] or energy-transfer rates between molecules,[182] and a method for the engineering of novel quantum materials.[183] Some recent studies in practical implementations include the promotion of site selectivity in chemical reactions,[184] enhancement of intermolecular vibrational energy transfer in liquid phase donor-acceptor solutions,[185] and suppression of unwanted photoisomerisation in light-sensitive organic molecules.[176] While the volume of experimental evidence in support of strong-coupling effects on photochemistry continues to grow, the precise mechanisms and limitations with respect to vacuum vibrational strong coupling (i.e. without pumping in additional photons) is the subject of active debate in the theoretical community, especially in regards to the role of dark states in ground state reactions.[186]

Looking ahead, while the above experimental works all involve the use of an optical resonator to achieve strong coupling, such as a plasmonic array or Fabry–Pérot cavity, recent studies have shown that the use of a resonator may not strictly be necessary

to achieve and take advantage of strong coupling effects in some cases. Polaritonic states can, in fact, be realised by tuning the intrinsic properties and nanostructures of the materials of interest and their dielectric environment in order to promote 'self' or 'cavity-less' coupling. [187,188] Indeed, it has been suggested that exciton-polaritons can be the primary source of photoexcitation in a variety of organic molecular nanostructures. [189] Harnessing this aspect may be a key route to the development of simpler implementations of polaritonic devices.

3 Characterisation techniques

Beyond the applications of weak interactions in devices and materials, there are several experimental characterisation techniques analysing nano-structured materials or explicitly using effects occurring from these interactions. In the following, we introduce a small selection illustrating the broad range starting with the most commonly used technique of surface force apparatus and atomic force microscopes, sec. 3.1 via matter-wave scattering experiments probing surface plasmons, sec. 3.2, and dispersion forces, sec. 3.3, and finalising this section with the characterisation of spatially orientated aggregates in thin films and on surfaces, sec. 3.4.

3.1 Insights into intermolecular interactions by Surface Forces Apparatus and Atomic Force Microscopy

The surface forces apparatus (SFA) is one of the earliest techniques that allows quantifying the interactions between two surfaces. Introduced in the late 1960s by Tabor and Winterton, [190] it has been used until today to measure forces in the Piconewton range. [191] Prominent results were e.g. gained for ionic liquids, where long-range electrostatic forces were recorded [192] or for bringing evidence of liquid layering due to a balance of van der Waals attraction and steric and osmotic repulsive forces. [193]

Weak vdW forces also play a significant role in nanoscopic imaging of surfaces using the so-called atomic force microscopy (AFM) [194] which was first introduced in 1986 by Binning, Quate and Gerber. [195,196] Here, an (ideally atomically sharp) tip is attached to a mechanical resonator (e.g., a cantilever [195] or one arm of a tuning fork [197]) and is approached to a surface or an object. That way, force-distance curves like an SFA can be recorded. To obtain images, the tip is raster-scanned across the surface or the object using piezo scanners that allow for sub-nm control of tip movement. Thereby, various modes of operation can be chosen, ranging from a mechanical (and tribological) contact between tip and substrate over "intermitted" to "truly non-contact" AFM modes, depending on the chosen feedback parameters. [198] As between all objects, the forces between the tip, medium (e.g. air, vacuum or a liquid) and sample feature long- and short-range contributions. Long-range contributions include van der Waals, electrostatic and magnetic interactions if one uses the "traditional terms" of interactions, see sec. 1 and table 2.

Short-range contributions mostly stem from quantum-mechanical Born repulsion (also steric repulsion) and, in case fluids are involved, hydration forces or hydrophobic interactions can also lead to short-ranged contributions. [16] Typically, AFM is
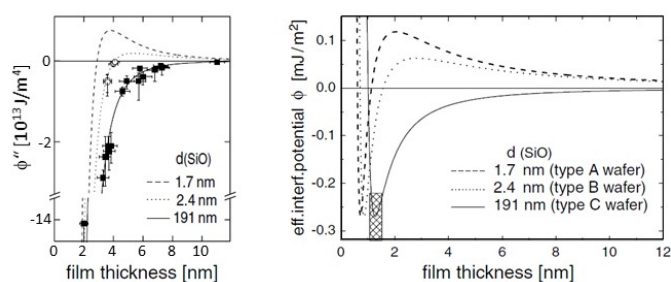

Fig. 9 Example of a reconstruction of the effective interface potential between a thin polystyrene film of the displayed film thickness and a Si wafer with variable SiO$_2$-thickness d. Left: The second derivative of the effective interface potential as a function of film thickness. Data points display the observed spinodal wavelength λ of the dewetting polystyrene film. $\phi''(h)$ and λ are connected via Eq. (4). Taken from Ref. [202].

used to study distances between contact (0 nm) and a few 100 nm, so both short- and long-range forces are important. Since the tip is usually not atomically sharp, a number of atoms interact with another number of the (flat or curved) surface, across a medium, which needs to be taken into account for modelling the interactions. [16] Moreover, even in ultrahigh vacuum, water molecules are present, adsorbing in wedges, especially if the AFM tip contacts the surface. Therefore, capillary forces also contribute to the sum of interactions and many experiments are conducted in water or aqueous solution to avoid uncontrolled capillary forces. Immersing AFM measurements in (slightly) conduction liquid also helps to avoid static charges which can otherwise influence a delicate forces measurement in an uncontrolled manner.

By AFM, it is not possible to record the entire interaction potential between tip and object, since the cantilever imposes an external force that makes the system "jump to contact" at a certain distance above the surface. [199] However, the AFM can nevertheless help to identify the different forces, if individual parameters (e.g., salt concentration or wettability) can be varied separately. [200] Indirectly, by recording the topography of a thin polymer film, AFM helped to reveal the effective interface potential of the system air/thin polymer film/silicon wafer, which can be described by a Lennard–Jones-type potential in the appropriate geometry (two flat semi-infinite interfaces interact) possible: [201,202] at temperatures above the glass transition temperature (here $T > 480$ K), the thin polystyrene film can dewet spinodally under certain conditions off a Si wafer. The spinodal wavelength λ_S is depending on the prepared film thickness h and relates to the second derivative of the effective interface potential $\phi''(h)$ via

$$\lambda_S = \sqrt{-\frac{8\pi^2\sigma}{\phi''(h)}}, \qquad (4)$$

where σ is the known surface tension of the liquid polymer film. [203] By AFM, the spinodal wavelength λ_S can be determined as a function of polymer film thickness, see Fig. 9 left.

Here, the interaction between the film and the surface can be described by

$$\phi(h) = \frac{c}{h^8} + \phi_{vdW}(h), \qquad (5)$$

with the vdW potential

$$\phi_{\text{vdW}}(h) = -\frac{A_{\text{SiO}}}{12\pi h^2} + \frac{A_{\text{SiO}} - A_{\text{Si}}}{12\pi (h+d)^2}. \tag{6}$$

The Hamaker coefficients A_{SiO} and A_{Si} as well as the coefficient c characterising the short-range part were gained by fitting the Lennard–Jones-type potential to the experimental data points, see Fig. 9 (a). The experimental Hamaker coefficients match the ones that can be calculated using the dielectric properties of the materials involved[16] and see sec. 4.4.1. Figure 9 right displays the gained effective interface potentials for different SiO_2 thicknesses on top of the Si wafer.

At very short tip-sample distances, about below 1 nm, the repulsive term that stems from quantum-mechanical Born repulsion dominates. Using careful control of the distance, the force between tip and sample can be measured, and using a feedback mechanism that operates the tip e.g at a constant force high-resolution images can be obtained, even with sub-molecular resolution, see for instance Ref. [204].

The AFM can be operated in various imaging modes (e.g., tapping, contact, etc.) and in various positions of the Lennard–Jones potential (the attractive or the repulsive part, see Fig. 9). Furthermore, the long-range part of the vdW force (along with electrostatic interactions) adds a large background (typically attractive) force between tip and sample that can be with 10 nN larger than the short-range part of the vdW forces (typically < 0.1 nN).[194] This long-range part of the vdW force (also termed Casimir or Casimir–Lifshitz force, see table 2) can be made small by imaging in a liquid medium, as mentioned before[205,206] or even turned into negative.[207,208] Since the initial demonstration of atomic force microscopy imaging in 1986, AFMs have become a standard tool in university and industry laboratories.

3.2 Helium scattering

Helium atom scattering (HAS) is a surface-sensitive characterisation technique; ideal for use when probing fragile and insulating materials, surfaces, and 2D materials. This is due to a combination of low incident energies, usually in the 10 - 100 meV range, with wavelengths comparable to interparticle separation. The helium atoms are electrically neutral, chemically inert, and are scattered by the tail of the electron distribution that seeps out of the probed surface, see sec. 4.3. HAS is therefore a non-penetrating technique that leaves the sample undamaged. An overview of the technique is presented in Fig. 10.

3.2.1 Surface Phonons

Inelastic HAS is, for the reasons described above, ideal for measuring the surface dynamics of materials. The recent rise of 2D materials and vdW heterostructures has proven the need for an experimental technique that can determine their mechanical properties. In particular for applications in flexible electronics, the bending rigidity κ is an important metric. The bending rigidity is a measure of the flexibility of the material. It has been known for several years that the out-of-plane flexural mode, also known as the bending mode or the ZA mode has a dispersion
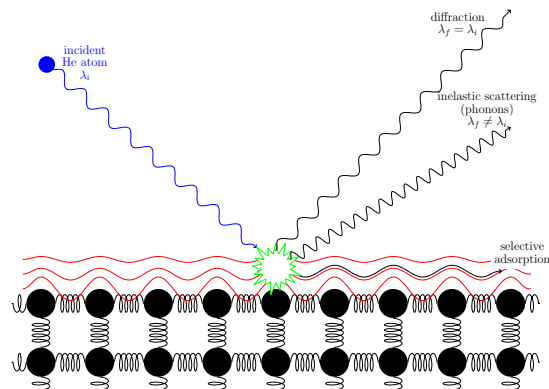

Fig. 10 A helium atom scattering experiment. The helium atom can scatter elastically to give a diffraction pattern, inelastically to provide information about surface dynamics or be adsorbed on the surface.

relation for a free-standing membrane given by[209–211]

$$\omega_{\text{ZA}}^2(\Delta K) = v_{\text{ZA}}^2 \Delta K^2 + \frac{\kappa}{\rho_{\text{2D}}} \Delta K^4, \tag{7}$$

with the parallel wave vector ΔK transferred between the helium atom and the surface, the shear velocity $v_{\text{ZA}} = \sqrt{\frac{c_{44}}{\rho_{\text{2D}}}}$, the shear force constant of the material c_{44}, the 2D mass density ρ_{2D}, and the bending rigidity κ. In an inelastic time-of-flight (TOF) experiment, the ZA-mode will show up as phonon excitation peaks in the recorded spectrum. By varying the incident angle, it is possible to vary the parallel wave vector transfer ΔK. Recording the resulting ZA-excitations allows for mapping out the dispersion relation of the ZA-mode and to extract a value for κ by making a fit of Eq. (7).

It is also worth noting that for substrate-supported membranes, the dispersion relation (7) is modified by the inclusion of the binding energy, ω_0 between the substrate and the membrane.[212] In that case, the dispersion relation reads

$$\omega_{\text{ZA}}^2(\Delta K) = \omega_0^2 + \frac{\kappa}{\rho_{\text{2D}}} \Delta K^4. \tag{8}$$

The quadratic acoustic term in Eq. (7) is in principle present in Eq. (8) as well, but it is at long wavelengths (short ΔK) completely dominated by the constant binding energy, and therefore negligible.

This technique was first applied by Al Taleb *et al.* to measure the bending rigidity of graphene grown on copper foil,[213] more recently to measure the bending rigidity of bilayer silica on ruthenium,[214,215] as well as the temperature dependence of the bending rigidity of *AB*-stacked bilayer graphene.[216]

3.2.2 Electron-Phonon Coupling

Another application of HAS in the context discussed in the present paper is measurements of the electron-phonon coupling (EPC) constant λ. Inelastic HAS' relation to the EPC has been known for some time.[217,218] More recently, it has also been shown that the EPC of metallic surfaces can be related to the Debye–Waller factor.[219–221] The Debye–Waller factor is a measure of the thermal attenuation of the elastic peak in an atom-surface scattering experiment, and has been shown to be proportional to the EPC.[219]

This technique has also been expanded and shown to hold for semiconductors and semimetals. [222,223]

Thermal attenuation of the elastic peak in a (helium) atom surface scattering experiment is given by

$$I(T) = I_0 \exp\left[-2W(\mathbf{k}_i, \mathbf{k}_f, T)\right], \qquad (9)$$

where I is the measured intensity of the elastic peak at temperature T, and I_0 is the hypothetical measured intensity of a frozen surface. The exponential is the Debye–Waller factor and its argument is dependent on temperature, as well as the incident and final momenta of the helium projectile (subscripts i and f, respectively). In general, the argument is given by the thermal average of the product of the scattering momentum vector, $\Delta\mathbf{k} = \mathbf{k}_f - \mathbf{k}_i$, and the effective phonon displacement field, $\mathbf{u}^*$, $2W(\mathbf{k}_f, \mathbf{k}_i, T) = \langle \Delta\mathbf{k} \cdot \mathbf{u}^* \rangle_T$. For HAS from a thin, metallic substrate this argument can be greatly simplified and shown to be [219]

$$2W \approx N(E_F) \frac{m}{m_e^*} \frac{E_{iz}}{\phi} \lambda k_B T, \qquad (10)$$

where $N(E_F)$ is the density of states at Fermi energy E_F, m is the mass of a Helium atom, m_e^* is the effective electron mass, ϕ is the work-function, k_B is the Boltzmann constant and $E_{iz} = \hbar^2 k_{iz}^2 / 2m$ is the normal component of the incident energy. That is to say, from a temperature-resolved measurement of the elastic peak intensity of the surface, the EPC constant can be estimated directly in the low energy regime using HAS. This is advantageous as the experimental technique usually used to measure λ, angle-resolved photoemission spectroscopy (ARPES), is done at much higher incident energies. This makes it difficult for ARPES to determine which phonon bands, and which energy regimes, contribute to the EPC. Using HAS in combination with ARPES is therefore an approach to determine which energy ranges and phonon modes that make significant contributions to the EPC in the investigated materials.

3.3 Matter-wave diffraction and Poisson's spot

The most convenient and direct method for sensing the minute dispersive interaction between a polarisable, but neutral atom or molecule and a surface is matter-wave diffraction. [224–226] There, the usually attractive interaction leads to a phase shift imposed on the de Broglie wavefunction of atoms and molecules that coherently pass by a surface, often in the form of a diffraction grating. The phase shift modifies the observed diffraction pattern, and the strength of the interaction can be extracted by means of careful modelling.

Matter-wave diffraction has been used, among others, to measure C_3 constants for the interaction between silicon nitride gratings and inert gas atoms [227] or sodium atoms. [228] In a more recent example, researchers demonstrated the significantly reduced van der Waals interaction between various ultra-thin carbon-based nanostructured gratings and massive phthalocyanine molecules. [229]

In these experiments, the probed surfaces are restricted to materials that are sufficiently tough so that they can be patterned into freely suspended grating structures on the nanoscale. An al-

ternative near-field diffraction method exists that makes use of the simpler geometry of a sphere as a diffraction obstacle. [230,231] Due to the availability of simple chemical methods to grow spherically shaped sub-micron particles in a bottom-up approach, this has the potential to open matter-wave diffraction to a wide variety of surface materials.

This alternative method is based on the observation of Poisson's spot, which is the bright interference spot in the wave shadow cast by a circular or spherical object. [232–235] Its intensity relative to the undisturbed wavefront, with wavelength λ, for a spatially incoherent source of width w_s, and without any van-der-Waals induced phase shifts is given by the expression [236]

$$I_{\text{rel}} = J_0^2\left(\frac{g\lambda}{w_s R \pi}\right) + J_1^2\left(\frac{g\lambda}{w_s R \pi}\right), \qquad (11)$$

where J_0 and J_1 are zero- and first-order Bessel functions of the first kind, g is the source-to-obstacle distance and R is the radius of the object casting the shadow. The attractive interaction with the surface results in an increase of I_{rel} as the distance between the obstacle and the observation screen is reduced.

Due to the spherical symmetry, the interaction potential can be expressed in a particularly neat expression. [230] Its effect on the Poisson spot can be well described in the Wentzel–Kramers–Brillouin (WKB) approximation by an additional phase shift $\Delta\varphi(a)$ in the Fresnel-Kirchhoff integral [228,234,237] as a function of distance a from the sphere's surface.

In experiments, the assumption of a large sphere and neglecting retardation are applicable. In this case, the shift can be approximated by

$$\Delta\varphi(a) \approx \frac{C_3}{2\hbar v} \frac{3\pi\sqrt{R}}{2\sqrt{2}a^{5/2}} \quad \text{for } a \ll R. \qquad (12)$$

Here, v is the speed of the atom passing by the sphere. In the special case of indium atoms diffracting from spherical silica particles the intensity of Poisson's spot can be well described using a realistic calculation of the interaction potential. [230,231]

We expect that sensing dispersion forces using matter-wave diffraction will contribute to their understanding under realistic conditions such as rough surfaces and finite temperature among others. While results are directly relevant in for example NEMS applications, they may help to advance new concepts for matter-wave interferometry [238] or improve diffractive optics for imaging with neutral atoms. [239,240]

3.4 Determination of transition dipole orientations

Knowledge of, and in many cases a degree of control over, the transition dipole moment (TDM) for a given electronic transition is often of key interest for understanding and utilising complex materials. [92,242] As a prime example, the organometallic molecules implemented in the emissive layers of organic light-emitting diodes (OLEDs) emit light perpendicular to their TDM, thus control over the molecular/TMD orientation has been a critical step for increasing external quantum efficiencies (EQE). [243,244] The TDMs of quantum nanostructures are also an important aspect for the development of quantum photonics ap-
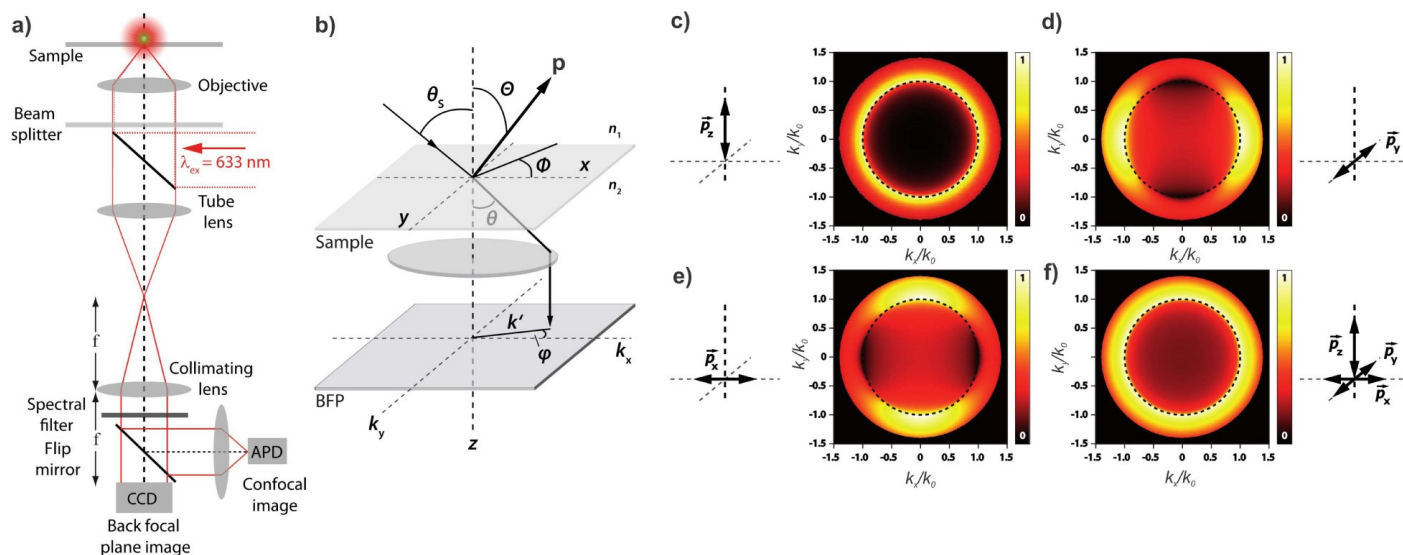
Fig. 11 (a) Example of a setup for back focal plane (BFP) imaging and spectroscopy. (b) Schematic diagram illustrating the mapping of dipoles from a sample onto the BFP. (c)-(f) Numerical calculations of the BFP intensity patterns for differently oriented dipoles. Figure unchanged taken from Ref. [241] according to the Creative Commons license [175]

plications.[241]

Besides classical angle- and polarisation-resolved spectroscopy[92,242,245,246] and sophisticated time-resolved techniques[247], especially back focal plane (BFP) imaging is an elegant and powerful method to determine TMD orientations,[241,248] see Fig. 11. Here, the sample is observed through an oil immersion or high-NA objective to maximise the angular resolution. Emitted light from the photo-excited sample is then collected, and the angular dispersion is resolved via a Bertrand lens focusing onto the BFP of the objective and projected onto a spectrometer CCD. Dipoles p in the sample emit with different angles θ according to the orientation within the sample. This results in an intensity profile for the different k-vectors which are mapped onto the BFP.

4   Theoretical Methods

After introducing various systems where weak interactions play an essential role, we will illustrate the typical theoretical framework describing them. We will focus on the quantum mechanical description of matter's states (sec. 4.3) and demonstrate the statistical (sec. 4.1), electrodynamical (sec. 4.2), and quantum electrodynamical approaches (sec. 4.4) to characterise mesoscopic or macroscopic many-particle systems, such as molecular aggregates (sec. 4.6). Finally, we will continue with systems in extreme conditions leading to strong coupling (sec. 4.5) and Rydberg physics (sec. 4.7).

4.1   Forces on mesoscopic scales

How can Casimir or dispersion forces be treated on mesoscopic scales? We start by treating the involved objects classically, i.e., using their classical scattering operator $\mathbb{T} = T_{ij}(\boldsymbol{r}, \boldsymbol{r}')$, depending on two spacial arguments $\boldsymbol{r}$ and $\boldsymbol{r}'$, and being a 3×3 matrix in the space of electric field vector. It is related to the dielectric and

magnetic properties via ($\mathbb{G}_0$ is the vacuum Green's function)

$$\mathbb{T} = \mathbb{V} \frac{1}{1 - \mathbb{G}_0 \mathbb{V}}.$$

The here introduced potential $\mathbb{V}$ encodes the dielectric (via ε) and magnetic (via μ) responses

$$\mathbb{V} = \frac{\omega^2}{c^2}(\varepsilon - \mathbb{I}) + \boldsymbol{\nabla} \times \left(\mathbb{I} - \frac{1}{\mu} \right) \boldsymbol{\nabla} \times . \tag{13}$$

Note that ε and μ are in general 3×3 matrices, thus potentially encoding anisotropic material properties. They depend on space, thereby characterising the material distributions of the objects, and may also depend on two spacial arguments in case of non-local properties. The Green's function in the presence of an object with operator $\mathbb{T}$ reads

$$\mathbb{G} = \mathbb{G}_0 + \mathbb{G}_0 \mathbb{T} \mathbb{G}_0.$$

The electromagnetic field is then a quantum field, for which the objects play the role of boundary conditions. The Casimir free energy $\mathscr{F}$, i.e., the potential corresponding to the Casimir force for two objects with operators $\mathbb{T}_1$ and $\mathbb{T}_2$ is then found to be[249–251]

$$\mathscr{F} = k_B T \sum_{n=0}^{\infty} \mathrm{Tr} \left\{ \log \left[1 - \mathbb{G}_0 \mathbb{T}_1 \mathbb{G}_0 \mathbb{T}_2 \right] \right\}. \tag{14}$$

Here, the sum runs over Matsubara frequencies, $\xi_n = 2\pi n k_B T / \hbar$, so that $\mathbb{G}_0$ and $\mathbb{T}_2$ are evaluated at imaginary frequencies.[249]

Notably, the forces resulting from Eq. (14) are indeed identical to the average of Lorentz forces acting on the fluctuating charges in the objects as described in Table 1,[252] see sec. 4.4.1.

The form of Eq. (14) allows to provide a number of remarkable general statements for non-magnetic objects ($\mu = 1$). For example, two objects that are each other's mirror images always attract.[253] More general, for any shape of objects, a statement

equivalent to Earshaw's theorem for electrostatics is possible[254]: the Laplacian of the free energy with respect to the positions of the objects is non-positive so that the free energy does not have minima as a function of particle positions; in other words, mechanically stable configurations are ruled out.

The above statements hold true for reciprocal objects, i.e., if $\mathbb{T} = \mathbb{T}^T$ [with transpose $\mathbb{T}^T$, i.e., $[T_{ij}(\boldsymbol{r}, \boldsymbol{r}')]^T = T_{ji}(\boldsymbol{r}', \boldsymbol{r})$], a property following from micro-reversibility.[255] In contrast, recent discoveries have highlighted the relevance of so-called non-reciprocal materials, for which $\mathbb{T} \neq \mathbb{T}^T$. This breakage of micro-reversibility is, for example, possible in the presence of magnetic fields[256], and such non-reciprocal objects find a variety of new phenomena regarding fluctuating electromagnetic fields, including near field energy transfer.[257]

To better understand and prove these properties and to connect to sec. 4.4.1, we expand the log in Eq. (14), keeping only the leading term. This approximation becomes exact when the separation of the objects is much larger than the sizes of the objects, e.g., in the Casimir–Polder or vdW limits. It yields the following simpler expression

$$\mathscr{F} \approx -k_B T \sum_{n=0}^{\infty} \mathrm{Tr}\left\{\mathbb{G}_0 \mathbb{T}_1 \mathbb{G}_0 \mathbb{T}_2\right\}. \tag{15}$$

For reciprocal objects, the scattering operators are symmetric non-negative operators, which lets to determine the sign of the free energy,

$$\mathrm{Tr}\left\{\mathbb{G}_0 \mathbb{T}_1 \mathbb{G}_0 \mathbb{T}_2\right\} \geq 0 \Rightarrow \mathscr{F} < 0. \tag{16}$$

This statement, together with the observation that the free energy typically goes as an inverse power law, d^{-n}, implies that forces between two reciprocal objects are typically attractive.[253,254] Here, d is the objects' separation. Moreover, using the same type of mathematical manipulations, one can determine the sign of the Laplacian and prove Earnshaw's theorem.

As mentioned, these proofs rely on the symmetry of the scattering operator, which thus is not given for non-symmetric operators like those related to non-reciprocal objects.

By splitting the scattering operator into a symmetric and an antisymmetric contribution, it is possible to show that the antisymmetric part gives rise to a *positive* part of the free energy, which typically produces a repulsive force.[258] The latter could dominate for a large antisymmetric part. As an explicit example, we regard two non-reciprocal particles located along the z axis with the following polarisability tensor,

$$\alpha_i = \alpha_0 \begin{pmatrix} 1 & 0 & 0 \\ 0 & 1 & -b_i \\ 0 & b_i & 1 \end{pmatrix}. \tag{17}$$

This tensor breaks reciprocity because it is not symmetric. For simplicity of computation, we assume that Eq. (17) is a frequency-independent response. Evaluating Eq. (15) yields, for $d \ll \hbar c / k_B T$,

$$\mathscr{F} = \frac{\hbar c \alpha_0^2}{64 d^7 \pi^3} \left[-23 - 15 b_1 b_2\right]. \tag{18}$$

This result agrees with the literature for the reciprocal case of $b_i = 0$. For $b_1 b_2 < -\frac{23}{15}$, the free energy is positive, and the resulting force is repulsive.

Figure 12 shows a numerical evaluation of the free energy as a function of the position of the second particle in the xy-plane, with the first particle at the origin. The mentioned properties are seen, i.e., the free energy can be positive or negative, and the force can be attractive or repulsive. Notably, the Laplacian of the free energy (not shown) can be positive or negative, in violation of the corresponding findings for reciprocal cases.[254] This would, in principle, allow for mechanically stable configurations, which are, however, not present for this simple toy model. The free energy in this toy model shows saddle points but not minima.

Despite all these fundamental differences between reciprocal and non-reciprocal objects, in both cases, the Casimir forces are gradients of free energy, and therefore the forces are conservative. This forbids the creation of propulsion forces or cyclic work extraction, which requires the objects to be at different temperatures.[259]

Besides these differences found for equilibrium situations, non-reciprocal objects have other features absent in their reciprocal counterpart such as novel lateral forces,[259–261] nontrivial optical torques,[262,263] recoil forces,[264] lateral thermal-fluctuations-induced forces[265,266] and repulsive forces.[267,268]

Future work can investigate the connection of the presented framework to microscopic approaches as in Sec. 4.4, or including charges as in Sec. 4.2. Also, the connection of these energies to electronic states in Van der Waals Heterostructures, Sec. 2.2, is an exciting topic.
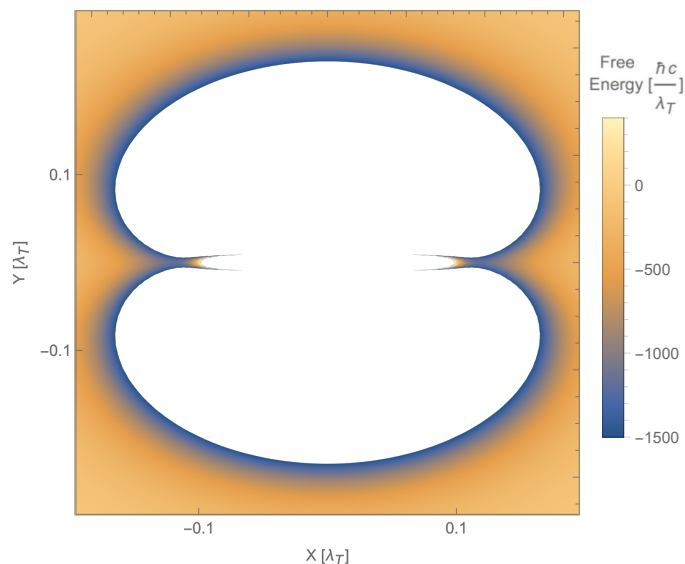

Fig. 12 Free energy of particle 2 as function of its position relative to particle 1, using the polarisability tensor of Eq. (17), $b_1 b_2 = 2$ and $T = 300$ K. The blue areas along the x-axis indicate saddle points (minima along the radial direction but maxima along both angular directions). The white areas represent values of the free energy beyond the ones indicated on the vertical bar.

4.2 Regulation of nanoparticle interactions through a balance of charge and ionic Casimir–Polder interactions

In the study of interactions at surfaces and between microscopic bodies, attention is often drawn first to the charge state of the surface, giving rise to electrostatic forces. The negative surface charge typically arises from the dissociation of acidic oxide sites, hydroxyl groups in the case of mineral oxide materials, and carboxylate groups in the case of protein molecules. The likewise positive charge typically arises through chemisorption of H^+ ions at previously uncharged oxide sites or binding to amine groups. Alternatively, in electrochemical systems, the surface charge can arise due to redox half-reactions or through coupling to an external electrical circuit. An adsorption layer of electrolyte ions can form through physisorption driven by electrostatic interactions with the surface charge.

The conventional theory of surface forces employed to interpret interactions of bodies in electrolyte (salt) solutions is known as DLVO theory, after Derjaguin and Landau,[269] Verwey and Overbeek.[270] The net force in DLVO theory balances electrostatic forces, the entropy of adsorbed ions, and macroscopic dispersion forces. An initial theory of dispersion forces was developed by Hamaker through summation of the individual London dispersion forces between individual molecules comprising the interacting bodies.[271] Dzyaloshinskii later improved the theory of dispersion interaction, Lifshitz and Pitaevskii[21] using macroscopic quantum electrodynamics. This description of dispersion energy is in common use today, often known in short form as Lifshitz theory, see Sec. 4.1 above. The strength, but also the limitation, of Lifshitz theory, is that it presents material properties simply through the permittivity $\varepsilon(i\omega)$ over imaginary frequencies $i\omega$. This makes Lifshitz theory relatively simple to implement, when the dielectric response is known on the imaginary frequency axis $\varepsilon = \varepsilon(i\omega)$, see Secs. 4.1 and 4.4. But by treating the materials, including the medium, with a spatially homogeneous dielectric function $\varepsilon(i\omega)$, spatially resolved effects are neglected. In particular, the standard formulation does not account for the dielectric impact of the ionic adsorption layer itself on macroscopic dispersion interaction.

As for the formation of the ion adsorption layer, it is commonly described using a Boltzmann profile $c_i(x) = c_{i0} \exp(-q_i\psi(x)/k_BT)$ determined by the electrostatic potential $\psi(x)$, c_{i0} being the bulk concentration of the ion. The electrostatic potential, in turn, is determined by the Poisson equation,

$$\nabla[\varepsilon_0\varepsilon(x)\nabla\psi] = -e\sum_i z_i c_i(x) \qquad (19)$$

such that the electrostatic potential ψ is determined by the ion concentration profiles. $\varepsilon(x)$ is the dielectric function of the medium, and ε_0 is the permittivity of the vacuum. e is elementary charge and z_i is the valency of ion i. The two equations together form the Poisson–Boltzmann model.

There are two core deficiencies in the Poisson–Boltzmann model that limit its usefulness in applications, particularly in the development of new applications that aim to achieve a paradigm shift of what is possible beyond the general trends of conventional DLVO theory. Both deficiencies arise from the use of a point-charge model to describe electrolyte ions, which effectively

limits the validity of the model to concentrations below 0.1 mol/L and surface potentials less than 100 mV.

The first deficiency in the point-charge model is that ions are distinguished solely by valency. There is no means of distinguishing Cl^- from ClO_4^-, or Li^+ from K^+. But specific ion effects have been observed experimentally since 1886 when Franz Hofmeister examined the effect of different salts on egg-white protein precipitation.[272] And the differences matter. Na^+ is the dominant cation in normal physiological saline. Li^+ is used as a treatment for bipolar disorder.[273] K^+ is used in lethal injections.[274]

The second deficiency of the point-charge model is that, tautologically, it does not account for the finite size of ions. Its consequence for the Poisson–Boltzmann model is that calculated ion concentrations reach unbounded physically unrealistic levels of 10^6 mol/L or more with consequent unbounded surface forces or electrode capacitances.

Some techniques are already known for dealing with these deficiencies. But the methods currently available leave a set of questions unanswered with respect to the ramifications for dispersion forces used in DLVO analysis. Further development of the underlying Casimir–Lifshitz theory is required to address these questions.

4.2.1 Beyond the Poisson–Boltzmann model

The Poisson–Boltzmann model is a mean-field approximation, the leading term in a more general statistical description of interactions that would include three-body or higher-order many-body effects. The advantage of the Poisson–Boltzmann model, subject to the limitations identified above, is that it enables relatively simple computation of interactions potentially over long length scales (microns). Accounting for correlation effects requires considerably greater computational complexity, solving integral equations[275–277] or molecular dynamics simulations.[278,279]

In general, the Boltzmann component of the Poisson–Boltzmann model can be constructed in terms of an excess chemical potential $\mu_i(x)$ of an ion i describing the ion's interactions at position x relative to its chemical potential in bulk solution. The ion concentration at position x is then $c_i(x) = c_{i0}\exp(-\mu_i(x)/k_BT)$. In the conventional point-charge model, the excess chemical potential is simply the electrostatic energy of the point-like ion with charge q_i in an electrostatic potential $\psi(x)$, $\mu_i(x) = q_i\psi(x)$.

Within the framework of the mean-field Poisson–Boltzmann model, the point-charge deficiencies can be addressed by incorporating various additional interactions $\mu_i^{ex}(x)$ to the chemical potential, resulting in a modified Poisson–Boltzmann model with ion concentrations given by[280]

$$c_i(x) = c_{i0}\, e^{-[q_i\psi(x) + \mu_i^{ex}(x)]/k_BT}. \qquad (20)$$

4.2.2 Specific ion effects and the Casimir–Polder interaction

The specific ion effects reported first by Hofmeister are generally observed in the same order of strength, e.g. $Cl^- < Br^- < I^- < SCN^-$. While the order of ions is not universal—rearrangements of ions may be observed depending on the specific system and concentration—it is common enough to be identified as the conventional "Hofmeister series". The order of the Hofmeister se-

ries roughly correlates with the order of ion polarisabilities. This led Ninham to argue[280] that specific ion effects may be understood by including an ion dispersion interaction, in other words, a Casimir–Polder interaction, into the modified Poisson–Boltzmann model. That is, set

$$\mu_i^{ex}(x) = \mu_i^{disp}(x) \approx -\frac{B_i}{x^3}, \tag{21}$$

to represent the Casimir-Polder interaction of an ion at a distance x from an interface.

The Casimir–Polder interaction enables an interpretation of Hofmeister effects due to the non-electrostatic physisorption of ions at an interface. The expression as written here is problematic for a model of surface adsorption because of the divergence of the interaction at $x = 0$. Mahanty and Ninham provided a methodology[281,282] to address the problem by introducing a finite size to the ion. In their model, the polarisability α_i of the ion is smeared over the volume of the ion, represented as a Gaussian sphere $\exp(-r^2/a_i^2)$ with Gaussian radius a_i, r being the radial distance from the centre of the ion. Conceptually this picture represents the finite volume of the electron cloud of the ion, which is intrinsically ion-specific. However, using a Gaussian sphere is made for mathematical convenience and, strictly speaking, describes a 3D quantum harmonic oscillator. With the Gaussian-sphere representation of the Casimir–Polder interaction, the ion dispersion interaction at an interface becomes

$$\mu_i^{ex}(x) = \mu_i^{disp}(x) \approx -\frac{B_i g_i(x)}{x^3}, \tag{22}$$

where

$$g_i(x) = 1 + \frac{2x}{\sqrt{\pi}a_i}\left[\frac{2x^2}{a_i^2} - 1\right]\exp\left(-\frac{x^2}{a_i^2}\right) - \left[1 + \frac{4x^4}{a_i^4}\right]\mathrm{erfc}\left(\frac{x}{a_i}\right) \tag{23}$$

describes the finite size effect of the ion. In particular as $x \to 0$, $g_i(x)$ approaches the asymptotic form $g_i(x) = (16/3\sqrt{\pi})(x/a_i)^3$ such that the Casimir–Polder interaction energy becomes finite at contact, $\mu_i^{disp}(x=0) = -16B_i/3a_i^3\sqrt{\pi}$.

It should be noted that although the Mahanty–Ninham model incorporates ions of finite size, it embeds the ion in a dielectric medium such that the dielectric response of the medium smears into the volume of the ion. This model neglects additional effects that arise due to the reflection of virtual photons of the interface of an ion cavity cut out of the medium.[283] Nevertheless the model has successfully described the buffer specific effects observed in experimental measurements of protein zeta potentials[284] as well as the surface charge of protein[285] and silica particles[286], and charge reversal effects[284,287]. Once ion cavity effects are included[288], theory of weak interactions is able to reproduce a wide range of bulk experimental properties, including ion solvation energies[288], partial molar volumes and entropies[289], activity coefficients[290], as well as surface tensions[291,292]. Further work is needed to assess the impact of the cavity local field effect on the Casimir-Polder interactions of ions near solid interfaces.

4.3 Non-covalent interactions between molecules and surfaces from electronic structure theory

A microscopic approach to describing non-covalent interactions is to solve the many-electron Schrödinger equation, which accounts for all non-retarded dispersion interactions. Direct diagonalisation is all but impossible for the simplest systems, but perturbation theory approaches have been hugely successful and form the foundations of quantum chemistry. Expressing the wavefunction in antisymmetric Fock-basis in terms of single-particle orbitals between two separate electronic fragments, London-dispersion forces arise naturally to second-order perturbation theory, i.e. in the Møller–Plesset perturbation theory (MP2). While MP2 found some usage in the 2000s for studying bonding between molecules[293] the accuracy is low.[294] Higher-order perturbation theory coupled-cluster (CC) methods especially at the CCSD(T) level is generally too expensive for addressing broad systems of interest,[295,296] but play an invaluable role in providing reference data, for more approximate methods[297,298]. The same role is also played by diffusion Monte-Carlo calculations.[299] A computationally effective method to overcome the computational challenges in particular of CC is symmetry-adapted perturbation theory[300] explicitly defined for accurate exploration of non-covalent interactions. These highly accurate but computationally costly methods might find increased usage in combination with machine-learning approaches[301] as they provide highly accurate training data.

4.3.1 Density functional theory

The workhorse of electronic structure theory is density functional theory (DFT), a versatile and popular method centred around the mean-field electronic density $n(\mathbf{r})$.[302–304] It finds broad usage across every scientific disciple involving properties of molecules or materials, from medicine to geology. Within material science, it is "bread-and-butter" and is used to predict everything from the complex aggregation of atoms and phase boundaries to electronic and vibrational properties and heath transfer and optical properties and other excitation of (nano)materials.[305–307] The topic DFT is covered in many textbooks and reviews; nonetheless, we present it here to emphasise how long-range forces arise in DFT. This is pertinent as there is still a widely held misconception that DFT cannot describe van der Waals forces; however, many standard approximations of DFT lack van der Waals or describe the shorter-ranged part of it.

While the theory of DFT is more general,[308] the acronym DFT refers generally to the Kohn–Sham (KS) realisation,[309] in which the systems are described as consisting of effectively independent electrons $\psi_i(\mathbf{r})$, obeying Pauli repulsion so that $n(\mathbf{r}) = \sum_i^N |\psi_i(\mathbf{r})|^2$. Formally, KS-DFT is an exact theory for the ground state energy of an electronic system, thus the method has the potential to include non-covalent interactions. In practice, its performance and ability to describe such interactions hinge on approximations made. Overall, however, DFT is a highly versatile method from its ability to predict the energy, it can also describe forces acting on atoms of a given atomic configuration and it generally has an excellent trade-off between accuracy and computational cost.

The KS equation has the form of an independent-particle

Schrödinger equation,

$$\left\{ -\frac{\hbar^2}{2m_e}\nabla^2 + V_{\text{eff}}[n](\boldsymbol{r}) \right\} \psi_i(\boldsymbol{r}) = \epsilon_i \psi_i(\boldsymbol{r}), \qquad (24)$$

where the potential $V[n](\boldsymbol{r})$ is a functional of the electronic density, so that the KS equation must be solved consistently and where ϵ_i are the KS energy eigenvalues. The effective potential is given by

$$V_{\text{eff}}[n](\boldsymbol{r}) = V_{\text{ext}}(\boldsymbol{r}) + V_{\text{H}}[n](\boldsymbol{r}) + V_{\text{XC}}[n](\boldsymbol{r}). \qquad (25)$$

Here, $V_{\text{ext}}(\boldsymbol{r})$ is the external potential, typically the electron-nuclei interaction. $V_{\text{H}}[n](\boldsymbol{r})$ is the Hartree potential, the electrostatic repulsion in a mean-field approximation of the electronic density. Finally, the exchange potential $V_{\text{XC}}[n](\boldsymbol{r}) = \delta E_{\text{XC}}[n]/\delta n(\boldsymbol{r})$ accounts for all many-particle effects, where $E_{\text{XC}}[n]$ is the exchange-correlation energy functional. Exchange is the energetic effect of anti-symmetry under the exchange of electron coordinates and correlation, referring to the correlated motion of electrons. Correlation then includes every many-body effect that is not exchanged, including repulsion of an individual electron in the same spatial vicinity, but also the long-range coupling of spontaneously forming electrical dipoles, which give rise to London dispersion forces.

In addition to dispersion forces, longer-ranged electrostatic interactions can also raise the sum of $E_{\text{H}}[n] + \int d\boldsymbol{r} V_{\text{ext}}[n]n(\boldsymbol{r}) + \sum_{i \neq j} V_{\text{ion-ion}}^{ij}$, which includes monopole and static dipole-dipole interactions. Monopole interactions are, of course, the biggest contribution to "strong" ionic bonding, such as halides and oxides. Dipole-dipole interactions are the biggest contribution to hydrogen and halogen bonding. The term also includes Keesom forces, which arise once the KS equation is solved self-consistently, where the existence of dipoles causes a shift in the charge density $n(\boldsymbol{r})$ that sets up permanent dipole-dipole interactions.

In sparse materials,[307] hydrogen bonding is crucial for the structure of materials.[310] However, at longer ranges, dipoles tend to cancel out in complex materials, thus the London dispersion forces tend to be the dominant forces between electrically neutral objects at larger separations. While textbooks often describe "hydrogen bonding" as a purely electrostatic force, the total binding energy also contributes significantly from short-range London dispersion forces[311] and including dispersion forces is important for an accurate description of liquid water.[312]

Proper inclusion of London dispersion forces in DFT, or more broadly Casimir forces, hinges on the approximations used to describe the exchange-correlation functional $E_{\text{XC}}[n]$. Many of the most widely used and successful exchange-correlation functional approximations for describing chemistry and covalent and ionic-bonded materials completely lack long-range dispersion forces. The generalised-gradient approximation (GGA), for instance, is based on information on the local density $n(\boldsymbol{r})$ and the reduced gradient $s(\boldsymbol{r}) \propto |\nabla n(\boldsymbol{r})|/n(\boldsymbol{r})^{4/3}$ to construct $E_{\text{XC}}[n]$. It is a generalisation of the local density approximation (LDA), which is a weighting of the numerically exact exchange and correlation energy density of the homogeneous electron at different densities n, i.e. $E_{\text{XC}}^{\text{LDA}} = \int d^3 \boldsymbol{r}\, n(\boldsymbol{r}) e_{xc}^{\text{hom}}(n(\boldsymbol{r}))$. Integrating only over local

functions of $n(\boldsymbol{r})$ and $s(\boldsymbol{r})$, GGAs lack information on long-range interactions. Thus while GGAs can show good accuracy for covalently bound systems, they are very inaccurate for systems where dispersion forces are important. In the approach developed by Grimme,[313] explicit long-range contribution to the GGA-xc energy are added to the DFT energy, i.e.

$$E_{\text{xc}}[n] = E_{\text{xc}}^{\text{GGA}}[n] - \frac{1}{2}\sum_{A \neq B} f(R_{AB})\frac{C_{6,AB}}{R_{AB}^6}, \qquad (26)$$

where the sum goes over all atoms pairs with their distance R_{AB}. The $C_{6,AB}$ are coefficients that can be tabulated or evaluated self-consistently[314,315] and $f(R)$ is a cut-off function needed to avoid the singularity for $R \to 0$, but in practice also must be tuned to ensure accurate binding energies. Higher order contributions R^{-8} and R^{-10} may be considered as well and non-pairwise terms might be implicitly included in the $C_{6,AB}$, see also Sec. 4.4.1.[316]

Dispersion forces can also be obtained from the many-body theory for electron gases. In particular, the adiabatic-connection fluctuation-dissipation theory (ACFD) provides an exact expression for the exchange-correlation energy,[317,318] as follows

$$E_{\text{xc}} = -\int_0^\infty \frac{du}{2\pi} \int_0^1 d\lambda\, \text{Tr}\left\{ \frac{\tilde{\chi}_\lambda v}{1 - \tilde{\chi}_\lambda v \lambda} \right\} - E_{\text{self}}, \qquad (27)$$

Here $\tilde{\chi}_\lambda v$ is the local field response function for given coupling constant strength, λ. In this expression, the electron self-energy E_{self} must be subtracted. In the coupling-constant integration, the external potential is adjusted to keep density $n_\lambda(\boldsymbol{r}) = n(\boldsymbol{r})$ fixed during the integration. In the so-called ACFD-RPA method, the response function of independent Kohn–Sham orbitals $\chi_\lambda \to \lambda_{\text{KS}}$ is used. The ACDF-RPA method is a rather expensive but quite accurate method for some material classes, including layered materials.[319–321]

The vdW-DF[322–324] framework instead assumes ACDF-mean-value evaluation[325–327] of Eq. (27), which results in[326,328]

$$E_{\text{xc}} = \int_0^\infty \frac{du}{2\pi} \text{Tr}\left[\ln(1 - \tilde{\chi}_{\text{acf}}v)\right] - E_{\text{self}}. \qquad (28)$$

Classical electrodynamics can be used to justify the reformulation,

$$E_{\text{xc}} = \int_0^\infty \frac{du}{2\pi} \text{Tr}\left[\ln(-\nabla \epsilon^{\text{acf}}\nabla v/4\pi)\right] - E_{\text{self}}., \qquad (29)$$

where ϵ^{acf} is analogous to a dielectric function. In the homogenous electron gas limit, this simplifies to

$$E_{\text{xc,hom}} = \int_0^\infty \frac{du}{2\pi} \text{Tr}\left[\ln(\epsilon^{\text{acf}}(iu, |\boldsymbol{r} - \boldsymbol{r}'|))\right] - E_{\text{self}}. \qquad (30)$$

This expression is used to define an effective response function $S = \ln(\epsilon^{\text{acf}})$, which is used an expansion parameter. Next, the key step in vdW-DF is to use a plasmon-pole ansatz for S that captures several exact constraints. The first-order term, however, is parameterised in terms of a semi-local exchange-correlation functional, similar to what is used in standard DFT. Thus, vdW-DF can be viewed as a series expansion in a GGA-type DFT. To second-order, this results in a non-local correlation purely in terms of the

electronic density $n(\boldsymbol{r})$,

$$E_c^{\text{nl}}[n] = \frac{1}{2} \int d^3 r_1 \int d^3 r_2 n(\boldsymbol{r}_1) \phi[n](\boldsymbol{r}_1, \boldsymbol{r}_2) n(\boldsymbol{r}_2). \quad (31)$$

This expression vanishes seamlessly in the homogeneous electron gas limit as the integral of the kernel ϕ integrates to zero for uniform densities. In the long-range limit, however, the $1/r^6$-limit is retained.

The non-locality of the total energy in Eq. 31 still gives a local exchange-potential operator in Eq. 31, and with clever computational approximations, the computational cost of DFT with vdW-DF is comparable to that of GGAs.[329] Hartree-Fock theory uses full Slater determinant to describe the many-particle wavefunction and hybrid DFTs, which can be viewed as a mixture of Hatree-Fock theory and standard KS-DFT; however, results in non-local exchange potentials, which is costly to compute, especially so for plane-wave DFT. However, such non-local exchange does not cross voids and only becomes long-ranged for systems with extended wavefunctions. The use of hybrid functionals; however, provides more accurate electronic densities and exchange energies and, including dispersion interactions with hybrid DFT provides highly accurate (albeit somewhat costly) functionals for chemical interactions and hydrogen bonds[330–332] including proton transfer.[333]

4.4 Divide and Conquer

In the sense of this article, complex materials are many-particle systems composed of (quantum) nano-objects that scale up to micron-sized systems. Their theoretical description is rather complicated due to the many degrees of freedom. Most fundamentally, such systems are described by the many-particle Hamiltonian for a set of charges $\mathscr{A}$[334]

$$\hat{H} = \sum_{\alpha \in \mathscr{A}} \frac{\left[\hat{\boldsymbol{p}}_\alpha - q_\alpha \hat{\boldsymbol{A}}(\hat{\boldsymbol{r}}_\alpha)\right]^2}{2m_\alpha} + \sum_{\alpha \neq \beta} \frac{q_\alpha q_\beta}{8\pi\varepsilon_0 |\hat{\boldsymbol{r}}_\alpha - \hat{\boldsymbol{r}}_\beta|}$$
$$+ \frac{1}{2} \int d^3 r \left[\varepsilon_0 \hat{\boldsymbol{E}}^2 + \frac{1}{\mu_0} \hat{\boldsymbol{B}}^2\right] + \sum_{\alpha \in \mathscr{A}} q_\alpha \hat{\phi}(\hat{\boldsymbol{r}}_\alpha), \quad (32)$$

with the vacuum permittivity ε_0 and permeability μ_0, the charges q_α with position and momentum operators $\hat{\boldsymbol{r}}_\alpha$ and $\hat{\boldsymbol{p}}_\alpha$, the electric and magnetic field operators $\hat{\boldsymbol{E}}$ and $\hat{\boldsymbol{B}}$ and the corresponding scalar and vector potentials $\hat{\phi}$ and $\hat{\boldsymbol{A}}$. The electromagnetic fields in Eq. (32) also describe the quantum vacuum in the absence of absorbing (realistic) materials. For classical electromagnetic fields, the effect of dielectric materials is included via the macroscopic displacement field $\boldsymbol{D} = \varepsilon_0 \boldsymbol{E} + \boldsymbol{P}$, with the polarisation $\boldsymbol{P}$ describing the response of the dielectric object, and the magnetic field strength $\boldsymbol{H} = \frac{1}{\mu_0} \boldsymbol{B} - \boldsymbol{M}$ with the magnetisation $\boldsymbol{M}$ including the magnetic response of the media.[335] This method can be adapted to the quantised fields and yields the diagonalised field Hamiltonian[336]

$$\hat{H}_{\text{F}} = \sum_{\lambda = e,m} \int d^3 r \int_0^\infty d\omega \, \hbar\omega \hat{\boldsymbol{f}}_\lambda^\dagger(\boldsymbol{r}, \omega) \cdot \hat{\boldsymbol{f}}_\lambda(\boldsymbol{r}, \omega), \quad (33)$$

where the field's ladder operators $\hat{\boldsymbol{f}}_\lambda$ are related to the electric and magnetic fields via the dyadic Green function

$$\hat{\boldsymbol{E}}(\boldsymbol{r}) = \int_0^\infty d\omega \sum_{\lambda = e,m} \int d^3 r' \mathbf{G}_\lambda(\boldsymbol{r}, \boldsymbol{r}', \omega) \cdot \hat{\boldsymbol{f}}_\lambda(\boldsymbol{r}', \omega) + \text{H.c.}, \quad (34)$$

$$\hat{\boldsymbol{B}}(\boldsymbol{r}) = \int_0^\infty \frac{d\omega}{i\omega} \sum_{\lambda = e,m} \int d^3 r' \nabla \times \mathbf{G}_\lambda(\boldsymbol{r}, \boldsymbol{r}', \omega) \cdot \hat{\boldsymbol{f}}_\lambda(\boldsymbol{r}', \omega) + \text{H.c.}, \quad (35)$$

that is the fundamental solution of the vector Helmholtz equation

$$\left[\nabla \times \frac{1}{\mu(\boldsymbol{r}, \omega)} \nabla \times - \frac{\omega^2 \varepsilon(\boldsymbol{r}, \omega)}{c^2}\right] \mathbf{G}(\boldsymbol{r}, \boldsymbol{r}', \omega) = \boldsymbol{\delta}(\boldsymbol{r} - \boldsymbol{r}'). \quad (36)$$

One possibility to handle this complexity is the separation of the set of charges $\mathscr{A}$ into disjointed subsets of neutral particles $\mathscr{A}_i$ with "non"-overlapping wavefunctions. For instance, particles with wavefunctions $\psi_{i,j}$ (from subset $\mathscr{A}_{i,j}$ with $i \neq j$) fulfilling

$$\langle \psi_i | \psi_j \rangle \mapsto 0. \quad (37)$$

This separation is formally equivalent to the series expansion of the Coulomb interaction in Eq. (32). According to this separation, the resulting subsets either describe quantum objects, such as atoms, molecules, and small clusters, or macroscopic objects, such as solid surfaces. Concerning the illustrated method, the macroscopic objects will be considered as boundary conditions of the vector Helmholtz equation (36), whereas microscopic objects will be treated as quantised particles in eigenstates[334]

$$\hat{H}_{\text{A}} - \frac{\hat{\boldsymbol{P}}_{\text{A}}^2}{2M_{\text{A}}} = \sum_{\alpha \in \mathscr{A}_{\text{A}}} \frac{\hat{\boldsymbol{p}}_\alpha^2}{2m_\alpha} + \sum_{\alpha \neq \beta} \frac{q_\alpha q_\beta}{8\pi\varepsilon_0 |\hat{\boldsymbol{r}}_\alpha - \hat{\boldsymbol{r}}_\beta|} = \sum_n E_n |n\rangle \langle n|, \quad (38)$$

with the centre-of-mass momentum $\hat{\boldsymbol{P}}_{\text{A}}$ and the total mass of the particle $M_{\text{A}} = \sum_\alpha m_\alpha$. Thus, a particle is completely described by the set of eigen-energies and eigenstates $(E_n, |n\rangle)$. However, typical particles are characterised by by optical data, such as transition energies[337]

$$E_{mn} = \hbar\omega_{mn} = \hbar[E_n - E_m], \quad (39)$$

transition dipole moments[337]

$$\boldsymbol{d}_{nm} = \langle m| \hat{\boldsymbol{d}} |n\rangle = e\langle m| \hat{\boldsymbol{r}} |n\rangle, \quad (40)$$

or transition lifetimes τ_{nm}, which are quantum-mechanically described by the transition rates $\Gamma_{nm} = 1/\tau_{nm}$, that are related to the transition energy and dipole moment via[338]

$$\Gamma_{nm} = \frac{2\mu_0 \omega_{nm}^2}{\hbar} \boldsymbol{d}_{nm} \cdot \text{Im}\mathbf{G}(\boldsymbol{r}, \boldsymbol{r}, \omega_{nm}) \cdot \boldsymbol{d}_{mn} = \frac{\omega_{nm}^3 |\boldsymbol{d}_{nm}|^2}{3\hbar\pi\varepsilon_0 c^3}, \quad (41)$$

where we used the free-space Green function $\text{Im}\mathbf{G}^{(0)}(\boldsymbol{r}, \boldsymbol{r}, \omega) = \omega\mathbb{I}/(6\pi c)$ to obtain Fermi's Golden rule.[339] These quantities are usually combined into the polarisability of the quantised parti-

cle[338]

$$\alpha_n(\omega) = \frac{1}{\hbar} \sum_k \left[\frac{\boldsymbol{d}_{nk}\boldsymbol{d}_{kn}}{\omega_{kn} - \omega - \frac{i}{2}(\Gamma_n + \Gamma_k)} + \frac{\boldsymbol{d}_{kn}\boldsymbol{d}_{nk}}{\omega_{kn} + \omega + \frac{i}{2}(\Gamma_n + \Gamma_k)} \right],$$

(42)

with the total transition rate $\Gamma_k = \sum_{n<k} \Gamma_{kn}$. The advantage of this technique is that it dramatically reduces the number of considered particles. Furthermore, non-relevant quantised objects at the positions $\boldsymbol{r}_i$ can directly be treated via their induced fields

$$\mathbf{G}(\boldsymbol{r}, \boldsymbol{r}', \omega) = \frac{\omega^2}{c^2 \varepsilon_0} \sum_i \mathbf{G}(\boldsymbol{r}, \boldsymbol{r}_i, \omega) \cdot \boldsymbol{\alpha}_i(\omega) \cdot \mathbf{G}(\boldsymbol{r}_i, \boldsymbol{r}', \omega), \quad (43)$$

with typically the free-space Green function $\mathbf{G}(\boldsymbol{r}, \boldsymbol{r}', \omega)$. In the coincidence limit ($\boldsymbol{r}' \to \boldsymbol{r}$), the imaginary part of the Green function is often called local optical mode-density in classical optics.[334] Here, we concentrate on radiative decays. Non-radiative decays would require a quantised environment absorbing the energy in the sense of an open quantum system.[340,341]

Within the macroscopic quantum electrodynamics, the electromagnetic fields are considered as a (macroscopically dressed) response to the vacuum field excitations (33) and the quantised particle in eigenbasis (38). The remaining part of the total Hamiltonian (32) is the interaction between the fields and the particles

$$\hat{H}_{\text{int}} = \sum_{\alpha \in \mathscr{A}} q_\alpha \hat{\phi}(\hat{\boldsymbol{r}}_\alpha) - \sum_{\alpha \in \mathscr{A}} \frac{q_\alpha}{m_\alpha} \hat{\boldsymbol{p}}_\alpha \cdot \hat{\boldsymbol{A}}(\hat{\boldsymbol{r}}_\alpha) + \sum_{\alpha \in \mathscr{A}} \frac{q_\alpha^2}{2m_\alpha} \hat{\boldsymbol{A}}^2(\hat{\boldsymbol{r}}_\alpha). \quad (44)$$

In most cases of interest in practice, one may assume that the quantised particle is small compared to the wavelength of the relevant electromagnetic field. Thus, it is useful to approximate the interaction via the leading-order long-wavelength approximation. This leading-order expansion of the interaction Hamiltonian in terms of the relative particle coordinates leads to the minimal coupling regime which reads for a neutral object[342]

$$\hat{H}_{\text{int}}^{\min} = -\hat{\boldsymbol{d}} \cdot \hat{\boldsymbol{E}}^{\parallel}(\hat{\boldsymbol{r}}_A) - \sum_{\alpha \in \mathscr{A}} \frac{q_\alpha}{m_\alpha} \hat{\bar{\boldsymbol{p}}}_\alpha \cdot \hat{\boldsymbol{A}}(\hat{\boldsymbol{r}}_A) + \sum_{\alpha \in \mathscr{A}} \frac{q_\alpha^2}{2m_\alpha} \hat{\boldsymbol{A}}^2(\hat{\boldsymbol{r}}_A), \quad (45)$$

with the centre-of-mass coordinate $\hat{\boldsymbol{r}}_A$ and the relative momentum $\hat{\bar{\boldsymbol{p}}}_\alpha$. An alternative approach to the minimal coupling regime is the multipolar coupling,[342] that yields a series of interacting multipoles via a Power–Zienau–Woolley transform.[343,344] In the following, we restrict ourselves to consider the dominant dipole interaction $\hat{H}_{\text{int}} = -\hat{\boldsymbol{d}} \cdot \hat{\boldsymbol{E}}^{\parallel}(\hat{\boldsymbol{r}}_A)$.

4.4.1 Dispersion forces

As pointed out in the introduction, the dispersion forces between neutral objects are distinguished by the response of the interacting particles, either dielectric functions for macroscopic objects or dynamics polarisabilities for quantised objects, see tables 2 and 1, and Fig. 13. In the following, we will shortly introduce the origin of the different dispersion forces.

Casimir force: One possibility to introduce the Casimir force is the volume averaged ground-state expectation value of the quantum Lorentz force[342]

$$\boldsymbol{F} = \int_V \mathrm{d}^3 r \langle \hat{\rho}_{\text{in}}(\boldsymbol{r})\hat{\boldsymbol{E}}(\boldsymbol{r}') + \hat{\boldsymbol{j}}_{\text{in}} \times \hat{\boldsymbol{B}}(\boldsymbol{r}') \rangle_{\boldsymbol{r}' \mapsto \boldsymbol{r}}, \quad (46)$$
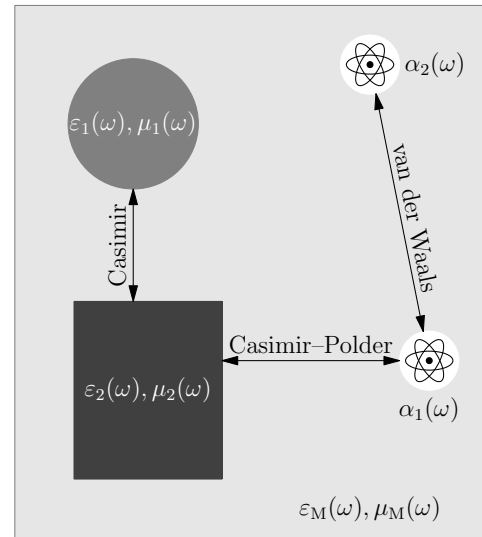

Fig. 13 Schematic illustration of dispersion interactions: Casimir force between two dielectric macroscopic objects with permittivities ε_i and permeabilities μ_i, die Casimir–Polder force acting between a polarisable object α_1 and the dielectric body ε_2, and the van der Waals force interacting between two polarisable objects α_i.

with the internal charge and current densities $\hat{\rho}(\boldsymbol{r})$ and $\hat{\boldsymbol{j}}(\boldsymbol{r})$, respectively. Together with the continuity equation $\dot{\rho}_{\text{in}} + \nabla \cdot \boldsymbol{j}_{\text{in}} = 0$, and the decomposition into noises (index N) and induced charges and currents, $\rho_{\text{in}} = \rho_{\text{N}} - \varepsilon_0 \nabla \cdot [\chi \boldsymbol{E}]$ and $\boldsymbol{j}_{\text{in}} = \boldsymbol{j}_{\text{N}} - i\varepsilon_0 \omega \chi \boldsymbol{E}$, the internal densities in the quantum Lorentz equation (46) can be rewritten in terms of the field operators $\hat{\boldsymbol{f}}$ (quantisation via the noise current density $\boldsymbol{j}_{\text{N}} \to \hat{\boldsymbol{j}}_{\text{N}} \to \hat{\boldsymbol{f}}$) and the ground-state expectation value can be obtained leading the Casimir force[342]

$$\boldsymbol{F} = -\frac{\hbar}{\pi} \int_V \mathrm{d}^3 r \int_0^\infty \mathrm{d}\omega \, \text{Im} \left\{ \frac{\omega^2}{c^2} \nabla \cdot \left[\chi(\boldsymbol{r}, \omega) \mathbf{G}(\boldsymbol{r}, \boldsymbol{r}', \omega) \right] \right.$$

$$\left. - \text{Tr} \left[\mathbb{I} \times \left(\nabla \times \nabla \times + \frac{\omega^2}{c^2} \chi(\boldsymbol{r}, \omega) \right) \mathbf{G}(\boldsymbol{r}, \boldsymbol{r}', \omega) \times \nabla' \right] \right\}_{\boldsymbol{r}' \mapsto \boldsymbol{r}}, \quad (47)$$

with the three-dimensional identity matrix $\mathbf{I}$. By applying contour integration techniques, the integral along the real frequency axis can be turned onto the imaginary axis and yields

$$\boldsymbol{F} = \frac{\hbar}{\pi} \int_V \mathrm{d}^3 r \int_0^\infty \mathrm{d}\xi \left\{ \frac{\xi^2}{c^2} \nabla \cdot \left[\chi(\boldsymbol{r}, i\xi) \mathbf{G}(\boldsymbol{r}, \boldsymbol{r}', i\xi) \right] \right.$$

$$\left. + \text{Tr} \left[\mathbb{I} \times \left(\nabla \times \nabla \times - \frac{\xi^2}{c^2} \chi(\boldsymbol{r}, i\xi) \right) \mathbf{G}(\boldsymbol{r}, \boldsymbol{r}', i\xi) \times \nabla' \right] \right\}_{\boldsymbol{r}' \mapsto \boldsymbol{r}}, \quad (48)$$

transform the imaginary parts of the Green function (local mode density) into the propagator of virtual photons. This change to the imaginary frequency axis provide the interpretation of the dispersion forces via an exchange of virtual photons via closed loops due to the coincidence limit that source and field points coincide $\boldsymbol{r}' \mapsto \boldsymbol{r}$. Inserting the separation of the Green function into its bulk and scattering part, $\mathbf{G} = \mathbf{G}^{(0)} + \mathbf{G}^{(S)}$, and applying the Born-series expansion,[334] analogously to Eq. (43), the Casimir force (48) transforms to the well-known Lifshitz formula (14) dis-

cussed in Sec. 4.1. These forces are usually measured via atomic force microscopes, see Sec. 3.1, and dominate the interactions in MEMS and NEMS, see Sec. 2.5.

Casimir–Polder force: appears between a polarisable object, which can be described via Eq. (38), and a dielectric surface entering the theory via the induced electromagnetic fields, Eq. (33). Both systems are described via the Fock state $|I\rangle = |k\rangle |\{n\}\rangle$, as the product state of the particles and field states $|k\rangle$ and $|\{n\}\rangle$, respectively. Both systems are typically coupled perturbatively with the leading second-order

$$\Delta_2 E = \langle \hat{H}_{\text{int}} \rangle_2 = \sum_{I \neq G} \frac{\langle G| \hat{H}_{\text{int}} |I\rangle \langle I| \hat{H}_{\text{int}} |G\rangle}{E_I - E_G}, \qquad (49)$$

with the initial ground state $|G\rangle = |0\rangle |\{0\}\rangle$ and the intermediate state $|I\rangle = |k\rangle |1(\mathbf{r}, \omega)\rangle$ containing a single excitation for the particle $|k\rangle$ and a single-photon field excitation $|1(\mathbf{r}, \omega)\rangle$. Thus, the energy change induced by the field reads[334]

$$\Delta E = \frac{\mu_0}{\pi} \sum_k \int_0^\infty \frac{d\omega}{\omega_k + \omega} \mathbf{d}_{0k} \cdot \left\{ \omega_k \omega \left[\text{Im} \mathbf{G}(\mathbf{r}_A, \mathbf{r}_A, \omega) \right. \right.$$

$$\left. \left. - \text{Im}^\parallel \mathbf{G}^\parallel(\mathbf{r}_A, \mathbf{r}_A, \omega) \right] - \omega^2 \text{Im}^\parallel \mathbf{G}^\parallel(\mathbf{r}_A, \mathbf{r}_A, \omega) \right\} \cdot \mathbf{d}_{k0}, \qquad (50)$$

where we omit the index for the order of the perturbation. By splitting the Green function into its bulk (free-space) and scattering part, $\mathbf{G} = \mathbf{G}^{(0)} + \mathbf{G}^{(S)}$, the position independent part (free-space Green function) $\text{Im} \mathbf{G}^{(0)}(\mathbf{r}, \mathbf{r}, \omega) = \frac{\omega}{6\pi c} \mathbb{I}$ yields the Lamb-shift[345]

$$\Delta E = \frac{\mu_0}{6\pi^2 c} \sum_k \omega_k^3 |\mathbf{d}_{0k}|^2 \ln \left(\frac{m_e c^2}{\hbar \omega_k} \right). \qquad (51)$$

The remaining position-dependent part of the energy shift is the Casimir–Polder potential which reads after applying contour integration techniques[334]

$$U(\mathbf{r}_A) = \frac{\hbar \mu_0}{2\pi} \int_0^\infty d\xi \, \xi^2 \text{Tr} \left[\alpha(i\xi) \cdot \mathbf{G}(\mathbf{r}_A, \mathbf{r}_A, i\xi) \right], \qquad (52)$$

where we omitted the superscript (S) for the scattering part of the Green function and used Eq. (42) to introduce the particle's polarisability. These forces are involved in all situations where neutral particles get close to dielectric objects, such as particles in surfaces, see Sec. 2.1, or scattering of matter waves, see Secs. 3.2 and 3.3.

Van der Waals force: arises between two neutral quantised objects which classically do not interact. Due to the selection rules of the dipole operator, which couples only different states, the perturbative approach (as followed for the Casimir–Polder interaction) yields the fourth order with a non-vanishing contribution. Details about this approach can be found in Ref. [342] However for an intuitive understanding, a simpler approach starts from the Casimir–Polder interaction (52) and applying the dilute limit of the interacting dielectric surface. In this case, the corresponding

Green function is given by Eq. (43) leading the vdW potential[334]

$$U_{\text{vdW}}(\mathbf{r}_A, \mathbf{r}_B) = -\frac{\hbar \mu_0^2}{2\pi} \int_0^\infty d\xi \, \xi^4 \text{Tr} \left[\alpha_A(i\xi) \right.$$

$$\left. \cdot \mathbf{G}(\mathbf{r}_A, \mathbf{r}_B, i\xi) \cdot \alpha_B(i\xi) \cdot \mathbf{G}(\mathbf{r}_B, \mathbf{r}_A, i\xi) \right], \qquad (53)$$

which again can be interpreted as an exchange of virtual photons, that are created at particle A, transmitted to particle B, where they interact via its polarisability α_B, and propagate back to particle A and interact. The sum (integral) over all these scattering processes yields the vdW potential. These forces determine the structure of van der Waals heterostructures, Sec. 2.2.

Dispersion forces, in general, have been widely studied in theory[16,282,336,346–348] and experiments.[227,231,349–351] Hence, we do not want to overstress their further discussions. However, to end this section, we will discuss finite-size effects for microscopic particles and the transition between different dispersion forces. Most relevant systems described in this review deal with bounded particles or at least in very close separation. Thus, the typical relevant length scales are of the same order as the extension of the particles leading to a breakdown of the point-particle assumption. In classical electrodynamics, there are different ways to account for finite system sizes represented by a collection of charges, namely the multipole expansion[335]

$$\phi(\mathbf{r}) = \frac{1}{4\pi} \left[\frac{1}{r} q + \frac{\mathbf{r} \cdot \mathbf{d}}{r^3} + \frac{\mathbf{r} \cdot \mathbf{Q} \cdot \mathbf{r}}{2r^5} + \ldots \right], \qquad (54)$$

with the charge q, the dipole moment $\mathbf{d}$, and the quadrupole moment $\mathbf{Q}$. The impact of higher-order multipoles are discussed in the literature, for instance in Ref. [352]. An alternative approach to include higher-order of moments follows from finite-size effects of the particles via a spatially smeared out dielectric polarisability $\alpha = \alpha(\mathbf{r}, \omega)$,[353] see sec. 4.2.2. By taking into account the finite size of a particle, the dispersion interactions get corrected in a series corresponding to higher-order moments.[351,354–356]

4.4.2 Radiative decays

An important process for nanoparticles near interfaces is the change of optical properties, such as spectral detunings or change excitation lifetimes. One is the Purcell effect,[357,358] i.e., the environmental influence on the decay rate of an excited state. While this can be viewed as a single-particle effect in an effective environment, the collective effects of an ensemble of particles superradiance,[45,359,360] as used in experiments reported in Sec. 2.1 and used in nano-structured solar cells, see Sec. 2.4. These properties can be addressed within mQED via the internal quantum mechanical dynamics of a particle in the presence of dielectric bodies, we obtain the Hamiltonian 32) by separation into the subsystems: the atomic system (38)

$$\hat{H}_A = \sum_n E_n |n\rangle \langle n| = \sum_n E_n \hat{A}_{nn}, \qquad (55)$$

with atomic flip operator $\hat{A}_{mn} = |n\rangle \langle m|$; the electromagnetic fields $\hat{H}_{\mathrm{F}}$ (33); and the atom-field coupling $\hat{H}_{\mathrm{int}} = -\hat{\boldsymbol{d}} \cdot \hat{\boldsymbol{E}}(\boldsymbol{r}_{\mathrm{A}})$,

$$\hat{H} = \hat{H}_{\mathrm{A}} + \hat{H}_{\mathrm{F}} + \hat{H}_{\mathrm{AF}}. \tag{56}$$

To obtain the internal atomic dynamics, Heisenberg's equations of motion [338]

$$\hat{A}_{mn} = \frac{1}{\mathrm{i}\hbar} \left[\hat{A}_{mn}, \hat{H}\right]$$

$$= \mathrm{i}\omega_{mn}\hat{A}_{mn} + \frac{\mathrm{i}}{\hbar} \sum_{k} \left(\hat{A}_{mk}\boldsymbol{d}_{nk} - \hat{A}_{kn}\boldsymbol{d}_{km}\right) \cdot \hat{\boldsymbol{E}}(\boldsymbol{r}_{\mathrm{A}}). \tag{57}$$

By solving the system of coupled equations of motion (57) and splitting the result into its imaginary and real part, one obtains, the atomic frequency shifts for the nth excited state [341]

$$\Delta\omega_n = -\frac{\mu_0}{\hbar} \sum_{k} \omega_{nk}^2 \boldsymbol{d}_{nk} \cdot \operatorname{Re}\mathbf{G}(\mathbf{r}_A, \mathbf{r}_A, \omega_{nk}) \cdot \boldsymbol{d}_{kn}$$

$$+ \frac{\mu_0}{\pi\hbar} \sum_{k} \int_0^\infty \mathrm{d}\xi \frac{\omega_{kn}\xi^2}{\omega_{kn}^2 + \xi^2} \boldsymbol{d}_{nk} \cdot \mathbf{G}(\mathbf{r}_A, \mathbf{r}_A, i\xi) \cdot \boldsymbol{d}_{kn}, \tag{58}$$

and the transition rate

$$\Gamma_n = \frac{2\mu_0}{\hbar} \sum_{k<n} \omega_{nk}^2 \boldsymbol{d}_{nk} \cdot \operatorname{Im}\mathbf{G}(\boldsymbol{r}_A, \boldsymbol{r}_A, \omega_{nk}) \cdot \boldsymbol{d}_{kn}. \tag{59}$$

The spectral detuning (58) is the sum of the resonant and the non-resonant of the particle's state with the field. The change of the transition rate (59) is due to the coupling of the states with lower energies. The transition rate is the inverse of the excitation decay $\tau = 1/\gamma$. Thus, the excitation lifetime changes to $\tau \to 1/(\gamma + \Gamma_n)$. At binding separation, the local mode density is typically a positive quantity. Hence, a dielectric object results in a reduction of the excitation lifetime. The simultaneous consideration of both effects is only relevant if the observed transition ω_{kn} is closed a resonance of the dielectric object. In this case, the impact of the detuning $\delta\omega_{kn}$ on the local mode density $\operatorname{Im}\mathbf{G}(\boldsymbol{r}_A, \boldsymbol{r}_A, \omega_{nk} + \delta\omega_{nk})$ gets relevant.

The resulting changes of the resonances frequencies (58) and transition rates (59) can be interpreted as an environmental induced state mixing. Especially, the energy change is equivalent to the Casimir–Polder force of excited particles. [356]

4.4.3 Dielectric function from density functional theory

To determine the macroscopic dielectric function $\varepsilon(\boldsymbol{r}, \omega)$ within the DFT, it is common to consider the linear response of the internal electric field to the external electric field: $\boldsymbol{E}_{\mathrm{int}}(\boldsymbol{q}, \omega) = \varepsilon^{-1}(\boldsymbol{q}, \omega)\boldsymbol{E}(\boldsymbol{q}, \omega)$. In the long-wavelength limit ($\boldsymbol{q} \to 0$) and with the independent single-electron eigenfunctions, the response due to interband transitions is the joint density-of-states modulated by the optical matrix elements. For nonlocal potentials or self-energies, the linear momentum operator is replaced by the velocity (or the position) operator. Local field effects are typically neglected. The imaginary part of the dielectric tensor can then be

computed as [361]

$$\varepsilon_{\alpha\beta}^{''\,\mathrm{inter}}(\omega) = \lim_{\boldsymbol{q}\to 0} \frac{4\pi^2 e^2}{V_\Omega q^2} \sum_{v,c,\boldsymbol{k}} \delta(\epsilon_{c,\boldsymbol{k}} - \epsilon_{v,\boldsymbol{k}} - \hbar\omega)$$

$$\times \langle u_{c,\boldsymbol{k}+\boldsymbol{e}_\alpha q}|u_{v,\boldsymbol{k}}\rangle \langle u_{v,\boldsymbol{k}}|u_{c,\boldsymbol{k}+\boldsymbol{e}_\beta q}\rangle, \tag{60}$$

where V_Ω is the unit cell volume, $\boldsymbol{e}_\alpha$ is the Cartesian unit vector, and $u_{v/c}$ is the cell periodic part of the eigenfunction with energy $\epsilon_{v/c}$ for the valence (v) or conduction (c) band state.

For ionic materials, there is a contribution to the dielectric response from the dipole-active phonon modes. The vibrations associated with the longitudinal optical phonons build up an electric field that screens the carries. In the long-wavelength limit the phonon dispersion is approximated to be constant for both the longitudinal optical (LO) and the transverse optical (TO) modes. The contribution to the imaginary part of the dielectric function can be modelled as Lorentz oscillators

$$\varepsilon^{''\,\mathrm{ph}}(\omega) = \sum_j \frac{S_j\,\omega_{\mathrm{TO}}^2\Gamma_j\omega}{(\omega_{\mathrm{TO}}^2 - \omega^2)^2 + \Gamma_j\omega^2}, \tag{61}$$

where Γ_j is the damping and S_j is the oscillator strength of the jth mode in its vibration direction. Typically for *ab initio* calculations, the density functional perturbation theory is employed to compute the response for the Hessian matrix of ionic displacements.

For metals, the Drude theory with the plasma frequency ω_{pl} describes the intraband screening from the nearly free carriers in the partially occupied band

$$\varepsilon^{''\,\mathrm{intra}}(\omega) = \frac{\Gamma\omega_{\mathrm{pl}}^2}{\omega(\omega^2 + \Gamma^2)}. \tag{62}$$

The total imaginary part of the dielectric function, $\varepsilon_{\alpha\beta}^{''}(\omega)$, is the summation of the three contributions. The corresponding response function for imaginary frequencies is obtained from the Kramers–Kronig relation

$$\varepsilon_{\alpha\beta}(\mathrm{i}\xi) = 1 + \frac{2}{\pi} \int_0^\infty \frac{\omega\,\varepsilon_{\alpha\beta}^{''}(\omega)}{\omega^2 + \xi^2}\,d\omega. \tag{63}$$

In this work, the geometric average $\varepsilon(\mathrm{i}\xi)$ has been considered.

The summation over the $\boldsymbol{k}$-mesh in Eq. (60) is a computational challenge. For bulk-like materials, the summation can be replaced by an integration over the first Brillouin zone, however, the issue to compute the eigenstates for sufficiently many $\boldsymbol{k}$-points remains. The reasons are, first, energy band crossing yields incorrect integration for each band. This could be avoided by analysing the symmetry of the eigenfunctions [362] and reordering the energy states. Second, a compact $\boldsymbol{k}$-mesh is required for metals in order to accurately determine the Fermi level, especially when several bands are partially filled. [363] Third, since the energy bands have quadratic dispersion around band extrema, i.e., $\epsilon_{j,\boldsymbol{k}} \propto \boldsymbol{k}^2$, the density-of-states should there be proportional to the square root of the energy. The linear tetrahedron integration is a standard algorithm, however assuming a linear dispersion $\epsilon_{j,\boldsymbol{k}} \propto |\boldsymbol{k}|$ implies that the density-of-states is direct proportional to the square of

Physical Chemistry Chemical Physics Accepted Manuscript

the energy. A dense k-mesh is therefore required to account for details in the energy dispersion.[364] Further, for a nano-sized material, assuming Bloch functions and neglecting surface effects, the summation over the k-points is still demanding unless the material comprises only a moderate number of unit cells.

To compute the energy states for a dense k-mesh is time consuming with hybrid functionals, GW approaches, or other beyond-DFT methods. There are different approaches to address this issue, for instance, polynomial fitting,[365] smoothed Fourier interpolation,[366] construction of optimal basis,[367] or Wannier-like functions.[368] A straightforward method is the full-band $k \cdot p$ calculation.[363,369] The scheme is to perform a DFT calculation for a sparsely sampled k-mesh, whereupon the energy states for the dense k-mesh are determined by describing those states as linear combinations of the DFT eigenfunctions. The method generates exact results if an infinite number of bands is used, but already for a rather modest number of bands the $k \cdot p$ calculations yield accurate results, describing also band crossing.

4.4.4 Polarisable Continuum Model

The polarisable continuum approach (PCM)[370], or the related Conductor-like Screening Model (COSMO)[371,372], is computationally inexpensive method to calculate properties of solvated molecules or surfaces, see Fig. 13. The solvent is modelled solely by its relative permittivity ε_M (subscript M for medium), which can have a large impact on the electronic states. In particular for the arguably most important solvent, water, with its static polarisability of $\varepsilon \approx 80$, the PCM e.g. correctly describes the stabilisation of the zwitterionic form of proteins.[373]

An environmental solvent has, in general, two effects on a dissolved ensemble: (i) restraining of the electronic wave functions and the electron density, and (ii) screening of the long-range interactions through the medium[374].

While dispersive contributions between solute and solvent are important to obtain accurate solvation energies, dispersive interactions between different solutes have so far received less attention. The PCM influences electric fields,[375] where e.g. the Coulomb energy of point charges embedded within a continuous ε at distance R is screened by $1/\varepsilon$ largely stabilising local charges. This continuum assumption opens the field of access polarisability models[283] considering local-field effects at the particles. These models describe effectively the impact of the surrounding media on the interactions via an effective dielectric response of the particle. The established model is Onsager's real cavity model[376] assuming a point-like particle embedded in a vacuum bubble of finite radius. This assumption is questionable due to finite particle size leading to more complex models[283] and concerning the hard wall.[377,378] Similar to point charges screening occurs also for dispersive interactions, where one expects screening by $1/\varepsilon(\omega_{opt})^2$ with the frequency ω_{opt} in the optical range for usual molecular systems.[374,379] Water has $\varepsilon(\omega_{opt}) \approx 1.7$, such that the screening is much less than for pure Coulomb fields. A comprehensive experimental and theoretical study concerning correct assumptions for such models is still required.

4.5 Cavity QED

The interaction of atoms or molecules with the electromagnetic field is, to lowest order in the perturbative expansion of the light-matter coupling, determined by the electric-dipole interaction $\hat{H}_{int} = -\hat{\boldsymbol{d}} \cdot \hat{\boldsymbol{E}}(\boldsymbol{r}_A)$, with the electric field taken at the position $\boldsymbol{r}_A$ of the atom. In view of second-order perturbation theory with this interaction Hamiltonian, it is clear that the interaction strength crucially depends on the local density of states (LDOS) of the electromagnetic field (see also the discussion on dispersion forces, Sec. 4.4.1). In a situation in which the light field is confined in a resonator-like structure, the density of field modes can be very sharply peaked around one or more discretely spaced frequencies. If that cavity mode is resonant with a particular atomic transition, the light-matter interaction can be treated in a two-level approximation for the atom, and a single-mode approximation for the field.

Within the framework of macroscopic quantum electrodynamics, one can define position-dependent ladder operators for photon-like excitations as[380]

$$\hat{a}(\boldsymbol{r},\omega) = -\frac{1}{\hbar g(\boldsymbol{r},\omega)} \sum_\lambda \int d^3 r' \boldsymbol{d} \cdot \mathbf{G}_\lambda(\boldsymbol{r},\boldsymbol{r}',\omega) \cdot \hat{\boldsymbol{f}}_\lambda(\boldsymbol{r}',\omega) \quad (64)$$

with the coupling constant

$$g(\boldsymbol{r},\omega) = \sqrt{\frac{\mu_0}{\hbar\pi} \boldsymbol{d} \cdot \text{Im}\mathbf{G}(\boldsymbol{r},\boldsymbol{r},\omega) \cdot \boldsymbol{d}^*} . \quad (65)$$

From this expression, the coupling strength is seen to explicitly contain the LDOS $\propto \text{Im}\mathbf{G}(\boldsymbol{r},\boldsymbol{r},\omega)$. The ladder operators define single-quantum field excitations $|\boldsymbol{r},\omega\rangle = \hat{a}^\dagger(\boldsymbol{r},\omega)|\{0\}\rangle$. In the limit of a sharply peaked LDOS with a Lorentzian profile around a centre frequency ω_c with width γ,

$$g^2(\boldsymbol{r},\omega) = g^2(\boldsymbol{r},\omega_c) \frac{\gamma^2/4}{(\omega-\omega_c)^2 + \gamma^2/4} , \quad (66)$$

one can construct photon-like single-excitation states as

$$|1\rangle = \sqrt{\frac{\gamma}{2\pi}} \int_\gamma \frac{d\omega}{\sqrt{(\omega-\omega_c)^2 + \gamma^2/4}} |\boldsymbol{r}_A,\omega\rangle . \quad (67)$$

In the subspace containing at most one excitation, and on timescales on which relaxation processes can be neglected, the interaction is equivalent to the Jaynes–Cummings model[381,382] with the Hamiltonian

$$\hat{H} = \hbar\omega_c\hat{a}^\dagger\hat{a} + \frac{1}{2}\hbar\omega_A\hat{\sigma}_z + \hbar g\left(\hat{a}\hat{\sigma}^\dagger + \hat{a}^\dagger\hat{\sigma}\right) \quad (68)$$

in which a single field mode $\hat{a}$ with frequency ω_c couples to a two-level atomic transition with frequency $\omega_A \approx \omega$. In this model, the transitions between the energy levels of the two-level atom with ground state $|g\rangle$ and excited state $|e\rangle$ are described by transition operators $\sigma = |g\rangle\langle e|$ and $\hat{\sigma}^\dagger = |e\rangle\langle g|$, and $\sigma_z = |e\rangle\langle e| - |g\rangle\langle g|$ denotes the atomic inversion operator. The coupling strength g $(= \sqrt{\pi\gamma g^2(\boldsymbol{r}_A,\omega_c)}/2$ in the framework of macroscopic QED[380]) is given by the overlap of the atomic transition dipole moment and the cavity electric field. As we have assumed near resonance between atomic transition and the cavity mode, we have

employed the rotating-wave approximation and dropped the off-resonant, counter-rotating terms that would ordinarily be present in the electric-dipole Hamiltonian (for ultra-strong coupling, this assumption is no longer valid and has to be relaxed, leading to the Tavis–Cummings model[383]).

The Jaynes–Cummings model is a rare example of an exactly solvable model of interacting quantum systems. The Hamiltonian (68) is block-diagonal in the basis of atom-field states $\{|n,e\rangle, |n+1,g\rangle\}$ containing either n photons and with the atom in its excited state, or the field containing $n+1$ photons on the expense of the atom residing in its ground state,

$$\hat{H}\begin{pmatrix}|n,e\rangle \\ |n+1,g\rangle\end{pmatrix} = \hbar \begin{pmatrix} n\omega_c + \frac{1}{2}\omega_A & -g\sqrt{n+1} \\ -g\sqrt{n+1} & (n+1)\omega_c - \frac{1}{2}\omega_A \end{pmatrix}\begin{pmatrix}|n,e\rangle \\ |n+1,g\rangle\end{pmatrix}. \tag{69}$$

The eigenvalues of the Hamiltonian matrix are

$$\hbar\omega_{n,\pm} = \hbar\omega_c\left(n+\frac{1}{2}\right) \pm \frac{1}{2}\hbar\Delta_n \tag{70}$$

with the Rabi splitting $\Delta_n = \sqrt{\delta^2 + \Omega_n^2}$ that depends on the detuning $\delta = \omega_A - \omega_c$ of the atomic transition from the cavity resonance, and the n-photon Rabi frequency $\Omega_n = 2g\sqrt{n+1}$. Its eigenstates are linear combinations of the unperturbed states

$$\begin{pmatrix}|n,+\rangle \\ |n,-\rangle\end{pmatrix} = \begin{pmatrix}\cos\Theta_n & \sin\Theta_n \\ -\sin\Theta_n & \cos\Theta_n\end{pmatrix}\begin{pmatrix}|n,e\rangle \\ |n+1,g\rangle\end{pmatrix} \tag{71}$$

with the rotation angles

$$\sin\Theta_n = \frac{\Omega_n}{\sqrt{(\Delta_n - \delta)^2 + \Omega^2}}, \quad \cos\Theta_n = \frac{\Delta_n - \delta}{\sqrt{(\Delta_n - \delta)^2 + \Omega^2}}. \tag{72}$$

At exact resonance, $\delta = 0$, the unperturbed states are pairwise degenerate, except for the lowest-energy state $|0,g\rangle$ that is not coupled to any other state. This degeneracy is now lifted by the atom-field interaction, and the level splitting equals the n-photon Rabi frequency $\Omega_n = 2g\sqrt{n+1}$. It is worth noting that even in the absence of a photon, $n=0$, the eigenstates $|0,\pm\rangle$ are split by the vacuum Rabi splitting $\Omega_0 = 2g$. At exact resonance, the exact eigenstates (or dressed states) are (anti-)symmetric combinations of the unperturbed states $|0,\pm\rangle = (\mp|0,e\rangle + |1,g\rangle)/\sqrt{2}$.

Because the Jaynes–Cummings model is exactly solvable, the resulting unitary evolution is also known exactly.[334] Its experimental verification[384] using superconducting microwave cavities and circular Rydberg atoms has been remarkably successful, and included the generation of maximally entangled pairs of atoms[385] as well as of Schrödinger cat-like states between an atom and the radiation field,[386] the development of a single-atom single-photon quantum interface[387] or the observation of photon blockade[388] in a cavity.

More recently, it has been realised that the strong coupling to light in a cavity also influences the dynamics of chemical reactions[177,180,181] which led to the development of the field of polaritonic chemistry or QED chemistry.[179] The strong coupling to the cavity field can be used to control chemical reaction rates[177] or energy-transfer rates between molecules.[182] These developments opened up a new field in which even the engineering of

novel quantum materials becomes feasible.[183] What has started out as a model system in quantum optics, strong coupling to light fields has turned into an important tool in fields ranging from quantum information processing and quantum engineering to QED-enhanced chemistry.

4.6 Prediction of molecular aggregate structures

A fascinating field of experimental applications is to use the ability of weakly interacting molecules to self-organise on interfaces and surfaces (see, e.g., sections 2.1, 2.2, 2.4, 2.3).[39,93] The resulting structures are often stable at elevated temperature and can therefore be produced at air-water interfaces[78,79] or within liquid environments[389–391]. The latter allows for electrochemical control that gives an additional handle on the variety of structures that can be achieved.[392] Theoretical descriptions of such aggregates are mostly based on modelling experimentally observed patterns, but efforts for ab initio theoretical predictions of molecular aggregate structures are less frequent. Such a possibility would be an essential prerequisite to develop molecular target structures that will exhibit tailored photonic and electronic properties as materials (see section 2.4 on solar cells). Usually, geometries of small aggregates are created manually, extracted from experimental crystal structures, or are identified by searching for minima on the energy hypersurface. Due to the obvious drawbacks of the first two ways, namely limitation by chemical intuition and availability of crystal structures, an overview of currently available methods for theoretical determination of aggregate structures is given here.

An established method to determine energetically favourable, hence frequently appearing, aggregate structures are molecular dynamics (MD) simulations[393], but they are often very time-consuming and have deficiencies in the accurate description of dispersion interactions. Faster coarse-grained simulations do not always allow a simple back-mapping of the coarse structure to the underlying atomistic structure.[394–396] Alternatively, the energy hypersurface of dimers might be explicitly sampled, what can be very demanding also. Therefore, fitting approaches that necessitate only a few quantum chemical calculations of possible dimer structures and approaches where multiple dimer structures are created randomly or systematically have been developed.[397,398]

In one of such systematic approaches, all possible dimers of a pre-defined spatial (e.g., $100 \times 100 \times 100$ points) and rotational grid (e.g., yielding $10^6 \times 10 \times 10 \times 10$ total grid points) are energetically evaluated with force fields methods as implemented in the OpenBabel program. The program EnergyScan,[399] which utilises OpenBabel libraries, efficiently identifies energetically favourable and geometrically distinct dimer structures. For the case of urea, identical dimers have been identified as through extensive MD runs,[393] but π-stacks are not properly recognised as energetically favourable due to deficiencies of the force fields.[399] For the example of porphin, approximately 6400, 3260, and 1900 energy evaluations can be performed per second and thread on a desktop computer (year 2018) for a dimer, a trimer, and a quadrumer of porphin, respectively. To properly identify all relevant aggregate structures, i.e., those bound by dispersion forces, supplementary

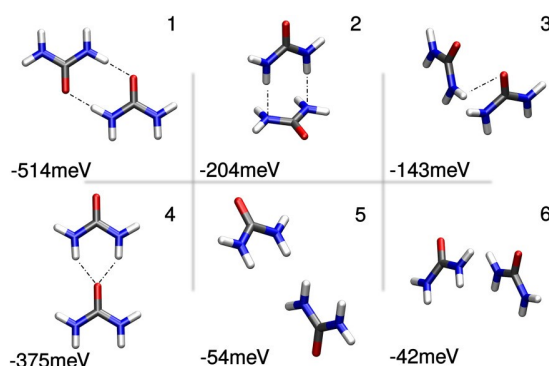searches based on DFT (see section 4.3) or other methods (see section 4.4.1) are necessary.

Fig. 14 Local energy minimum geometries and associated binding energies of urea dimers as found by EnergyScan with subsequent quantum chemical optimisation. The first four types are urea-urea pair-conformations known from the literature, the first three of which have been identified in literature through extensive MD simulations. Dot-dashed lines indicate hydrogen bonds. Reprinted with permission from Sachse *et al.*[399], Copyright (2018) John Wiley and Sons.

Upon increasing the concentration of organic dyes in solution, the individual dye molecules can self-assemble in supramolecular structures (e.g., cylinders) consisting of thousands of molecules.[400] The resulting structure depends on an intricate interplay between the morphology of the dye molecules, entropic effects, electrostatic and dispersive interactions. Direct imaging of these fragile structures is a difficult task and therefore, typically a combination of optical spectroscopy techniques are used to obtain information about possible structures.[400–404] A promising future direction is the application of machine-learning methods to extract the arrangement of the molecules of the aggregate from optical spectra and theoretical calculations Ref. [405]. In recent years, these spectroscopic approaches have been amended by Cryo-STM images[406,407] and also first steps have been made to investigate the stability of predicted structures using molecular dynamics simulations.[408–413]

4.7 Ensembles of highly excited atoms

In nearly all of the examples discussed in this review, the dispersion forces are mostly relevant at small distances in the nanometer range. Highly excited atoms (so called Rydberg atoms) are paradigmatic systems to precisely study dispersion interactions, which manifest themselves even at interatomic distances in the order of several micrometers. This is because of the huge polarisability of such Rydberg atoms, which scales roughly as n^7, where n is the principal quantum number of the Rydberg electron.

This long-range interaction leads for example to the formation of macrodimers[414,415] and it is important for the implementation of quantum gates.[416–419] Ensembles of Rydberg atoms can for example be excited in ultra-cold gases or Bose-Einstein condensates. Here, the long range interactions play a crucial role in forming correlated distributions of the excited atoms. In recent years it became also possible to create arrangements of Rydberg atoms in nearly arbitrary arrangements using optical lattices or tweezer arrays.[420,421]

To get a feeling about the most relevant aspects of the long-range interactions between Rydberg atoms, we will discuss the example of alkali atoms (such as lithium or rubidium), which are commonly used in experiments. Alkali atoms are hydrogen-like, with their single valence electron moving in a modified Coulomb potential because of the polarisability of the core electrons.[422] The size of their wavefunction scales with n^2. As it is common to work in experiments with principal quantum numbers in the range from $n = 20$ up to $n = 200$, their classical Bohr radius of roughly 1μm for $n = 200$ makes them mesoscopic quantum objects.

In the following we consider two atoms, denoted by A and B. Their quantum evolution is governed by the Hamiltonian $H = H_A + H_B + V_{\text{int}}$, where H_A and H_B are the Hamiltonians of the individual atoms [Eq. (38)] and V_{int} is the interaction between the two atoms. We consider the case in which the distance between the atoms located at R_A and R_B is so large that there is negligible overlap of their wavefunctions[423], i.e. we assume $R = |\mathbf{R}| = |\mathbf{R}_A - \mathbf{R}_B| > 2(\langle r_A^2 \rangle^{1/2} + \langle r_B^2 \rangle^{1/2})$, where the coordinates of the valence electron of each atom with respect to the position of the atom core are denoted by $\mathbf{r}_A$ and $\mathbf{r}_B$, respectively. On the other hand, we restrict ourselves to distances where retardation effects of the interaction between the two atoms can be neglected. This distance can be estimated[424] by $R_{\text{ret}} \approx (n - \delta_l)^3/(8\pi \text{Ry})$ with Ry the Rydberg constant of the respective atom and δ_l the quantum defect, which depends on the angular momentum state l. For distances $|\mathbf{R}_A - \mathbf{R}_B| < R_{\text{ret}}$, the interaction between the atoms is approximated as the sum of the Coulomb interactions between the positively charged cores and the Rydberg electrons which is conveniently expressed in terms of interactions between the multipoles of the individual atoms. For not too small separations between the atoms, the dominant term is the dipole-dipole interaction $V_{\text{int}} \approx \frac{e^2}{R^3}\left[\mathbf{r}_A \cdot \mathbf{r}_B - 3(\mathbf{r}_A \cdot \mathbf{R})(\mathbf{r}_B \cdot \mathbf{R})/R^2\right]$. At these distances, one can perform second-order perturbation theory[425] with respect to the eigenstates of the individual atoms $|n_A, l_A, j_A, m_A\rangle|n_B, l_B, j_B, m_B\rangle$, where n, l, j and m denote the principal quantum number, the orbital angular momentum, the total angular momentum and the corresponding magnetic quantum number of the individual atoms, respectively. The energy of such a state is $E_{n_A, l_A, j_A} + E_{n_B, l_B, j_B}$ and is independent of the magnetic quantum numbers m_A and m_B. Let us first consider the case when both atoms have the same quantum numbers n, l, and j, i.e., they have the same energy $E_{n,l,j}$ and the unperturbed energy of the pair state is $2E_{n,l,j}$, which is $(2j+1)^2$ fold degenerate. Consider for example the case when both atoms are in a state with principal quantum number n state and angular momentum $l = 0$. Ignoring the fine structure splitting and the magnetic quantum numbers, the second-order expression for the energy correction becomes[425–427]

$$E_{n\text{S}}^{(2)} \approx -\frac{C_6}{R^6},\tag{73}$$

where the C_6-coefficient is given by

$$C_6 = C_6(n\text{S}) = 6\sum_{n_A, n_B}\frac{\left|\langle n\text{S}|d_z|n_A\text{P}\rangle\right|^2 \left|\langle n\text{S}|d_z|n_B\text{P}\rangle\right|^2}{E_{n_A\text{P}} + E_{n_B\text{P}} - 2E_{n\text{S}}}.\tag{74}$$

where, we have taken the atoms to be located on the z-axis and d_z denotes the z-component of the dipole operator of the respective atom which, by the usual selection rules, couples only to states with angular momentum $l = 1$. For $n > 20$, the dominant contributions to the sum stem from states with principal numbers n_A and n_B close to n, typically $|n_{A/B} - n| < 10$. The fractional contribution of the remaining terms (together with the integral over the continuum) is usually smaller than 10^{-4}. In contrast to the vdW interaction between atoms/ molecules in their ground states, for the case of excited atoms the denominator $E_{n_A P} + E_{n_B P} - 2E_{nS}$ can become positive as well as negative. For this reason, the C_6-coefficient can be positive or negative and scales as n^{11} with the principal quantum number. Similar results hold for other low angular momentum states nP, nD and nF. For some combination of states, the denominator becomes very small so that one has to use degenerate (first-order) perturbation theory (for example for the $38P_{3/2}$ state of rubidium). This results in a deviation from the $1/R^6$ scaling and a cross-over to a $1/R^3$ behaviour. For non-zero angular momentum states the C_6-coefficient becomes a tensor with respect to the magnetic quantum numbers.[425] For heavy atoms (rubidium, caesium), the tensor character can also arise for the $nS_{1/2}$ state because of the large fine structure splitting.

So far, we discussed the dispersion interaction for the case when both atoms are in the same Rydberg state. If the atoms are in angular momentum states that differ by one, then one of the pair states are degenerate and one has first diagonalise the respective subspaces, which results in a $1/R^3$ distance scaling.

Many recent experiments are performed at rather small distances and with such a precision that perturbative calculations as well as restrictions to the leading dipole–dipole interaction term are no longer sufficient. Then, diagonalisation within a suitable two-particle basis is the method of choice. In Refs. [424,428,429], relevant aspects of such calculation for Rydberg energy potential surfaces are reviewed. One finds that overall the eigenenergies and eigenstates as function of distance show a rich behaviour with strong state mixing at small distances, and even at larger distances different power laws can appear. This picture is even more complicated when the Rydberg atoms are close to a surface[430] or when more than two Rydberg atoms are involved.

Experimentally, there is a long tradition to investigate the van der Waals interaction between Rydberg atoms and surfaces.[431,432] Recently, it has also become possible to investigate the interaction between two individual Rydberg atoms.[433,434] Good agreements between experiment and numerical results based on the full diagonalisation in a large basis have been found.

5 Conclusions

This review aims to give an overview of weak (non-covalent) interactions, demonstrating the role they have played in recent research projects. Due to the huge variety in different applications, such as nano-structured materials for solar cells, sec. 2.4, vdW heterostructures, sec. 2.2, micro- and nano-electro-mechanical systems, sec. 2.5, and electrochemical transistors, sec. 2.3, (to name some applications discussed in this article) via interactions on surfaces, sec. 2.1, self-organisation, sec. 4.6 and many besides, this topic is studied from different perspectives that we want to

bring closer together. We introduced the research topic with a summary of the terminologies used in various scientific communities, sec. 1. We illuminated their investigations by discussing effects, such as Rabi splitting, sec. 2.6, or superradiance, sec. 2.1, and characterisation methods such as microscopy, sec. 3.1, helium scattering, secs. 3.2 and 3.3, and back-focal plane imaging, sec. 2.3. Finally, we summarised different theories describing these materials and their dielectric properties. Here, we focused on microscopic modelling via density functional theory, sec. 4.3, and their propagation to larger scales in the mean-field approximation, sec. 4.6, and via statistical methods, sec. 4.1, and macroscopic quantum electrodynamics, sec. 4.4. These models work best in a vacuum, whereas most experiments occur in a solution or are strongly influenced by a surrounding medium. To this end, we illustrated extensions to continuum models, sec. 4.4.4, and included an entire chapter on interactions between colloids, sec. 4.2, and finalised the manuscript with an outlook on field enhancements via cavities leading to strong coupling, sec. 4.5, and effects caused by highly excited (Rydberg) atoms, sec. 4.7. Finally, weak interactions in complex materials are a vast topic and studied by many different scientists. This article cannot reflect the entire research, but we are confident that it supports the exchange between the involved researchers.

Author Contributions

Conflicts of interest

There are no conflicts to declare.

Acknowledgements

Notes and references

1　E. Klampaftis, D. Ross, K. R. McIntosh and B. S. Richards, *Sol. Energy Mater. Sol. Cells*, 2009, **93**, 1182–1194.

2　S. Izadnia, D. W. Schönleber, A. Eisfeld, A. Ruf, A. C. LaForge

and F. Stienkemeier, *J. Phys. Chem. Lett.*, 2017, **8**, 2068–2073.

3 F. Stienkemeier and K. K. Lehmann, *J. Phys. B: At. Mol. Opt. Phys.*, 2006, **39**, R127.

4 P. Moraitis, R. Schropp and W. van Sark, *Opt. Mat.*, 2018, **84**, 636–645.

5 P. K. Nayak, S. Mahesh, H. J. Snaith and D. Cahen, *Nat. Rev. Mat.*, 2019, **4**, 269–285.

6 A. Zatirostami, *J. Alloys Compd.*, 2020, **844**, 156151.

7 W. Cai, H. Li, M. Li, M. Wang, H. Wang, J. Chen and Z. Zang, *J. Phys. D: Appl. Phys.*, 2021, **54**, 293002.

8 A. Christou, F. Liu and R. Dahiya, *Microsyst. Nanoeng.*, 2021, **7**, 82.

9 J. Nemirovsky and Y. Sagi, *Phys. Rev. Res.*, 2021, **3**, 013113.

10 N. Gack, G. Iankevich, C. Benel, R. Kruk, D. Wang, H. Hahn and T. Reisinger, *Nanomaterials*, 2020, **10**, 2192.

11 C. Outeiral, M. Strahm, J. Shi, G. M. Morris, S. C. Benjamin and C. M. Deane, *WIREs Comput. Mol. Sci.*, 2021, **11**, e1481.

12 F. Biedermann and H.-J. Schneider, *Chem. Rev.*, 2016, **116**, 5216–5300.

13 F. Zheng, X. Gao and A. Eisfeld, *Phys. Rev. Lett.*, 2019, **123**, 163202.

14 T. Nesse, I. Simonsen and B. Holst, *Phys. Rev. Applied*, 2019, **11**, 024009.

15 Boström, M., Esteso, V., Fiedler, J., Brevik, I., Buhmann, S. Y., Persson, C., Carretero-Palacios, S., Parsons, D. F. and Corkery, R. W., *A&A*, 2021, **650**, A54.

16 *Intermolecular and Surface Forces (Third Edition)*, ed. J. N. Israelachvili, Academic Press, San Diego, Third Edit edn, 2011.

17 P. Barcellona, R. Bennett and S. Y. Buhmann, *J. Phys. Comm.*, 2018, **2**, 035027.

18 B. Guillot, *J. Mol. Liq.*, 2002, **101**, 219 – 260.

19 H. B. G. Casimir, *K. Ned. Akad. Wet.*, 1948, **51**, 793.

20 H. B. G. Casimir and D. Polder, *Phys. Rev.*, 1948, **73**, 360–372.

21 I. E. Dzyaloshinskii, E. M. Lifshitz and L. P. Pitaevskii, *Adv. Phys.*, 1961, **10**, 165–209.

22 V. Esteso, S. Carretero-Palacios, L. G. MacDowell, J. Fiedler, D. F. Parsons, F. Spallek, H. Míguez, C. Persson, S. Y. Buhmann, I. Brevik and M. Boström, *Phys. Chem. Chem. Phys.*, 2020, **22**, 11362–11373.

23 M. Chern, J. C. Kays, S. Bhuckory and A. M. Dennis, *Methods Appl. Fluoresc.*, 2019, **7**, 012005.

24 H. Watzinger, J. Kukučka, L. Vukušić, F. Gao, T. Wang, F. Schäffler, J.-J. Zhang and G. Katsaros, *Nat. Commun.*, 2018, **9**, 3902.

25 J. P. Toennies and A. F. Vilesov, *Angew. Chem. Int. Ed.*, 2004, **43**, 2622–2648.

26 M. Dvorak, M. Müller, T. Knoblauch, O. Bünermann, A. Rydlo, S. Minniberger, W. Harbich and F. Stienkemeier, *J. Chem. Phys.*, 2012, **137**, 164301.

27 J. Farges, M. de Feraudy, B. Raoult and G. Torchet, *Surf. Sci.*, 1981, **106**, 95–100.

28 M. Hartmann, R. E. Miller, J. P. Toennies and A. Vilesov, *Phys. Rev. Lett.*, 1995, **75**, 1566–1569.

29 J. Harms, M. Hartmann, J. P. Toennies, A. F. Vilesov and B. Sartakov, *J. Mol. Spectrosc.*, 1997, **185**, 204–206.

30 G. B. Piland and C. J. Bardeen, *J. Phys. Chem. Lett.*, 2015, **6**, 1841–1846.

31 E. Garoni, J. Zirzlmeier, B. S. Basel, C. Hetzer, K. Kamada, D. M. Guldi and R. R. Tykwinski, *J. Amer. Chem. Soc.*, 2017, **139**, 14017–14020.

32 A. Rao and R. H. Friend, *Nat. Rev. Mat.*, 2017, **2**, 17063.

33 M. Müller, S. Izadnia, S. M. Vlaming, A. Eisfeld, A. LaForge and F. Stienkemeier, *Phys. Rev. B*, 2015, **92**, 121408.

34 O. Stauffert, S. Izadnia, F. Stienkemeier and M. Walter, *J. Chem. Phys.*, 2019, **150**, 244703.

35 M. Bohlen, R. Michiels, M. Michelbach, S. Ferchane, M. Walter, A. Eisfeld and F. Stienkemeier, *J. Chem. Phys.*, 2022, **156**, 034305.

36 E. Le Moal, M. Müller, O. Bauer and M. Sokolowski, *Phys. Rev. B*, 2010, **82**, 045301.

37 M. Müller, A. Paulheim, A. Eisfeld and M. Sokolowski, *J. Chem. Phys.*, 2013, **139**, 044302.

38 R. Hoffmann-Vogel, *Rep. Prog. Phys.*, 2017, **81**, 016501.

39 D. P. Goronzy, M. Ebrahimi, F. Rosei, Arramel, Y. Fang, S. De Feyter, S. L. Tait, C. Wang, P. H. Beton, A. T. S. Wee, P. S. Weiss and D. F. Perepichka, *ACS Nano*, 2018, **12**, 7445.

40 Y. Zhang, Y. Luo, Y. Zhang, Y.-J. Yu, Y.-M. Kuang, L. Zhang, Q.-S. Meng, Y. Luo, J.-L. Yang, Z.-C. Dong and J. G. Hou, *Nature*, 2016, **531**, 623.

41 B. Yang, G. Chen, A. Ghafoor, Y. Zhang, Y. Zhang, Y. Zhang, Y. Luo, J. Yang, V. Sandoghdar, J. Aizpurua, Z. Dong and J. G. Hou, *Nat. Phot.*, 2020, **14**, 693.

42 X. Gao and A. Eisfeld, *J. Phys. Chem. Lett.*, 2018, **9**, 6003–6010.

43 Y. Luo, G. Chen, Y. Zhang, L. Zhang, Y. Yu, F. Kong, X. Tian, Y. Zhang, C. Shan, Y. Luo, J. Yang, V. Sandoghdar, Z. Dong and J. G. Hou, *Phys. Rev. Lett.*, 2019, **122**, 233901.

44 J. Doležal, S. Canola, P. Hapala, R. C. de Campos Ferreira, P. Merino and M. Švec, *ACS Nano*, 2022, **16**, 1082–1088.

45 A. Eisfeld, C. Marquardt, A. Paulheim and M. Sokolowski, *Phys. Rev. Lett.*, 2017, **119**, 097402.

46 *Diamond-Based Materials for Biomedical Applications*, ed. R. Narayan, Woodhead Publishing, 2013.

47 Q. Xu and X. Zhao, *J. Mater. Chem.*, 2012, **22**, 16416–16421.

48 B. S. Miller, L. Bezinge, H. D. Gliddon, D. Huang, G. Dold, E. R. Gray, J. Heaney, P. J. Dobson, E. Nastouli, J. J. L. Morton and R. A. McKendry, *Nature*, 2020, **587**, 588–593.

49 D. P. Bottaro, J. S. Rubin, D. L. Faletto, A. M.-L. Chan, T. E. Kmiecik, G. F. V. Woude and S. A. Aaronson, *Science*, 1991, **251**, 802–804.

50 K. S. Novoselov, A. K. Geim, S. V. Morozov, D. Jiang, M. I. Katsnelson, I. V. Grigorieva, S. V. Dubonos and A. A. Firsov, *Nature*, 2005, **438**, 197–200.

51 Y. Zhang, Y.-W. Tan, H. L. Stormer and P. Kim, *Nature*, 2005,

438, 201–204.

52 C. R. Dean, A. F. Young, I. Meric, C. Lee, L. Wang, S. Sorgenfrei, K. Watanabe, T. Taniguchi, P. Kim, K. L. Shepard and J. Hone, *Nat. Nanotechnol.*, 2010, **5**, 722–726.

53 T. Taniguchi and K. Watanabe, *J. Cryst. Growth*, 2007, **303**, 525–529.

54 R. T. Weitz and A. Yacoby, *Nat. Nanotechnol.*, 2010, **5**, 699–700.

55 L. Renn, L. S. Walter, K. Watanabe, T. Taniguchi and R. T. Weitz, *Adv. Mater. Int.*, 2022, **9**, 2101701.

56 Y. J. Chung, K. A. Villegas Rosales, K. W. Baldwin, P. T. Madathil, K. W. West, M. Shayegan and L. N. Pfeiffer, *Nat. Mater.*, 2021, **20**, 632–637.

57 F. R. Geisenhof, F. Winterer, S. Wakolbinger, T. D. Gokus, Y. C. Durmaz, D. Priesack, J. Lenz, F. Keilmann, K. Watanabe, T. Taniguchi, R. Guerrero-Avilés, M. Pelc, A. Ayuela and R. T. Weitz, *ACS Appl. Nano Mater.*, 2019, **2**, 6067–6075.

58 R. Guerrero-Avilés, M. Pelc, F. Geisenhof, T. Weitz and A. Ayuela, *Relative Stability of Bernal and Rhombohedral Stackings in Trilayer Graphene under Distortions*, 2021, https://arxiv.org/abs/2110.06590.

59 N. Mounet, M. Gibertini, P. Schwaller, D. Campi, A. Merkys, A. Marrazzo, T. Sohier, I. E. Castelli, A. Cepellotti, G. Pizzi and N. Marzari, *Nat. Nanotechnol.*, 2018, **13**, 246–252.

60 D. G. Purdie, N. M. Pugno, T. Taniguchi, K. Watanabe, A. C. Ferrari and A. Lombardo, *Nat. Commun.*, 2018, **9**, 5387.

61 K. S. Novoselov, A. Mishchenko, A. Carvalho and A. H. C. Neto, *Science*, 2016, **353**, aac9439.

62 S. Wakolbinger, F. R. Geisenhof, F. Winterer, S. Palmer, J. G. Crimmann, K. Watanabe, T. Taniguchi, F. Trixler and R. T. Weitz, *2D Mater.*, 2020, **7**, 035002.

63 C. R. Dean, L. Wang, P. Maher, C. Forsythe, F. Ghahari, Y. Gao, J. Katoch, M. Ishigami, P. Moon, M. Koshino, T. Taniguchi, K. Watanabe, K. L. Shepard, J. Hone and P. Kim, *Nature*, 2013, **497**, 598–602.

64 J. I. A. Li, T. Taniguchi, K. Watanabe, J. Hone and C. R. Dean, *Nat. Phys.*, 2017, **13**, 751–755.

65 J. O. Island, X. Cui, C. Lewandowski, J. Y. Khoo, E. M. Spanton, H. Zhou, D. Rhodes, J. C. Hone, T. Taniguchi, K. Watanabe, L. S. Levitov, M. P. Zaletel and A. F. Young, *Nature*, 2019, **571**, 85–89.

66 A. M. Seiler, F. R. Geisenhof, F. Winterer, K. Watanabe, T. Taniguchi, T. Xu, F. Zhang and R. T. Weitz, *Quantum cascade of new correlated phases in trigonally warped bilayer graphene*, 2021, https://arxiv.org/abs/2111.06413.

67 F. R. Geisenhof, F. Winterer, A. M. Seiler, J. Lenz, T. Xu, F. Zhang and R. T. Weitz, *Nature*, 2021, **598**, 53–58.

68 Y. Cao, V. Fatemi, A. Demir, S. Fang, S. L. Tomarken, J. Y. Luo, J. D. Sanchez-Yamagishi, K. Watanabe, T. Taniguchi, E. Kaxiras, R. C. Ashoori and P. Jarillo-Herrero, *Nature*, 2018, **556**, 80–84.

69 Y. Cao, V. Fatemi, S. Fang, K. Watanabe, T. Taniguchi, E. Kaxiras and P. Jarillo-Herrero, *Nature*, 2018, **556**, 43–50.

70 M. Kasha, *Radiat. Res.*, 1963, **20**, 55–70.

71 S. Das, F. Herrmann-Westendorf, F. H. Schacher, E. Tauscher, U. Ritter, B. Dietzek and M. Presselt, *ACS Appl. Mater. Interfaces*, 2016, **8**, 21512–21.

72 M. L. Hupfer, D. Blaschke, H. Schmidt and M. Presselt, *Langmuir*, 2021, **37**, 13255–13264.

73 J. Bellessa, C. Symonds, K. Vynck, A. Lemaitre, A. Brioude, L. Beaur, J. C. Plenet, P. Viste, D. Felbacq, E. Cambril and P. Valvin, *Phys. Rev. B*, 2009, **80**, 033303.

74 J. George, T. Chervy, A. Shalabney, E. Devaux, H. Hiura, C. Genet and T. W. Ebbesen, *Phys. Rev. Lett.*, 2016, **117**, 153601.

75 S. Dey, C. Fan, K. V. Gothelf, J. Li, C. Lin, L. Liu, N. Liu, M. A. D. Nijenhuis, B. Saccà, F. C. Simmel, H. Yan and P. Zhan, *Nat. Rev. Meth. Prim.*, 2021, **1**, 13.

76 F. Hong, F. Zhang, Y. Liu and H. Yan, *Chem. Rev.*, 2017, **117**, 12584–12640.

77 W. Liu, H. Duan, D. Zhang, X. Zhang, Q. Luo, T. Xie, H. Yan, L. Peng, Y. Hu, L. Liang, G. Zhao, Z. Xie and J. Hu, *Appl. Bionics. Biomech.*, 2021, **2021**, 9112407–9112407.

78 K. Ariga, *Langmuir*, 2020, **36**, 7158–7180.

79 K. Ariga, Y. Yamauchi, T. Mori and J. P. Hill, *Adv. Mater.*, 2013, **25**, 6477–6512.

80 I. Langmuir, *J. Am. Chem. Soc.*, 1917, **39**, 1848–1906.

81 I. Langmuir and K. B. Blodgett, *Kolloid-Zeitschrift*, 1935, **73**, 257–263.

82 Y. Yonamine, K. Cervantes-Salguero, K. Minami, I. Kawamata, W. Nakanishi, J. P. Hill, S. Murata and K. Ariga, *Phys. Chem. Chem. Phys.*, 2016, **18**, 12576–12581.

83 D. Bialas, C. W. Zhong, F. Wurthner and F. C. Spano, *J. Phys. Chem. C*, 2019, **123**, 18654–18664.

84 N. J. Hestand and F. C. Spano, *Chem. Rev.*, 2018, **118**, 7069–7163.

85 B. Heyne, *Photochem. Photobiol. Sci.*, 2016, **15**, 1103–1114.

86 E. E. Jelley, *Nature*, 1937, **139**, 631–631.

87 G. Scheibe, *Angew. Chem.*, 1937, **50**, 212–219.

88 F. C. Spano, *Acc. Chem. Res.*, 2010, **43**, 429–439.

89 F. Würthner, *Acc. Chem. Res.*, 2016, **49**, 868–876.

90 F. Würthner, S. Yao, T. Debaerdemaeker and R. Wortmann, *J. Am. Chem. Soc.*, 2002, **124**, 9431–9447.

91 C. W. Zhong, D. Bialas and F. C. Spano, *J. Phys. Chem. C*, 2020, **124**, 2146–2159.

92 M. L. Hupfer, S. Ghosh, Y. Wang, T. Opsomer, W. Dehaen and M. Presselt, *Adv. Mater. Interfaces*, 2021, **9**, 2101490.

93 S. Das and M. Presselt, *J. Mater. Chem. C*, 2019, **7**, 6194–6216.

94 G. Herzberg and E. Teller, *Z. Phys. Chem. (Frankfurt am Main)*, 1933, **B 21**, 410.

95 F. Negri, G. Orlandi and F. Zerbetto, *J. Chem. Phys.*, 1992, **97**, 6496–6503.

96 G. Orlandi and W. Siebrand, *J. Chem. Phys.*, 1973, **58**, 4513–4523.

97 N. J. Hestand, H. Yamagata, B. L. Xu, D. Z. Sun, Y. Zhong, A. R. Harutyunyan, G. G. Chen, H. L. Dai, Y. Rao and F. C. Spano, *J. Phys. Chem. C*, 2015, **119**, 22137–22147.

98 O. Ostroverkhova, S. Shcherbyna, D. G. Cooke, R. F. Egerton, F. A. Hegmann, R. R. Tykwinski, S. R. Parkin and J. E. Anthony, *J. Appl. Phys.*, 2005, **98**, 033701.

99 J. A. Reinspach, Y. Diao, G. Giri, T. Sachse, K. England, Y. Zhou, C. Tassone, B. J. Worfolk, M. Presselt, M. F. Toney, S. Mannsfeld and Z. Bao, *ACS Appl. Mater. Interfaces*, 2016, **8**, 1742–1751.

100 B. Munkhbat, A. Canales, B. Küçüköz, D. G. Baranov and T. O. Shegai, *Nature*, 2021, **597**, 214–219.

101 S. H. Kim, K. Hong, W. Xie, K. H. Lee, S. Zhang, T. P. Lodge and C. D. Frisbie, *Adv. Mater.*, 2013, **25**, 1822–1846.

102 M. Kettner, I. Vladimirov, A. J. Strudwick, M. G. Schwab and R. T. Weitz, *J. Appl. Phys.*, 2015, **118**, 025501.

103 J. Lenz, A. M. Seiler, F. R. Geisenhof, F. Winterer, K. Watanabe, T. Taniguchi and R. T. Weitz, *Nano Lett.*, 2021, **21**, 4430–4436.

104 Y. van de Burgt, E. Lubberman, E. J. Fuller, S. T. Keene, G. C. Faria, S. Agarwal, M. J. Marinella, A. Alec Talin and A. Salleo, *Nat. Mater.*, 2017, **16**, 414–418.

105 C. Eckel, J. Lenz, A. Melianas, A. Salleo and R. T. Weitz, *Nano Lett.*, 2022, **22**, 973–978.

106 A. Shirinskaya, G. Horowitz, J. Rivnay, G. G. Malliaras and Y. Bonnassieux, *Biosensors*, 2018, **8**, 103.

107 J. F. Geisz, R. M. France, K. L. Schulte, M. A. Steiner, A. G. Norman, H. L. Guthrey, M. R. Young, T. Song and T. Moriarty, *Nat. Energy*, 2020, **5**, 326–335.

108 C. A. Nelson, N. R. Monahan and X.-Y. Zhu, *Energy Environ. Sci.*, 2013, **6**, 3508–3519.

109 J.-F. Guillemoles, T. Kirchartz, D. Cahen and U. Rau, *Nat. Photonics*, 2019, **13**, 501–505.

110 A. Deinega and S. John, *J. Appl. Phys.*, 2012, **112**, 074327.

111 D. M. Callahan, J. N. Munday and H. A. Atwater, *Nano Lett.*, 2012, **12**, 214–218.

112 Z. Yu, A. Raman and S. Fan, *Proc. Nat. Acad. Sci.*, 2010, **107**, 17491–17496.

113 S. Buddhiraju and S. Fan, *Phys. Rev. B*, 2017, **96**, 035304.

114 J. Wallentin, N. Anttu, D. Asoli, M. Huffman, I. Åberg, M. H. Magnusson, G. Siefer, P. Fuss-Kailuweit, F. Dimroth, B. Witzigmann, H. Q. Xu, L. Samuelson, K. Deppert and M. T. Borgström, *Science*, 2013, **339**, 1057–1060.

115 R. Kapadia, Z. Fan, K. Takei and A. Javey, *Nano Energy*, 2012, **1**, 132–144.

116 S.-F. Leung, M. Yu, Q. Lin, K. Kwon, K.-L. Ching, L. Gu, K. Yu and Z. Fan, *Nano Lett.*, 2012, **12**, 3682–3689.

117 A. Peter Amalathas and M. M. Alkaisi, *Mater. Sci. Semicond. Proces.*, 2017, **57**, 54–58.

118 M. A. Green and S. Pillai, *Nat. Photonics*, 2012, **6**, 130–132.

119 P. G. Jamkhande, N. W. Ghule, A. H. Bamer and M. G. Kalaskar, *J. Drug Deliv. Sci. Technol.*, 2019, **53**, 101174.

120 H. A. Atwater and A. Polman, *Nat. Mat.*, 2010, **9**, 205–213.

121 V. Giannini, Y. Zhang, M. Forcales and J. G. Rivas, *Opt. Express*, 2008, **16**, 19674–19685.

122 D. Derkacs, S. H. Lim, P. Matheu, W. Mar and E. T. Yu, *Appl. Phys. Lett.*, 2006, **89**, 093103.

123 H. R. Stuart and D. G. Hall, *Appl. Phys. Lett.*, 1996, **69**, 2327–2329.

124 S. Pillai, K. R. Catchpole, T. Trupke and M. A. Green, *J. Appl. Phys.*, 2007, **101**, 093105.

125 C. E. R. Disney, S. Pillai and M. A. Green, *Sci. Rep.*, 2017, **7**, 12826.

126 S. H. Lim, W. Mar, P. Matheu, D. Derkacs and E. T. Yu, *J. Appl. Phys.*, 2007, **101**, 104309.

127 F. J. Beck, A. Polman and K. R. Catchpole, *J. Appl. Phys.*, 2009, **105**, 114310.

128 N. P. Hylton, X. F. Li, V. Giannini, K.-H. Lee, N. J. Ekins-Daukes, J. Loo, D. Vercruysse, P. Van Dorpe, H. Sodabanlu, M. Sugiyama and S. A. Maier, *Sci. Rep.*, 2013, **3**, 1–6.

129 Y. Zhang, B. Cai and B. Jia, *Nanomaterials*, 2016, **6**, 1–10.

130 C. Bohren and D. R. Huffman, *Absorption and Scattering of Light by Small Particles*, John Wiley & Sons, Ltd, 1998.

131 C. Hägglund and S. P. Apell, *J. Phys. Chem. Lett.*, 2012, **3**, 1275–1285.

132 H. Shen, P. Bienstman and B. Maes, *J. App. Phys.*, 2009, **106**, 073109.

133 A. Augusto, E. Looney, C. del Cañizo, S. G. Bowden and T. Buonassisi, *Energy Procedia*, 2017, **124**, 706–711.

134 V. E. Ferry, L. A. Sweatlock, D. Pacifici and H. A. Atwater, *Nano Lett.*, 2008, **8**, 4391–4397.

135 I. R. Hooper and J. R. Sambles, *Phys. Rev. B*, 2002, **65**, 165432.

136 H. Huang, L. Lu, J. Wang, J. Yang, S.-F. Leung, Y. Wang, D. Chen, X. Chen, G. Shen, D. Li and Z. Fan, *Energy Environ. Sci.*, 2013, **6**, 2965–2971.

137 T. A. Kelf, Y. Sugawara, R. M. Cole, J. J. Baumberg, M. E. Abdelsalam, S. Cintra, S. Mahajan, A. E. Russell and P. N. Bartlett, *Phys. Rev. B*, 2006, **74**, 245415.

138 J. Zhu, Z. Yu, G. F. Burkhard, C.-M. Hsu, S. T. Connor, Y. Xu, Q. Wang, M. McGehee, S. Fan and Y. Cui, *Nano Lett.*, 2009, **9**, 279–282.

139 C.-M. Hsu, C. Battaglia, C. Pahud, Z. Ruan, F.-J. Haug, S. Fan, C. Ballif and Y. Cui, *Adv. Energy Mater.*, 2012, **2**, 628–633.

140 R. Bogue, *Sens. Rev.*, 2016, **36**, 225–230.

141 C. Li, P. Zhou and D. W. Zhang, *J. Semicond.*, 2017, **38**, 031005.

142 R. Liu and L. Wang, *J. Appl. Phys.*, 2020, **128**, 145105.

143 W. C. Crone, in *A Brief Introduction to MEMS and NEMS*, ed. W. N. Sharpe, Springer US, Boston, MA, 2008, pp. 203–228.

144 Anon., *Sens. Rev.*, 2011, **35**,.

145 R. Bogue, *Sens. Rev.*, 2016, **36**, 1–6.

146 A. Hajarian, M. M. Zand and N. Zolfaghari, *Int. J. Appl. Mech.*, 2019, **11**, 1950085.

147 Y. T. Beni, I. Karimipöur and M. Abadyan, *J. Mech. Sci. Technol.*, 2014, **28**, 3749–3757.

148 V. B. Svetovoy and G. Palasantzas, *Mod. Phys. Lett. A*, 2020, **35**, 2040014.

149 S. Akhundzada, X. Yang, J. Fiedler, E. Käkel, B. Al-Qargholi,

Physical Chemistry Chemical Physics Accepted Manuscript

S. Buhmann, A. Ehresmann and H. Hillmer, *Microsyst Technol*, 2022, **28**, 2139–2148.

150 M. Trushin and A. H. Castro Neto, *Phys. Rev. Lett.*, 2021, **127**, 156101.

151 T. Gong, M. R. Corrado, A. R. Mahbub, C. Shelden and J. N. Munday, *Nanophotonics*, 2021, **10**, 523–536.

152 H. B. Chan, V. A. Aksyuk, R. N. Kleiman, D. J. Bishop and F. Capasso, *Science*, 2001, **291**, 1941–1944.

153 D. S. Dovzhenko, S. V. Ryabchuk, Y. P. Rakovich and I. R. Nabiev, *Nanoscale*, 2018, **10**, 3589–3605.

154 M. Hertzog, M. Wang, J. Mony and K. Börjesson, *Chem. Soc. Rev.*, 2019, **48**, 937–961.

155 F. J. Garcia-Vidal, C. Ciuti and T. W. Ebbesen, *Science*, 2021, **373**, eabd0336.

156 Y. Yamamoto and A. Imamoglu, *Mesoscoptic Quantum Optics*, Wiley-Interscience, Hoboken, NJ, USA, 1999.

157 A. V. Zasedatelev, A. V. Baranikov, D. Urbonas, F. Scafirimuto, U. Scherf, T. Stöferle, R. F. Mahrt and P. G. Lagoudakis, *Nat. Photonics*, 2019, **13**, 378–383.

158 A. Graf, M. Held, Y. Zakharko, L. Tropf, M. C. Gather and J. Zaumseil, *Nat. Mater.*, 2017, **16**, 911–917.

159 M. Held, A. Graf, Y. Zakharko, P. Chao, L. Tropf, M. C. Gather and J. Zaumseil, *Adv. Opt. Mater.*, 2018, **6**, 1700962.

160 Y. Yu, S. Mallick, M. Wang and K. Börjesson, *Nat. Commun.*, 2021, **12**, 3255.

161 A. Thomas, E. Devaux, K. Nagarajan, G. Rogez, M. Seidel, F. Richard, C. Genet, M. Drillon and T. W. Ebbesen, *Nano Lett.*, 2021, **21**, 4365–4370.

162 F. Appugliese, J. Enkner, G. L. Paravicini-Bagliani, M. Beck, C. Reichl, W. Wegscheider, G. Scalari, C. Ciuti and J. Faist, *Science*, 2022, **375**, 1030–1034.

163 S. Xiao, X. Zhu, B.-H. Li and N. A. Mortensen, *Front. Phys.*, 2016, **11**, 117801.

164 L. Xiong, Y. Li, M. Jung, C. Forsythe, S. Zhang, A. S. McLeod, Y. Dong, S. Liu, F. L. Ruta, C. Li, K. Watanabe, T. Taniguchi, M. M. Fogler, J. H. Edgar, G. Shvets, C. R. Dean and D. N. Basov, *Sci. Adv.*, 2021, **7**, eabe8087.

165 E. Orgiu, J. George, J. A. Hutchison, E. Devaux, J. F. Dayen, B. Doudin, F. Stellacci, C. Genet, J. Schachenmayer, C. Genes, G. Pupillo, P. Samorì and T. W. Ebbesen, *Nat. Mater.*, 2015, **14**, 1123–1129.

166 K. Nagarajan, J. George, A. Thomas, E. Devaux, T. Chervy, S. Azzini, K. Joseph, A. Jouaiti, M. W. Hosseini, A. Kumar, C. Genet, N. Bartolo, C. Ciuti and T. W. Ebbesen, *ACS Nano*, 2020, **14**, 10219–10225.

167 P. Bhatt, K. Kaur and J. George, *ACS Nano*, 2021, **15**, 13616–13622.

168 D. Hagenmüller, J. Schachenmayer, S. Schütz, C. Genes and G. Pupillo, *Phys. Rev. Lett.*, 2017, **119**, 223601.

169 R. Pandya, A. Ashoka, K. Georgiou, J. Sung, R. Jayaprakash, S. Renken, L. Gai, Z. Shen, A. Rao and A. J. Musser, *Adv. Sci.*, 2022, **n/a**, 2105569.

170 J. D. B. Van Schenck, W. T. Goldthwaite, R. Puro, J. E. Anthony and O. Ostroverkhova, *J. Phys. Chem. C*, 2021, **125**, 27381–27393.

171 C. Gonzalez-Ballestero, J. Feist, E. Gonzalo Badía, E. Moreno and F. J. Garcia-Vidal, *Phys. Rev. Lett.*, 2016, **117**, 156402.

172 C.-Y. Cheng, R. Dhanker, C. L. Gray, S. Mukhopadhyay, E. R. Kennehan, J. B. Asbury, A. Sokolov and N. C. Giebink, *Phys. Rev. Lett.*, 2018, **120**, 017402.

173 C. Möhl, A. Graf, F. J. Berger, J. Lüttgens, Y. Zakharko, V. Lumsargis, M. C. Gather and J. Zaumseil, *ACS Photonics*, 2018, **5**, 2074–2080.

174 E. Orgiu, J. George, J. A. Hutchison, E. Devaux, J. F. Dayen, B. Doudin, F. Stellacci, C. Genet, J. Schachenmayer, C. Genes, G. Pupillo, P. Samorì and T. W. Ebbesen, *Nat. Mater.*, 2015, **14**, 1123–1129.

175 https://creativecommons.org/licenses/by/4.0/.

176 J. Galego, F. J. Garcia-Vidal and J. Feist, *Nat. Commun.*, 2016, **7**, 13841.

177 J. A. Hutchison, T. Schwartz, C. Genet, E. Devaux and T. W. Ebbesen, *Angew. Chem., Int. Ed.*, 2012, **51**, 1592–1596.

178 K. Nagarajan, A. Thomas and T. W. Ebbesen, *J. Am. Chem. Soc.*, 2021, **143**, 16877–16889.

179 J. Flick, M. Ruggenthaler, H. Appel and A. Rubio, *Proc. Natl. Acad. Sci.*, 2017, **114**, 3026–3034.

180 D. Sidler, M. Ruggenthaler, H. Appel and A. Rubio, *J. Phys. Chem. Lett.*, 2020, **11**, 7525–7530.

181 T. S. Haugland, C. Schäfer, E. Ronca, A. Rubio and H. Koch, *J. Chem. Phys.*, 2021, **154**, 094113.

182 D. M. Coles, N. Somaschi, P. Michetti, C. Clark, P. G. Lagoudakis, P. G. Savvidis and D. G. Lidzey, *Nat. Mat.*, 2014, **13**, 712–719.

183 H. Hübener, U. De Giovannini, C. Schäfer, J. Andberger, M. Ruggenthaler, J. Faist and A. Rubio, *Nat. Mat.*, 2021, **20**, 438–442.

184 A. Thomas, L. Lethuillier-Karl, K. Nagarajan, R. M. A. Vergauwe, J. George, T. Chervy, A. Shalabney, E. Devaux, C. Genet, J. Moran and T. W. Ebbesen, *Science*, 2019, **363**, 615–619.

185 B. Xiang, R. F. Ribeiro, M. Du, L. Chen, Z. Yang, J. Wang, J. Yuen-Zhou and W. Xiong, *Science*, 2020, **368**, 665–667.

186 B. S. Simpkins, A. D. Dunkelberger and J. C. Owrutsky, *J. Phys. Chem. C*, 2021, **125**, 19081–19087.

187 Y.-C. Chen, B. Song, A. J. Leggett, P. Ao and X. Zhu, *Phys. Rev. Lett.*, 2019, **122**, 257402.

188 A. Canales, D. G. Baranov, T. J. Antosiewicz and T. Shegai, *J. Chem. Phys.*, 2021, **154**, 024701.

189 R. Pandya, R. Y. S. Chen, Q. Gu, J. Sung, C. Schnedermann, O. S. Ojambati, R. Chikkaraddy, J. Gorman, G. Jacucci, O. D. Onelli, T. Willhammar, D. N. Johnstone, S. M. Collins, P. A. Midgley, F. Auras, T. Baikie, R. Jayaprakash, F. Mathevet, R. Soucek, M. Du, A. M. Alvertis, A. Ashoka, S. Vignolini, D. G. Lidzey, J. J. Baumberg, R. H. Friend, T. Barisien, L. Legrand, A. W. Chin, J. Yuen-Zhou, S. K. Saikin, P. Kukura, A. J. Musser and A. Rao, *Nat. Commun.*, 2021, **12**, 6519.

190 D. Tabor and R. H. S. Winterton, *Proc. R. Soc. A: Math. Phys. Eng. Sci.*, 1969, **312**, 435–450.

191 G. D. Degen, P. Delparastan, B. D. B. Tiu and P. B. Messersmith, *ACS Appl. Mater. Interfaces*, 2022, **14**, 6212–6220.

192 M. A. Gebbie, A. M. Smith, H. A. Dobbs, A. A. Lee, G. G. Warr, X. Banquy, M. Valtiner, M. W. Rutland, J. N. Israelachvili, S. Perkin and R. Atkin, *Chem. Commun.*, 2017, **53**, 1214–1224.

193 S. Perkin, L. Chai, N. Kampf, U. Raviv, W. Briscoe, I. Dunlop, S. Titmuss, M. Seo, E. Kumacheva and J. Klein, *Langmuir*, 2006, **22**, 6142–6152.

194 F. J. Giessibl, *Rev. Mod. Phys.*, 2003, **75**, 949–983.

195 G. Binnig, C. F. Quate and C. Gerber, *Phys. Rev. Lett.*, 1986, **56**, 930–933.

196 F. J. Giessibl, *Rev. Mod. Phys.*, 2003, **75**, 949–983.

197 H. Edwards, L. Taylor, W. Duncan and A. J. Melmed, *J. Appl. Phys.*, 1997, **82**, 980–984.

198 E. Meyer, H. Hug and R. Bennewitz, *Scanning Probe Microscopy: The Lab on a Tip*, Springer Berlin Heidelberg, 2003.

199 N. Ishida and V. S. J. Craig, *KONA Powd. Part. J.*, 2019, **36**, 187–200.

200 P. Loskill, J. Puthoff, M. Wilkinson, K. Mecke, K. Jacobs and K. Autumn, *J. R. Soc. Interface*, 2013, **10**, 20120587.

201 R. Seemann, S. Herminghaus and K. Jacobs, *Phys. Rev. Lett.*, 2001, **86**, 5534–5537.

202 R. Seemann, S. Herminghaus and K. Jacobs, *J. Phys.: Condens. Matter*, 2001, **13**, 4925–4938.

203 A. Vrij, *Discuss. Faraday Soc.*, 1966, **42**, 23–33.

204 L. Gross, F. Mohn, N. Moll, P. Liljeroth and G. Meyer, *Science*, 2009, **325**, 1110–1114.

205 J. L. Hutter and J. Bechhoefer, *J. Appl. Phys.*, 1993, **73**, 4123–4129.

206 F. Ohnesorge and G. Binnig, *Science*, 1993, **260**, 1451–1456.

207 J. N. Munday, F. Capasso and V. A. Parsegian, *Nature*, 2009, **457**, 170–173.

208 F. A. Burger, R. W. Corkery, S. Y. Buhmann and J. Fiedler, *J. Phys. Chem. C*, 2020, **124**, 24179–24186.

209 L. D. Landau and I. M. Lifshitz, *Theory of Elasticity*, Elsevier, Amsterdam, 1986.

210 T. Nihira and T. Iwata, *Phys. Rev. B*, 2003, **68**, 134305.

211 D. L. Nika and A. A. Balandin, *Rep. Prog. Phys.*, 2017, **80**, 036502.

212 B. Amorim and F. Guinea, *Phys. Rev. B*, 2013, **88**, 115418.

213 A. Al Taleb, H. K. Yu, G. Anemone, D. Farías and A. M. Wodtke, *Carbon*, 2015, **95**, 731–737.

214 C. Büchner, S. D. Eder, T. Nesse, D. Kuhness, P. Schlexer, G. Pacchioni, J. R. Manson, M. Heyde, B. Holst and H.-J. Freund, *Phys. Rev. Lett.*, 2018, **120**, 226101.

215 M. Tømterud, S. D. Eder, C. Büchner, M. Heyde, H.-J. Freund, J. R. Manson and B. Holst, *Phys. Chem. Chem. Phys.*, 2022, Advance Article.

216 S. D. Eder, S. K. Hellner, S. Forti, J. M. Nordbotten, J. R. Manson, C. Coletti and B. Holst, *Phys. Rev. Lett.*, 2021, **127**, 266102.

217 I. Y. Sklyadneva, G. Benedek, E. V. Chulkov, P. M. Echenique, R. Heid, K.-P. Bohnen and J. P. Toennies, *Phys. Rev. Lett.*, 2011, **107**, 095502.

218 G. Benedek, M. Bernasconi, K.-P. Bohnen, D. Campi, E. V. Chulkov, P. M. Echenique, R. Heid, I. Y. Sklyadneva and J. P. Toennies, *Phys. Chem. Chem. Phys.*, 2014, **16**, 7159.

219 J. R. Manson, G. Benedek and S. Miret-Artés, *J. Phys. Chem. Lett.*, 2016, **7**, 1016–1021.

220 G. Benedek, S. Miret-Artés, J. P. Toennies and J. R. Manson, *J. Phys. Chem. Lett.*, 2017, **9**, 76–83.

221 G. Benedek, J. R. Manson and S. Miret-Artés, *Phys. Chem. Chem. Phys.*, 2021, **23**, 7575–7585.

222 A. Tamtögl, P. Kraus, N. Avidor, M. Bremholm, E. M. J. Hedegaard, B. B. Iversen, M. Bianchi, P. Hofmann, J. Ellis, W. Allison, G. Benedek and W. E. Ernst, *Phys. Rev. B*, 2017, **95**, 195401.

223 G. Benedek, S. Miret-Artés, J. R. Manson, A. Ruckhofer, W. E. Ernst and A. Tamtögl, *J. Phys. Chem. Lett.*, 2020, **11**, 1927–1933.

224 A. D. Cronin, J. Schmiedmayer and D. E. Pritchard, *Rev. Mod. Phys.*, 2009, **81**, 1051–1129.

225 K. Hornberger, S. Gerlich, P. Haslinger, S. Nimmrichter and M. Arndt, *Rev. Mod. Phys.*, 2012, **84**, 157–173.

226 J. H. Lee, L. Y. Kim, Y.-T. Kim, C. Y. Lee, W. Schöllkopf and B. S. Zhao, *Phys. Rev. Lett.*, 2019, **122**, 040401.

227 R. E. Grisenti, W. Schöllkopf, J. P. Toennies, G. C. Hegerfeldt and T. Köhler, *Phys. Rev. Lett.*, 1999, **83**, 1755.

228 J. D. Perreault and A. D. Cronin, *Phys. Rev. Lett.*, 2005, **95**, 133201.

229 C. Brand, M. Sclafani, C. Knobloch, Y. Lilach, T. Juffmann, J. Kotakoski, C. Mangler, A. Winter, A. Turchanin, J. Meyer, O. Cheshnovsky and M. Arndt, *Nat. Nanotech.*, 2015, **10**, 845–848.

230 J. L. Hemmerich, R. Bennett, T. Reisinger, S. Nimmrichter, J. Fiedler, H. Hahn, H. Gleiter and S. Y. Buhmann, *Phys. Rev. A*, 2016, **94**, 023621.

231 N. Gack, C. Reitz, J. L. Hemmerich, M. Könne, R. Bennett, J. Fiedler, H. Gleiter, S. Y. Buhmann, H. Hahn and T. Reisinger, *Phys. Rev. Lett.*, 2020, **125**, 050401.

232 S. Nowak, N. Stuhler, T. Pfau and J. Mlynek, *Phys. Rev. Lett.*, 1998, **81**, 5792–5795.

233 T. Reisinger, A. A. Patel, H. Reingruber, K. Fladischer, W. E. Ernst, G. Bracco, H. I. Smith and B. Holst, *Phys. Rev. A*, 2009, **79**, 053823.

234 T. Juffmann, S. Nimmrichter, M. Arndt, H. Gleiter and K. Hornberger, *Found. Phys.*, 2012, **42**, 98–110.

235 M. Könne, R. Bennett, T. Reisinger and S. Y. Buhmann, *Phys. Rev. A*, 2017, **96**, 013626.

236 T. Reisinger, P. M. Leufke, H. Gleiter and H. Hahn, *N. J. Phys.*, 2017, **19**, 033022.

237 T. Reisinger, G. Bracco and B. Holst, *N. J. Phys.*, 2011, **13**, 065016.

238 C. Brand, M. Debiossac, T. Susi, F. Aguillon, J. Kotakoski, P. Roncin and M. Arndt, *N. J. Phys.*, 2019, **21**, 033004.

239 M. Koch, S. Rehbein, G. Schmahl, T. Reisinger, G. Bracco, W. E. Ernst and B. Holst, *J. Microsc. (cover story)*, 2008, **229**,

1.

240 T. Reisinger, S. Eder, M. M. Greve, H. I. Smith and B. Holst, *Microelectron. Eng.*, 2010, **87**, 1011 – 1014.

241 N. F. Hartmann, M. Otten, I. Fedin, D. Talapin, M. Cygorek, P. Hawrylak, M. Korkusinski, S. Gray, A. Hartschuh and X. Ma, *Nat. Commun.*, 2019, **10**, 3253.

242 M. L. Hupfer, M. Kaufmann, F. Herrmann-Westendorf, T. Sachse, L. Roussille, K. H. Feller, D. Weiss, V. Deckert, R. Beckert, B. Dietzek and M. Presselt, *ACS Appl. Mater. Interfaces*, 2017, **9**, 44181–44191.

243 M. J. Jurow, C. Mayr, T. D. Schmidt, T. Lampe, P. I. Djurovich, W. Brütting and M. E. Thompson, *Nat. Mater.*, 2016, **15**, 85–91.

244 S. Y. Byeon, J. Kim, D. R. Lee, S. H. Han, S. R. Forrest and J. Y. Lee, *Adv. Optical Mater.*, 2018, **6**, 1701340.

245 M. Orrit, D. Möbius, U. Lehmann and H. Meyer, *J. Chem. Phys.*, 1986, **85**, 4966–4979.

246 M. Yoneyama, M. Sugi, M. Saito, K. Ikegami, S. Kuroda and S. Iizima, *Jap. J. Appl. Phys. Part 1*, 1986, **25**, 961–965.

247 H. Yong, N. Zotev, B. Stankus, J. M. Ruddock, D. Bellshaw, S. Boutet, T. J. Lane, M. Liang, S. Carbajo, J. S. Robinson, W. Du, N. Goff, Y. Chang, J. E. Koglin, M. D. J. Waters, T. I. Sølling, M. P. Minitti, A. Kirrander and P. M. Weber, *J. Phys. Chem. Lett.*, 2018, **9**, 6556–6562.

248 M. A. Lieb, J. M. Zavislan and L. Novotny, *J. Opt. Soc. Am. B*, 2004, **21**, 1210–1215.

249 E. Lifshitz, *JETP*, 1956, **2**, 73.

250 P. A. Maia Neto, A. Lambrecht and S. Reynaud, *Phys. Rev. A*, 2008, **78**, 012115.

251 S. J. Rahi, T. Emig, N. Graham, R. L. Jaffe and M. Kardar, *Phys. Rev. D*, 2009, **80**, 085021.

252 M. Krüger, G. Bimonte, T. Emig and M. Kardar, *Phys. Rev. B*, 2012, **86**, 115423.

253 O. Kenneth and I. Klich, *Phys. Rev. Lett.*, 2006, **97**, 160401.

254 S. J. Rahi, M. Kardar and T. Emig, *Phys. Rev. Lett.*, 2010, **105**, 070404.

255 W. Eckhardt, *Phys. Rev. A*, 1984, **29**, 1991.

256 V. S. Asadchy, M. S. Mirmoosa, A. Díaz-Rubio, S. Fan and S. A. Tretyakov, *Proc. IEEE*, 2020, **108**, 1684–1727.

257 S.-A. Biehs, R. Messina, P. S. Venkataram, A. W. Rodriguez, J. C. Cuevas and P. Ben-Abdallah, *Rev. Mod. Phys.*, 2021, **93**, 025009.

258 D. Gelbwaser-Klimovsky, N. Graham, M. Kardar and M. Krüger, *Equilibrium forces on non-reciprocal media*, arXiv:2205.13470.

259 D. Gelbwaser-Klimovsky, N. Graham, M. Kardar and M. Krüger, *Phys. Rev. Lett.*, 2021, **126**, 170401.

260 M. G. Silveirinha, S. A. H. Gangaraj, G. W. Hanson and M. Antezza, *Phys. Rev. A*, 2018, **97**, 022509.

261 J. A. Girón-Sedas, J. J. Kingsley-Smith and F. J. Rodríguez-Fortuño, *Phys. Rev. B*, 2019, **100**, 075419.

262 S. A. H. Gangaraj, M. G. Silveirinha, G. W. Hanson, M. Antezza and F. Monticone, *Phys. Rev. B*, 2018, **98**, 125146.

263 F. Lindel, G. W. Hanson, M. Antezza and S. Y. Buhmann, *Phys. Rev. B*, 2018, **98**, 144101.

264 S. A. Hassani Gangaraj, G. W. Hanson, M. Antezza and M. G. Silveirinha, *Phys. Rev. B*, 2018, **97**, 201108.

265 C. Khandekar, S. Buddhiraju, P. R. Wilkinson, J. K. Gimzewski, A. W. Rodriguez, C. Chase and S. Fan, *Phys. Rev. B*, 2021, **104**, 245433.

266 Y. Tsurimaki, X. Qian, S. Pajovic, S. Boriskina and G. Chen, *Casimir force among spheres made of Weyl semimetals breaking Lorentz reciprocity*, 2021.

267 M. B. Farias, A. A. Zyuzin and T. L. Schmidt, *Phys. Rev. B*, 2020, **101**, 235446.

268 Q.-D. Jiang and F. Wilczek, *Phys. Rev. B*, 2019, **99**, 125403.

269 B. V. Derjaguin and L. D. Landau, *Acta Physicochimica URSS*, 1941, **14**, 633–662.

270 E. J. W. Verwey and J. T. G. Overbeek, *Theory of the Stability of Lyophobic Colloids*, Elsevier, 1948, p. 205.

271 H. C. Hamaker, *Physica (Amsterdam)*, 1937, **4**, 1058–1072.

272 F. Hofmeister, *Archiv für experimentelle Pathologie und Pharmakologie*, 1888, **24**, 247–260.

273 S. S. A. Burgess, J. Geddes, K. K. E. Hawton, M. J. Taylor, E. Townsend, K. Jamison and G. Goodwin, *Cochrane Database Syst. Rev.*, 2001, 1–49.

274 T. A. Zimmers, J. Sheldon, D. A. Lubarsky, F. López-Muñoz, L. Waterman, R. Weisman and L. G. Koniaris, *PLoS Medicine*, 2007, **4**, e156.

275 R. Kjellander, *J. Phys. Con. Matt.*, 2009, **21**, 424101.

276 R. Kjellander, *J. Chem. Phys.*, 2018, **148**, 193701.

277 J. P. De Souza, K. Pivnic, M. Z. Bazant, M. Urbakh and A. A. Kornyshev, *J. Phys. Chem. B*, 2021, **2022**, 1242–1253.

278 D. J. Bonthuis and R. R. Netz, *J. Phys. Chem. B*, 2013, **117**, 11397–11413.

279 M. Galib, T. T. Duignan, Y. Misteli, M. D. Baer, G. K. Schenter, J. Hutter and C. J. Mundy, *J. Chem. Phys.*, 2017, **146**, 244501.

280 B. W. Ninham and V. Yaminsky, *Langmuir*, 1997, **13**, 2097–2108.

281 J. Mahanty and B. W. Ninham, *J. Chem. Phys.*, 1973, **59**, 6157–6162.

282 J. Mahanty and B. W. Ninham, *Dispersion Forces*, Academic Press, London, 1976.

283 J. Fiedler, P. Thiyam, A. Kurumbail, F. A. Burger, M. Walter, C. Persson, I. Brevik, D. F. Parsons, M. Boström and S. Y. Buhmann, *J. Phys. Chem. A*, 2017, **121**, 9742–9751.

284 D. F. Parsons, C. Carucci and A. Salis, *Phys. Chem. Chem. Phys.*, 2022, **24**, 6544–6551.

285 M. Boström, D. F. Parsons, A. Salis, B. W. Ninham and M. Monduzzi, *Langmuir*, 2011, **27**, 9504–9511.

286 A. Salis, D. F. Parsons, M. Boström, L. Medda, B. Barse, B. W. Ninham and M. Monduzzi, *Langmuir*, 2010, **26**, 2484–2490.

287 D. F. Parsons and B. W. Ninham, *Langmuir*, 2010, **26**, 6430–6436.

288 T. T. Duignan, D. F. Parsons and B. W. Ninham, *J. Phys. Chem. B*, 2013, **117**, 9412–9420.

289 T. T. Duignan, D. F. Parsons and B. W. Ninham, *J. Phys. Chem. B*, 2014, **118**, 3122–3132.

290 T. T. Duignan, D. F. Parsons and B. W. Ninham, *Phys. Chem. Chem. Phys.*, 2014, **16**, 22014–22027.

291 T. T. Duignan, D. F. Parsons and B. W. Ninham, *J. Phys. Chem. B*, 2014, **118**, 8700–8710.

292 T. T. Duignan, D. F. Parsons and B. W. Ninham, *Chem. Phys. Lett.*, 2015, **635**, 1–12.

293 A. Reyes, M. A. Tlenkopatchev, L. Fomina, P. Guadarrama and S. Fomine, *J. Phys. Chem. A*, 2003, **107**, 7027–7031.

294 P. Jurečka, J. Šponer and P. Hobza, *J. Phys. Chem. B*, 2004, **108**, 5466–5471.

295 P. Jurečka, J. Šponer, J. Černý and P. Hobza, *Phys. Chem. Chem. Phys.*, 2006, **8**, 1985–1993.

296 J. Řezáč, K. E. Riley and P. Hobza, *J. Chem. Theory Comput.*, 2011, **7**, 2427–2438.

297 S. Grimme, C. Diedrich and M. Korth, *Angewandte Chemie International Edition*, 2006, **45**, 625–629.

298 Y. S. Al-Hamdani, P. R. Nagy, A. Zen, D. Barton, M. Kállay, J. G. Brandenburg and A. Tkatchenko, *Nature Communications*, 2021, **12**, 3927.

299 F. Zahariev and M. S. Gordon, *Phys. Chem. Chem. Phys.*, 2021, **23**, 14308–14314.

300 K. Patkowski, *WIREs Computational Molecular Science*, 2020, **10**, e1452.

301 S. Chmiela, H. E. Sauceda, K.-R. Müller and A. Tkatchenko, *Nat. Commun.*, 2018, **9**, 3887.

302 R. O. Jones, *Rev. Mod. Phys.*, 2015, **87**, 897–923.

303 A. Pribram-Jones, D. A. Gross and K. Burke, *Annu. Rev. Phys. Chem.*, 2015, **66**, 283–304.

304 D. S. Sholl and J. A. Steckel, *Density Functional Theory*, John Wiley & Sons, Inc., Hoboken, NJ, USA, 2009.

305 P. Makkar and N. N. Ghosh, *RSC Adv.*, 2021, **11**, 27897–27924.

306 J. Hafner, C. Wolverton and G. Ceder, *MRS Bull.*, 2006, **31**, 659–668.

307 D. C. Langreth, B. I. Lundqvist, S. D. Chakarova-Käck, V. R. Cooper, M. Dion, P. Hyldgaard, A. Kelkkanen, J. Kleis, L. Kong, S. Li, P. G. Moses, E. Murray, A. Puzder, H. Rydberg, E. Schröder and T. Thonhauser, *J. Phys.: Condens. Matter*, 2009, **21**, 084203.

308 P. Hohenberg and W. Kohn, *Phys. Rev.*, 1964, **136**, B864–B871.

309 W. Kohn and L. J. Sham, *Phys. Rev.*, 1965, **140**, A1133–A1138.

310 A. Nangia, *J. Chem. Sci.*, 2010, **122**, 295–310.

311 J. S. Arey, P. C. Aeberhard, I.-C. Lin and U. Rothlisberger, *J. Phys. Chem. B*, 2009, **113**, 4726–4732.

312 J. Wang, G. Román-Pérez, J. M. Soler, E. Artacho and M.-V. Fernández-Serra, *J. Chem. Phys.*, 2011, **134**, 024516.

313 S. Grimme, *J. Comput. Chem.*, 2004, **25**, 1463–1473.

314 A. Tkatchenko and M. Scheffler, *Phys. Rev. Lett.*, 2009, **102**, 073005.

315 A. Tkatchenko, R. A. DiStasio, R. Car and M. Scheffler, *Phys. Rev. Lett.*, 2012, **108**, 236402.

316 J. F. Dobson, *Int. J. Quantum Chem.*, 2014, **114**, 1157–1161.

317 D. Langreth and J. Perdew, *Solid State Commun.*, 1975, **17**, 1425–1429.

318 G. Giuliani and G. Vignale, *Quantum Theory of the Electron Liquid*, Cambridge University Press, 2005.

319 J. Harl and G. Kresse, *Phys. Rev. B*, 2008, **77**, 045136.

320 J. Harl, L. Schimka and G. Kresse, *Phys. Rev. B*, 2010, **81**, 115126.

321 T. Björkman, A. Gulans, A. V. Krasheninnikov and R. M. Nieminen, *J. Phys.: Condens. Matter*, 2012, **24**, 424218.

322 M. Dion, H. Rydberg, E. Schröder, D. C. Langreth and B. I. Lundqvist, *Phys. Rev. Lett.*, 2004, **92**, 246401.

323 K. Lee, É. D. Murray, L. Kong, B. I. Lundqvist and D. C. Langreth, *Phys. Rev. B*, 2010, **82**, 081101.

324 D. Chakraborty, K. Berland and T. Thonhauser, *J. Chem. Theory Comput.*, 2020, **16**, 5893–5911.

325 P. Hyldgaard, K. Berland and E. Schröder, *Phys. Rev. B*, 2014, **90**, 075148.

326 K. Berland, V. R. Cooper, K. Lee, E. Schröder, T. Thonhauser, P. Hyldgaard and B. I. Lundqvist, *Rep. Prog. Phys.*, 2015, **78**, 066501.

327 K. Berland, C. A. Arter, V. R. Cooper, K. Lee, B. I. Lundqvist, E. Schröder, T. Thonhauser and P. Hyldgaard, *J. Chem. Phys.*, 2014, **140**, 18A539.

328 K. Berland, *PhD thesis*, Department of Microtechnology and Nanoscience – MC2, Chalmers University of Technology, Göteborg, Sweden, 2012.

329 G. Román-Pérez and J. M. Soler, *Phys. Rev. Lett.*, 2009, **103**, 096102.

330 E. Torres and G. A. DiLabio, *J. Phys. Chem. Lett.*, 2012, **3**, 1738–1744.

331 K. Berland, Y. Jiao, J.-H. Lee, T. Rangel, J. B. Neaton and P. Hyldgaard, *J. Chem. Phys.*, 2017, **146**, 234106.

332 V. Shukla, Y. Jiao, J.-H. Lee, E. Schröder, J. B. Neaton and P. Hyldgaard, *Phys. Rev. X*, 2022, **12**, 041003.

333 S. Seyedraoufi and K. Berland, *J. Chem. Phys.*, 2022, **156**, 244106.

334 S. Scheel and S. Y. Buhmann, *Acta Physica Slovaca*, 2008, **58**, 675–809.

335 L. D. Landau and E. M. Lifshitz, *The Classical Theory of Fields. Vol. 2*, Pergamon Press, Oxford, 4th edn, 1975.

336 L. Knöll, S. Scheel and D.-G. Welsch, Coherence and Statistics of Photons and Atoms, New York, 2001.

337 A. Messiah, *Quantum Mechanics*, Dover Publications, Mineola, New York, 2014.

338 S. Y. Buhmann, *Dispersion Forces II: Many-Body Effects, Excited Atoms, Finite Temperature and Quantum Friction*, Springer, Heidelberg, 2012.

339 H. T. Dung, S. Y. Buhmann, L. Knöll, D.-G. Welsch, S. Scheel and J. Kästel, *Phys. Rev. A*, 2003, **68**, 043816.

340 J. Klatt, M. B. Farías, D. A. R. Dalvit and S. Y. Buhmann, *Phys. Rev. A*, 2017, **95**, 052510.

341 S. Ribeiro, S. Y. Buhmann, T. Stielow and S. Scheel, *Europhys. Lett.*, 2015, **110**, 51003.

342 S. Y. Buhmann, *Dispersion Forces I: Macroscopic quantum electrodynamics and ground-state Casimir, Casimir–Polder and van der Waals forces*, Springer, Heidelberg, 2012.

343 E. A. Power and S. Zienau, *Philos. Trans. Royal Soc. A*, 1959, **251**, 427–454.

344 R. G. Woolley and C. A. Coulson, *Proc. R. Soc. A: Math. Phys. Eng. Sci.*, 1971, **321**, 557–572.

345 W. E. Lamb and R. C. Retherford, *Phys. Rev.*, 1947, **72**, 241–243.

346 B. W. Ninham and P. Lo Nostro, *Molecular Forces and Self Assembly in Colloid, Nano Sciences and Biology*, Cambridge University Press, Cambridge, 2010.

347 T. Gruner and D.-G. Welsch, *Phys. Rev. A*, 1996, **53**, 1818.

348 W. M. R. Simpson and U. Leonhardt, *Forces of the Quantum Vacuum*, WORLD SCIENTIFIC, 2015.

349 H. Bender, C. Stehle, C. Zimmermann, S. Slama, J. Fiedler, S. Scheel, S. Y. Buhmann and V. N. Marachevsky, *Phys. Rev. X*, 2014, **4**, 011029.

350 M. Arndt, O. Nairz, J. Vos-Andreae, . Keller, G. van der Zouw and A. Zeilinger, *Nature*, 1999, **401**, 680.

351 C. Brand, J. Fiedler, T. Juffmann, M. Sclafani, C. Knobloch, S. Scheel, Y. Lilach, O. Cheshnovsky and M. Arndt, *Ann. Phys.*, 2015, **527**, 580.

352 A. Salam, *Molecular Quantum Electrodynamics: Long-Range Intermolecular Interactions*, Wiley, 2009.

353 D. F. Parsons and B. W. Ninham, *J. Phys. Chem. A*, 2009, **113**, 1141–1150.

354 J. Fiedler and S. Scheel, *Ann. Phys.*, 2015, **527**, 570–579.

355 J. Fiedler, C. Persson, M. Boström and S. Y. Buhmann, *J. Phys. Chem. A*, 2018, **122**, 4663–4669.

356 S. Das, J. Fiedler, O. Stauffert, M. Walter, S. Y. Buhmann and M. Presselt, *Phys. Chem. Chem. Phys.*, 2020, **22**, 23295–23306.

357 S. Fuchs and S. Y. Buhmann, *Europhys. Lett.*, 2018, **124**, 34003.

358 E. M. Purcell, H. C. Torrey and R. V. Pound, *Phys. Rev.*, 1946, **69**, 37.

359 R. H. Dicke, *Phys. Rev.*, 1954, **93**, 99.

360 M. Gross and S. Haroche, *Phys. Rep.*, 1982, **93**, 301.

361 M. Gajdoš, K. Hummer, G. Kresse, J. Furthmüller and F. Bechstedt, *Phys. Rev. B*, 2006, **73**, 045112.

362 J. Gao, Q. Wu, C. Persson and Z. Wang, *Comp. Phys. Comm.*, 2021, **261**, 107760.

363 C. Persson and C. Ambrosch-Draxl, *Com. Phys. Comm.*, 2007, **177**, 280–287.

364 A. Crovetto, R. Chen, R. B. Ettlinger, A. C. Cazzaniga, J. Schou, C. Persson and O. Hansen, *Sol. Energy Mater. Sol. Cells*, 2016, **154**, 121–129.

365 J. F. Cooke and R. F. Wood, *Phys. Rev. B*, 1972, **5**, 1276–1283.

366 D. G. Shankland, *Int. J. Quantum Chem.*, 1971, **5**, 497–500.

367 E. L. Shirley, *Phys. Rev. B*, 1996, **54**, 16464–16469.

368 I. Souza, N. Marzari and D. Vanderbilt, *Phys. Rev. B*, 2001, **65**, 035109.

369 K. Berland and C. Persson, *J. Appl. Phys.*, 2018, **123**, 205703.

370 J. Tomasi, B. Mennucci and R. Cammi, *Chem. Rev.*, 2005, **105**, 2999–3094.

371 A. Klamt and G. Schüürmann, *J. Chem. Soc., Perkin trans. II*, 1993, 799–805.

372 A. Klamt, V. Jonas, T. Bürger and J. C. Lohrenz, *J. Phys. Chem. A*, 1998, **102**, 5074–5085.

373 R. Ghassemizadeh, B. Moore, T. Momose and M. Walter, *J. Phys. Chem. B*, 2019, **123**, 4392–4399.

374 J. Fiedler, M. Walter and S. Y. Buhmann, *J. Chem. Phys.*, 2021, **154**, 104102.

375 S. Pipolo, S. Corni and R. Cammi, *J. Chem. Phys.*, 2014, **140**, 164114.

376 L. Onsager, *J. Am. Chem. Soc.*, 1936, **58**, 1486–1493.

377 A. Held and M. Walter, *J. Chem. Phys.*, 2014, **141**, 174108.

378 J. Fiedler, F. Spallek, P. Thiyam, C. Persson, M. Boström, M. Walter and S. Y. Buhmann, *Phys. Rev. A*, 2019, **99**, 062512.

379 B. Hartl, S. Sharma, O. Brügner, S. F. L. Mertens, M. Walter and G. Kahl, *J. Chem. Theory Comput.*, 2020, **16**, 5227–5243.

380 S. Y. Buhmann and D.-G. Welsch, *Phys. Rev. A*, 2007, **77**, 012110.

381 E. T. Jaynes and F. W. Cummings, *Proc. IEEE*, 1963, **51**, 89.

382 B. W. Shore and P. L. Knight, *J. Mod. Opt.*, 1993, **40**, 1195–1238.

383 M. Tavis and F. W. Cummings, *Phys. Rev.*, 1968, **170**, 379–384.

384 H. Walther, B. T. H. Varcoe, B.-G. Englert and T. Becker, *Rep. Prog. Phys.*, 2006, **69**, 1325.

385 E. Hagley, X. Maître, G. Nogues, C. Wunderlich, M. Brune, J. M. Raimond and S. Haroche, *Phys. Rev. Lett.*, 1997, **79**, 1–4.

386 M. Brune, E. Hagley, J. Dreyer, X. Maître, A. Maali, C. Wunderlich, J. M. Raimond and S. Haroche, *Phys. Rev. Lett.*, 1996, **77**, 4887–4890.

387 T. Wilk, S. C. Webster, A. Kuhn and G. Rempe, *Science*, 2007, **317**, 488–490.

388 C. Hamsen, K. N. Tolazzi, T. Wilk and G. Rempe, *Phys. Rev. Lett.*, 2017, **118**, 133604.

389 K. Cui, K. S. Mali, D. Wu, X. Feng, K. Müllen, M. Walter, S. De Feyter and S. F. L. Mertens, *Small*, 2017, **13**, 1702379.

390 P. Bairi, K. Minami, J. P. Hill, W. Nakanishi, L. K. Shrestha, C. Liu, K. Harano, E. Nakamura and K. Ariga, *ACS Nano*, 2016, **10**, 8796–8802.

391 S. Das, J. Preiß, J. Plentz, U. Brückner, M. von der Lühe, O. Eckardt, A. Dathe, F. H. Schacher, E. Täuscher, U. Ritter, A. Csáki, G. Andrä, B. Dietzek and M. Presselt, *Adv. Energy Mater.*, 2018, **8**, 1801737.

392 K. Cui, K. S. Mali, O. Ivasenko, D. Wu, X. Feng, M. Walter, K. Müllen, S. De Feyter and S. F. L. Mertens, *Angew. Chem.*

Physical Chemistry Chemical Physics Accepted Manuscript

Physical Chemistry Chemical Physics Accepted Manuscript

Int. Ed., 2014, **53**, 12951–12954.

393 M. C. Stumpe and H. Grubmüller, *J. Phys. Chem. B*, 2007, **111**, 6220–6228.

394 C. Peter and K. Kremer, *Soft Matter*, 2009, **5**, 4357–4366.

395 O. Bezkorovaynaya, A. Lukyanov, K. Kremer and C. Peter, *J. Comput. Chem.*, 2012, **33**, 937–949.

396 M. R. Machado and S. Pantano, *Bioinform.*, 2016, **32**, 1568–1570.

397 L. A. Montero, J. Molina and J. Fabian, *Int. J. Quantum Chem.*, 2000, **79**, 8–16.

398 M. P. Metz, K. Piszczatowski and K. Szalewicz, *J. Chem. Theory Comput.*, 2016, **12**, 5895–5919.

399 T. Sachse, T. J. Martinez, B. Dietzek and M. Presselt, *J. Comput. Chem.*, 2018, **39**, 763–772.

400 *J-Aggregates*, ed. T. Kobayashi, World Scientific, 1996.

401 B. Kopainsky, J. K. Hallermeier and W. Kaiser, *Chem. Phys. Lett.*, 1981, **83**, 498–502.

402 A. Eisfeld, R. Kniprath and J. Briggs, *J. Chem. Phys.*, 2007, **126**, 104904.

403 C. Didraga, A. Pugžlys, P. R. Hania, H. von Berlepsch, K. Duppen and J. Knoester, *J. Phys. Chem. B*, 2004, **108**, 14976–14985.

404 F. Milota, V. I. Prokhorenko, T. Mancal, H. von Berlepsch, O. Bixner, H. F. Kauffmann and J. Hauer, *J. Phys. Chem. A*, 2013, **117**, 6007–6014.

405 F. Taher-Ghahramani, F. Zheng and A. Eisfeld, *Spectrochim. Acta A Mol. Biomol. Spectrosc.*, 2022, **275**, 121091.

406 H. von Berlepsch and C. Böttcher, *J. Phys. Chem. B*, 2002, **106**, 3146–3150.

407 H. von Berlepsch, K. Ludwig and C. Böttcher, *Phys. Chem. Chem. Phys.*, 2014, **16**, 10659–10668.

408 F. Haverkort, A. Stradomska, A. H. de Vries and J. Knoester, *J. Phys. Chem. B*, 2013, **117**, 5857–5867.

409 J. Megow, T. Körzdörfer, T. Renger, M. Sparenberg, S. Blumstengel, F. Henneberger and V. May, *J. Phys. Chem. C*, 2015, 5747–5751.

410 C. Friedl, T. Renger, H. v. Berlepsch, K. Ludwig, M. Schmidt am Busch and J. Megow, *J. Phys. Chem. C*, 2016, **120**, 19416–19433.

411 G. Zajac, E. Machalska, A. Kaczor, J. Kessler, P. Bouř and M. Baranska, *Phys. Chem. Chem. Phys.*, 2018, **20**, 18038–18046.

412 P. W. J. M. Frederix, I. Patmanidis and S. J. Marrink, *Chem. Soc. Rev.*, 2018, **47**, 3470–3489.

413 A. S. Bondarenko, I. Patmanidis, R. Alessandri, P. C. T. Souza, T. L. C. Jansen, A. H. d. Vries, S. J. Marrink and J. Knoester, *Chem. Sci.*, 2020, **11**, 11514–11524.

414 C. Boisseau, I. Simbotin and R. Côté, *Phys. Rev. Lett.*, 2002, **88**, 133004.

415 K. R. Overstreet, A. Schwettmann, J. Tallant, D. Booth and J. P. Shaffer, *Nat. Phys.*, 2009, **5**, 581–585.

416 D. Jaksch, J. I. Cirac, P. Zoller, S. L. Rolston, R. Côté and M. D. Lukin, *Phys. Rev. Lett.*, 2000, **85**, 2208–2211.

417 M. Saffman, T. G. Walker and K. Mølmer, *Rev. Mod. Phys.*, 2010, **82**, 2313–2363.

418 M. Saffman, *J. Phys. B: At. Mol. Opt. Phys.*, 2016, **49**, 202001.

419 I. S. Madjarov, J. P. Covey, A. L. Shaw, J. Choi, A. Kale, A. Cooper, H. Pichler, V. Schkolnik, J. R. Williams and M. Endres, *Nat. Phys.*, 2020, **16**, 857–861.

420 A. Browaeys and T. Lahaye, *Nat. Phys.*, 2020, **16**, 132–142.

421 M. Schlosser, D. O. de Mello, D. Schäffner, T. Preuschoff, L. Kohfahl and G. Birkl, *J. Phys. B: At. Mol. Opt. Phys.*, 2020, **53**, 144001.

422 T. Gallagher, *Rydberg Atoms*, Cambridge University Press, Cambridge, 2005.

423 R. J. LeRoy, *Can. J. Phys.*, 1974, **52**, 246–256.

424 J. Deiglmayr, *Physica Scripta*, 2016, **91**, 104007.

425 T. G. Walker and M. Saffman, *Phys. Rev. A*, 2008, **77**, 032723.

426 K. Singer, J. Stanojevic, M. Weidemüller and R. Côté, *J. Phys. B: At. Mol. Opt. Phys.*, 2005, **38**, 295–307.

427 A. A. Kamenski, N. L. Manakov, S. N. Mokhnenko and V. D. Ovsiannikov, *Phys. Rev. A*, 2017, **96**, 032716.

428 S. Weber, C. Tresp, H. Menke, A. Urvoy, O. Firstenberg, H. P. Büchler and S. Hofferberth, *J. Phys. B: At. Mol. Opt. Phys.*, 2017, **50**, 133001.

429 N. Šibalić, J. D. Pritchard, C. S. Adams and K. J. Weatherill, *Comput. Phys. Commun.*, 2017, **220**, 319–331.

430 J. Block and S. Scheel, *Phys. Rev. A*, 2017, **96**, 062509.

431 A. Anderson, S. Haroche, E. A. Hinds, W. Jhe and D. Meschede, *Phys. Rev. A*, 1988, **37**, 3594–3597.

432 V. Sandoghdar, C. I. Sukenik, E. A. Hinds and S. Haroche, *Phys. Rev. Lett.*, 1992, **68**, 3432–3435.

433 L. Béguin, A. Vernier, R. Chicireanu, T. Lahaye and A. Browaeys, *Phys. Rev. Lett.*, 2013, **110**, 263201.

434 S. Hollerith, J. Zeiher, J. Rui, A. Rubio-Abadal, V. Walther, T. Pohl, D. M. Stamper-Kurn, I. Bloch and C. Gross, *Science*, 2019, **364**, 664–667.